

Diese Dissertation haben begutachtet:

.....



DISSERTATION

# Novel Static and Dynamic Phenomena in Magnetoelectric Materials

ausgeführt zum Zwecke der Erlangung des akademischen Grades eines  
Doktors der technischen Wissenschaften unter der Leitung von

Univ.Prof. Dr.rer.nat. Andrei Pimenov

E138

Institut für Festkörperphysik

eingereicht an der Technischen Universität Wien  
Fakultät für Physik

von

Lukas Weymann

Matrikelnummer: 01635821

Kölblgasse 32/38, 1030 Wien

Wien, am September 24, 2020

# Kurzfassung

In dieser Dissertation werden verschiedene neuartige Phänomene in magnetischen und magnetoelektrischen Materialien mit einer breiten Auswahl an statischen und dynamischen Messmethoden untersucht.

Der magnetoelektrische Effekt wird direkt an Samarium Ferroborat,  $\text{SmFe}_3(\text{BO}_3)_4$ , gemessen. Dort beobachten wir entlang der dreifachen Symmetrie-Achse die Sättigung der magnetisch induzierten elektrischen Polarisierung bei kleinen Feldern und eine anschließende Unterdrückung der Polarisierung in starken gepulsten Magnetfeldern. Entlang einer anderen kristallographischen Richtung erhalten wir eine nicht-lineare induzierte Polarisierung, entsprechend der dreifachen Symmetrie des Kristalls.

In Holmium-dotierten Langasit,  $\text{Ho}_x\text{La}_{3-x}\text{Ga}_5\text{SiO}_{14}$ , wird ein ungewöhnlicher magnetoelektrischer Effekt gefunden, welcher mit zwei verschiedenen Ansätzen modelliert wird. Hierbei wird sowohl die besondere Winkelabhängigkeit des magnetoelektrischen Effekts berücksichtigt, als auch die magnetischen Eigenschaften. In diesem Material zeigt sich in der ungeordneten paramagnetischen Phase eine rätselhafte Kombination aus linearen und höchstgradig nicht-linearen magnetoelektrischen Signalen. So wächst die elektrische Polarisierung linear mit dem Magnetfeld, aber oszilliert viele Male unter der Rotation des Magnetfeldvektors. Diese Analyse liefert neue Einblicke in die Magnetoelektrizität von nicht-zentrosymmetrischen und paramagnetischen Verbindungen. Zusätzliche Erkenntnisse werden über die magnetischen Eigenschaften der Seltene-Erden-Langasite durch die Messung der paramagnetischen Resonanz in einem Mach-Zehnder-Interferometer im Sub-THz Bereich gewonnen. Bei dieser Untersuchung von  $\text{Ho}_x\text{La}_{3-x}\text{Ga}_5\text{SiO}_{14}$  wird auch von der Entdeckung eines starken Phonons bei ähnlichen Energien berichtet, welches eine ungewöhnliche Kopplung an ein angelegtes Magnetfeld zeigt, das zu einer Verschmälerung der Phononenresonanz führt.

In dünnen Filmen aus ferrimagnetischem Yttrium-Eisen-Granat wird bei der sub-THz-Spektroskopie bei der magnetischen Resonanz ein zusätzlicher Dämpfungsterm beobachtet. Dieses Phänomen kann von der intrinsischen Dämpfung durch eine Analyse der komplexen Transmission bei verschiedenen Resonanzfeldern und durch die Messung unterschiedlich dicker Proben mit unterschiedlichen experimentellen Geometrien separiert werden. Der vorgeschlagene mikroskopische Mechanismus basiert auf der kohärenten Reemission der einfallenden elektromagnetischen Welle durch einzelne magnetische Momente. Dadurch kann die beobachtete Dämpfung mit dem magnetischen Äquivalent der Superradianz in Verbindung gesetzt werden.

In den magnetoelektrischen Multiferroika  $\text{GaV}_4\text{S}_8$  und  $\text{Mn}_2\text{Mo}_3\text{O}_8$  wird Drehmomentmagnetometrie verwendet, um die Übergänge zwischen verschiedenen Quantenphasen

---

zu identifizieren. Es zeigt sich, dass die Winkelabhängigkeit des magnetischen Drehmoments ein nützliches Werkzeug ist, um konventionelle Messungen der Magnetisierung zu ergänzen. Außerdem kann sie auch bei der Bestimmung der Spinstruktur in diesen Materialien helfen.

# Abstract

In this dissertation, various novel phenomena in magnetic and magnetoelectric materials are investigated by a variety of static and dynamic methods.

A direct measurement of the magnetoelectric effect (MEE) is performed for samarium ferroborate,  $\text{SmFe}_3(\text{BO}_3)_4$ . There we observe along the threefold symmetry axis the saturation of magnetically induced electric polarization in small fields and subsequent suppression of the polarization in strong pulsed fields. Along a different crystallographic direction, we obtain a nonlinear induced polarization that is consistent with the threefold symmetry of the crystal.

In holmium-doped langasite,  $\text{Ho}_x\text{La}_{3-x}\text{Ga}_5\text{SiO}_{14}$ , an unusual effect is found and modeled with two different approaches. This includes the special angular dependence of the magnetoelectric effect as well as the magnetic properties. In this material a puzzling combination of linear and highly non-linear magnetoelectric responses in the disordered paramagnetic state coincide. In particular, the electric polarization grows linearly with the magnetic field, but oscillates many times upon rotation of the magnetic field vector. This analysis provides new insights into the magnetoelectricity of non-centrosymmetric and paramagnetic compounds.

An additional understanding of the magnetic properties of the rare-earth langasite compounds is obtained by measuring the paramagnetic resonance in a sub-THz Mach-Zehnder interferometer. This investigation of  $\text{Ho}_x\text{La}_{3-x}\text{Ga}_5\text{SiO}_{14}$  also reveals a strong phonon at similar energies, exhibiting an unusual coupling to an applied magnetic field that unexpectedly induces a narrowing of the phonon resonance.

In thin films of ferrimagnetic yttrium iron garnet, an additional radiative damping term is observed by sub-THz-spectroscopy at the magnetic resonance. This phenomenon can be separated from the intrinsic damping by an analysis of the complex transmission at different resonance fields and by measuring samples of different thicknesses with different experimental geometries. The proposed microscopic mechanism is based on the coherent re-emission of the incident electromagnetic wave by individual magnetic moments, allowing a relation between the observed damping and the magnetic equivalent of superradiance.

In the magnetoelectric multiferroics  $\text{GaV}_4\text{S}_8$  and  $\text{Mn}_2\text{Mo}_3\text{O}_8$  torque magnetometry is used to identify and resolve the transitions between different quantum phases. It is found that the angular dependence of the magnetic torque is a useful tool to complement conventional measurements of the magnetization, and can also help in determining the spin structure in these compounds.



# Contents

<b>1</b>	<b>Introduction</b>	<b>1</b>
<b>2</b>	<b>Experimental techniques</b>	<b>3</b>
2.1	Sample Characterization . . . . .	3
2.2	Static Properties Measurement Techniques . . . . .	3
2.2.1	Impedance Analyzer . . . . .	5
2.2.2	Electrometer . . . . .	5
2.2.3	Vibrating Sample Magnetometer . . . . .	7
2.2.4	Torque Magnetometer . . . . .	7
2.3	Dynamic Properties Measurement Techniques . . . . .	8
2.3.1	Backward Wave Oscillator . . . . .	8
2.3.2	Bolometer . . . . .	10
2.3.3	Cryostat . . . . .	10
2.3.4	Optical Elements . . . . .	10
2.4	Summary . . . . .	13
<b>3</b>	<b>Magnetoelectric Effect</b>	<b>15</b>
3.1	Introduction . . . . .	15
3.1.1	Linear Magnetoelectric Effect . . . . .	16
3.1.2	Higher Order Magnetoelectric Effects . . . . .	18
3.1.3	Microscopic Mechanism . . . . .	20
3.1.4	Magnetoelectric Multiferroics . . . . .	22
3.1.5	Applications . . . . .	23
3.2	Theory of the Magnetoelectric Effect in Rare-Earth Ferroborates . . . . .	24
3.3	Summary . . . . .	26
<b>4</b>	<b>Magnetoelectric Effect in Samarium Ferroborate</b>	<b>29</b>
4.1	High-Field Magnetoelectric Effect . . . . .	29
4.2	Induced Polarization along the $c$ -axis . . . . .	34
4.3	Summary . . . . .	34
<b>5</b>	<b>Magnetic Properties and the Magnetoelectric Effect in Ho-Langasite</b>	<b>37</b>
5.1	Simple Phenomenological Model of the Magnetoelectric Effect . . . . .	37
5.1.1	Holmium Langasite . . . . .	37
5.1.2	Magnetization . . . . .	39

5.1.3	Magnetoelectric Effect . . . . .	41
5.2	Extended Model of Magnetic Structure in Ho-LGS . . . . .	46
5.2.1	Breaking of Local $C_2$ Symmetry . . . . .	46
5.2.2	Magnetization . . . . .	48
5.2.3	Magnetic Torque . . . . .	50
5.2.4	Fitting the Magnetic Structure . . . . .	50
5.2.5	Paramagnetic Resonance . . . . .	56
5.2.6	Induced Electric Polarization . . . . .	59
5.2.7	Open Questions . . . . .	62
5.3	Electron-Phonon Coupling in Rare-Earth Langanites . . . . .	65
5.4	Excitation in the Complex Transmission . . . . .	67
5.5	Summary . . . . .	71
<b>6</b>	<b>Identifying Quantum Phase Transitions by Torque Magnetometry</b>	<b>73</b>
6.1	Transition of Cycloidal Phase to Skyrmion Lattice in $\text{GaV}_4\text{S}_8$ . . . . .	73
6.1.1	Identifying Phase Transitions by Magnetic Anisotropy . . . . .	74
6.2	Magnetic anisotropy in the antiferromagnetic multiferroic $\text{Mn}_2\text{Mo}_3\text{O}_8$ . . . . .	76
6.2.1	Manganese Molybdenum Oxide . . . . .	77
6.2.2	Magnetization . . . . .	78
6.2.3	Magnetic Torque . . . . .	78
6.3	Summary . . . . .	79
<b>7</b>	<b>Radiative Damping in Yttrium-Iron-Garnet Films</b>	<b>83</b>
7.1	Introduction . . . . .	83
7.2	Experimental Method . . . . .	84
7.3	Analyzing the Transmission Spectra and Separating Intrinsic and Radiative Damping . . . . .	86
7.4	Summary . . . . .	94
<b>8</b>	<b>Conclusions</b>	<b>95</b>
	<b>Acknowledgments</b>	<b>97</b>
	<b>Bibliography</b>	<b>101</b>

# 1 Introduction

Nearly every field of technology relies in one way or another on the development of new materials to either steadily improve functionality or to open completely new domains with the discovery of novel physical effects. This is especially true for the field of microelectronics, which is a primary driver of the huge changes seen in the everyday lives of most people during the last century, for example, due to the emergence of the first computers and smartphones.

A frequently mentioned candidate for the next leap in microelectronics are magnetoelectric materials, which are based on the coupling of electric and magnetic material properties. This coupling is not to be confused with the dualism of both fields in electromagnetic waves, as described by James Clerk Maxwell [1]. Even though the first induction of a magnetization in a dielectric material by moving it through a constant electric field was discovered already by Wilhelm Röntgen [2] in 1888, an internal coupling of electric and magnetic properties, as described by Pierre Curie [3] and further elaborated by Landau and Lifshitz [4], was not experimentally confirmed before the discovery of a linear magnetoelectric effect in the 1960's by Astrov [5]. Subsequently, research on magnetoelectricity was focused on the search for new magnetoelectric materials proving to be useful for applications by exhibiting stronger coupling and better operating temperatures. However, recent scientific attention has been drawn to many novel phenomena found to emerge in magnetoelectrics and in multiferroics. In this work, a wide range of experimental methods was used to investigate novel magnetoelectric effects in a diverse selection of magnetoelectric materials. These effects included both static and dynamic phenomena as well as non-negligible higher order terms.

In Chapter 2 different experimental setups are described. Primary measurements were performed using different operating modes of a commercially available Physical Properties Measurement System, equipped with a 14 T magnet, as well as a quasi-optical Mach-Zehnder interferometer, equipped with a 7 T magnet.

As previously stated, the magnetoelectric effect is the connecting concept between the samples investigated in this work. Therefore an extensive discussion about this effect is presented in Chapter 3, where the historical background will be briefly summarized, some potential applications introduced, and different realizations of the magnetoelectric effect elaborated. This includes the linear and higher order effects, magnetoelectric multiferroics and a model of the magnetoelectric effect in rare-earth ferrobates [6].

Chapters 4, 5, 6, 7 represent the primary body of work, showcasing all measurements of the different material classes studied. Chapter 4 focuses on  $\text{SmFe}_3(\text{BO}_3)_4$ , a member of the well investigated rare-earth ferrobates, known for exhibiting a giant magnetoelec-

tric effect [7]. However, the model developed in [6], based on the magnetism of the Fe and the Sm-ions, does not give a perfect agreement for the electric polarization induced by a high magnetic field. This indicates an inaccurate assumption of the Fe-Sm molecular field based on the estimated Landé-factor of Sm. By performing measurements in a pulsed high magnetic field, we overcome the difficulties in determining the Landé factor and refine this model. Moreover, the previous theory does not account for a magnetically induced polarization along the crystal's threefold axis, as it is limited to the first order approximation. We present the first experimental observation of such a higher order magnetoelectric effect in  $\text{SmFe}_3(\text{BO}_3)_4$  and propose a simple phenomenological model based solely on symmetry considerations.

In Chapter 5, a more extensive model is developed to explain the unusual magneto-electric effect observed in  $\text{Ho}_x\text{La}_{3-x}\text{Ga}_5\text{SiO}_{14}$ . In this non-centrosymmetric material, a linear magnetoelectric effect is forbidden by the crystal symmetry, but emerges at small magnetic fields on top of a higher order effect. The effect is observed when measuring the electric polarization along the high symmetry axis and when rotating the magnetic field around this axis. A model to explain this phenomenon is developed in two steps. First a phenomenological model is proposed by only taking into account the magnetically induced magnetization and polarization curves. This model is then revisited and expanded by taking into account the magnetic anisotropy and the paramagnetic resonance, as obtained by sub-THz-spectroscopy. In the same chapter a puzzling coupling between a low-frequency phonon and applied magnetic fields is explored and discussed.

In Chapter 6, the quantum phase diagram of two transition metal multiferroics is investigated by torque magnetometry. It is shown that this simple experimental method represents a valuable technique to complement magnetization curves when identifying magnetic phase transitions. In  $\text{GaV}_4\text{S}_8$ , the torque measurements prove to be useful for accurately measuring the phase transition of a cycloidal spin structure into a skyrmion lattice. In the polar magnet  $\text{Mn}_2\text{Mo}_3\text{O}_8$ , we resolve the transitions between the different phases of antiferromagnetically coupled magnetic moments.

In Chapter 7, a novel magnetic superradiance effect is revealed in thin films of yttrium iron garnet using the technique of transmission spectroscopy in a quasi-optical Mach-Zehnder interferometer under applied magnetic fields. The versatility and sensitivity of this experimental setup can be used to distinguish between subtle differences in the ferrimagnetic resonances originating from changes of the experimental geometry, sample thickness and resonance frequency. Using this sensitive data, we can separate the internal contribution to the line width of the resonance from the contribution of the radiative damping, which is identified as a 'superradiating' effect.

The conclusions of this work are provided in Chapter 8.

## 2 Experimental techniques

For the investigations reported in this thesis, a wide range of experimental techniques was used, falling into three categories: measurements of static phenomena, dynamic phenomena and sample characterization. A short introduction of the used experimental setups is given in this Chapter.

### 2.1 Sample Characterization

The samples have been characterized by several experiments that will be briefly introduced. A Laue diffractometer was used to confirm and accurately determine the orientation of the langasite compounds and the  $\text{SmFe}_3(\text{BO}_3)_4$  samples. The accurate orientation is of particular importance for the measurements of the angular dependence of the magnetic properties and the magnetoelectric effect. The diffractometer is based on the diffraction of a non-monochromatic X-ray beam on the crystal lattice.

The purity of the langasite crystals was probed with a scanning electron microscope operating with back scattered electrons. The accurate value of the holmium content in the  $\text{Ho}_x\text{La}_{3-x}\text{Ga}_5\text{SiO}_{14}$  samples (Chapter 5) is essential to analyze the corresponding measurements and was obtained by comparing a Ho-langasite sample with a pure langasite crystal ( $x = 0$ ) in a total reflection x-ray fluorescence (TXRF) analyzer<sup>1</sup>.

### 2.2 Static Properties Measurement Techniques

Static phenomena were mostly explored by different options for a commercially available Physical Properties Measurement Systems (PPMS) of the company Quantum Design. The PPMS is a variable temperature-field system providing a noteworthy versatility due to its modular structure. It can operate in a temperature range of 2 K-400 K and is equipped with a helium-cooled superconducting 14 T magnet. For the measurements in this work we used the commercial vibrating sample magnetometer and torque magnetometer options, complemented with an electrometer and an impedance analyzer.

---

<sup>1</sup>This sample characterization measurement was kindly performed by our colleagues Peter Kregsamer and Christina Strelj from the Institute of Atomic and Subatomic Physics of the Vienna University of Technology.

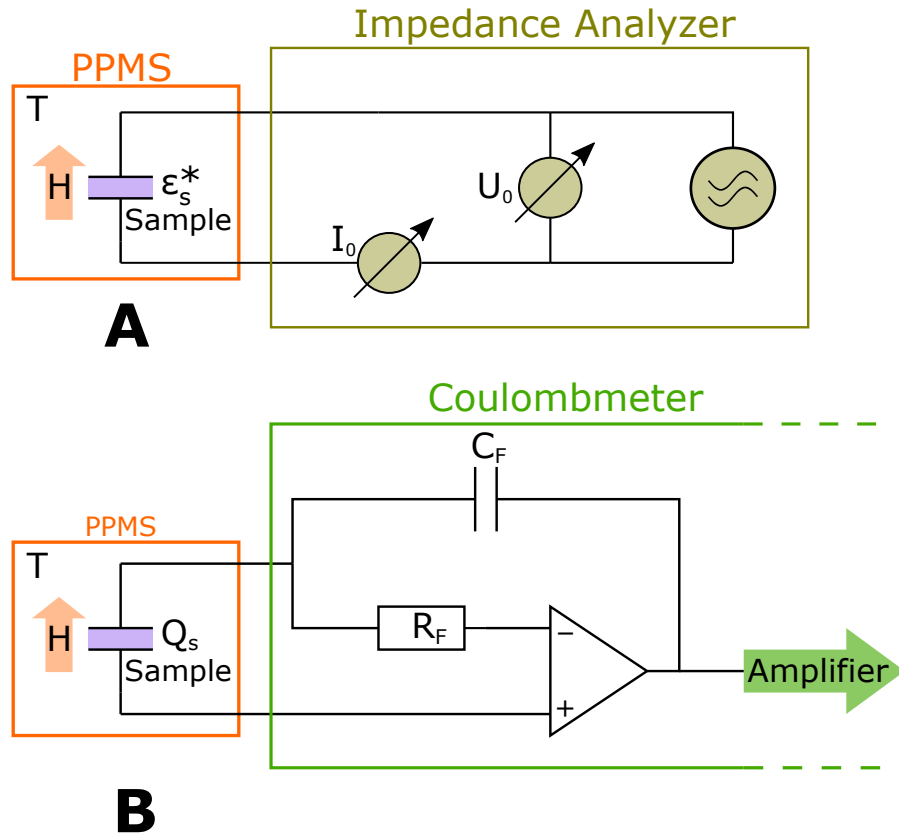


Figure 2.1: Schematic visualization of the circuitry of two experiments that were used to investigate the dielectric permittivity and the magnetoelectric effect. Both setups are based on the PPMS as the central element, in which the temperature  $T$  and the magnetic field  $H$  can be varied.

**A** Simplified circuitry of the Alpha-A High-Resolution Measurement System, which is used to determine the samples dielectric permittivity  $\epsilon_s^*$ . A sinusoidal voltage  $U_0$  is applied and simultaneously the response current  $I_0$  is measured.

**B** The essential part of the Keithley Electrometer, which is used to measure the charge  $Q_s$ , which is magnetically induced on the sample surfaces. The charge is transferred onto a known capacitor  $C_F$  and the balancing voltage amplified and read-out.

### 2.2.1 Impedance Analyzer

The dielectric permittivity of the sample can be measured by exchanging the multimeter with an impedance analyzer; in the presented measurements the Alpha-A High Resolution Measurement System of the company Novocontrol Technologies was used. Even though the frequency dependent dielectric permittivity is a dynamic sample property, we used the impedance analyzer for determining its static limit by measuring at low frequencies.

The impedance analyzer applies a sinusoidal voltage  $U(t) = \text{Re}(U_0 \exp(i\omega t))$  with a fixed frequency  $\omega$  and amplitude  $U_0$  to the sample capacitor, i.e. the two silver paste electrodes on opposite sample surfaces. Here  $t$  is the time, with  $t = 0$  chosen in such a way that the equation holds. This voltage induces a current to flow through the sample  $I(t) = \text{Re}(I^* \exp(i\omega t))$  with the same frequency, but an amplitude  $I_0 = |I^*|$  and phase shift  $\tan(\varphi) = \text{Im}(I^*)/\text{Re}(I^*)$  that depend on sample properties. The obtained impedance  $Z^* = \frac{U_0}{I^*}$  can be used to get the dielectric permittivity of the samples

$$\varepsilon^* = \frac{d}{\varepsilon_0 A} \frac{1}{i\omega Z^*}, \quad (2.1)$$

where  $d$  is the thickness of the sample and  $A$  the surface of the silver paste electrodes. The frequency range of the Alpha-A Analyzer spans from  $3 \mu\text{Hz}$  to  $20 \text{MHz}$  and measures the relative impedance with an accuracy of  $< 3 \times 10^{-5}$  and the absolute phase angle with  $< 0.002^\circ$ . A simplified sketch of the circuitry is shown in Fig. 2.1 **A**.

### 2.2.2 Electrometer

The measurements of the magnetoelectric effect are performed by using a commercially available multimeter of the company Keithley Instruments. It measures the charges that are induced in two silver paste electrodes, which are prepared on opposite sample surfaces and connected to the electrometer, which detects the charges that are induced by the applied magnetic field, as shown in Fig. 2.1**B**. A capacitor with an accurately known capacity  $C_F$  is placed in the feedback loop of an operational amplifier (OP). The induced charge on the sample  $Q_s$  is stored on this capacitor and matched via the OP with a balancing voltage  $V$ . This voltage is then amplified by a second OP and finally measured. Due to the known capacity  $C_F$ , the charge can be recalculated by the expression  $Q_s = C_F V$ . The electrometer is equipped with four capacitors to resolve charges down to  $10 \text{fC}$  and up to  $2.1 \mu\text{C}$ .

Due to the upper limit of the magnetic field provided by the PPMS, additional high-field measurements of the magnetoelectric effect were performed in a pulsed magnet at the Dresden High Magnetic Field Laboratory (HLD) at the Helmholtz Zentrum Dresden-Rossendorf.

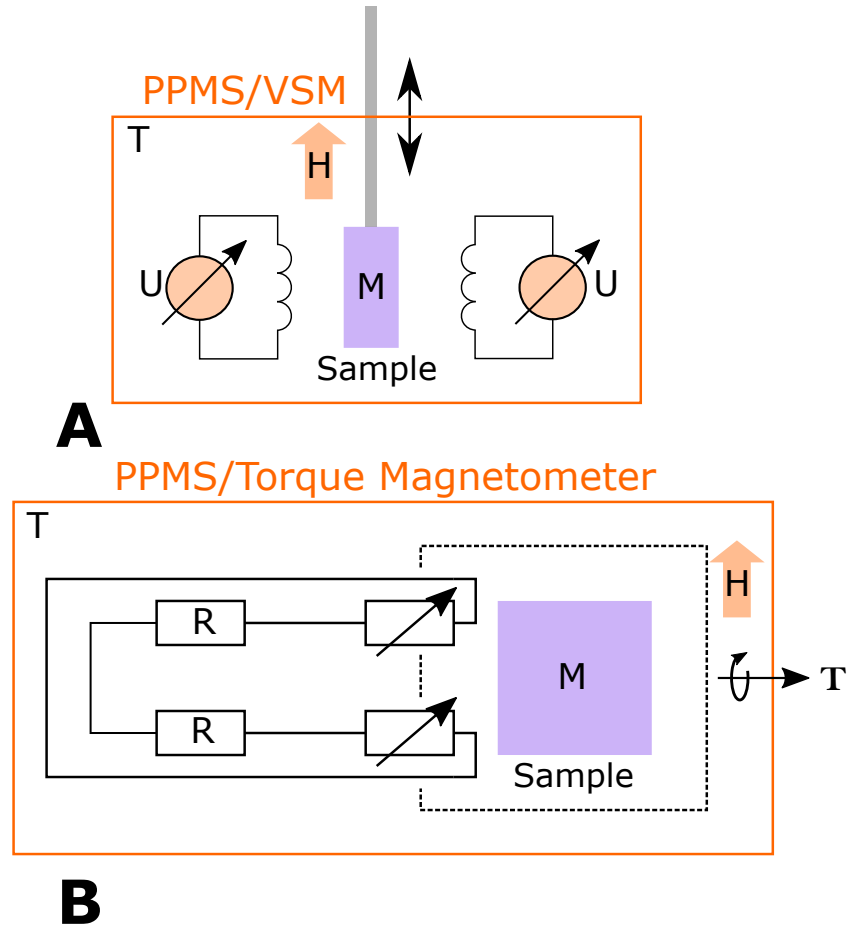


Figure 2.2: Schematic visualization of the circuitry of two experiments that were used to investigate the magnetic properties of the sample. Both setups are based on the PPMS as the central element, in which the temperature  $T$  and the magnetic field  $H$  can be varied. **A** Simplified structure of the Vibrating Sample Magnetometer. The oscillation of the sample magnetization  $M_s$  induces a voltage  $U$  in the pickup coils.

**B** The circuitry of the Wheatstone bridge, which is the central element of the Torque Magnetometer. A non-parallel applied magnetic field and sample magnetization lead to a torque  $\mathbf{T}$ , which induces a variation of electrical resistance in two piezoresistive paths, which is then matched by two known high-precision resistors. The balancing voltage is measured to determine the magnetic torque.

### 2.2.3 Vibrating Sample Magnetometer

The vibrating sample magnetometer (VSM) is a DC magnetometer that measures the samples magnetization by reading out the voltage

$$V_{\text{coil}} = \frac{d\Phi}{dt} \quad (2.2)$$

that it is induced in a pickup coil by the change of magnetic flux  $\Phi$  over time  $t$ , when the sample is oscillated in the vicinity of the coil. The characteristic vibration of the sample at a frequency of 40 Hz and an amplitude of 2 mm is generated by a linear motor. Using a lock-in detection technique of the amplified induced voltage, a resolution of  $10^{-6}$  emu is achieved. A sketch of the experimental setup is shown in Fig. 2.1C. Additional low field measurements were performed in a SQUID magnetometer<sup>2</sup> with a rotatable sample holder, which provides the angular dependence of the magnetization. This measurement of the magnetization in static 'low' fields is complemented by high-field measurements performed in a pulsed magnet with field strengths up to 56 T in the High Field Laboratory at the Helmholtz-Zentrum Dresden-Rossendorf in Germany. This magnetometer is based on a similar principle as the VSM: The induced magnetization leads to a voltage in pickup coils that can be read-out. But instead of oscillating the sample in a DC magnetic field in the vicinity of the coils, the change of magnetization is generated by the pulse nature of the field.

### 2.2.4 Torque Magnetometer

Measuring the torque that is induced by an applied magnetic field  $\mathbf{B}$  on a sample with magnetization  $\boldsymbol{\mu}$  is given by

$$\boldsymbol{\tau} = \boldsymbol{\mu} \times \mathbf{B}. \quad (2.3)$$

The torque magnetometer option for the PPMS is designed to measure this property accurately to give insights into the magnetization of the investigated material. The sample is mounted on a lever sample stage that is only connected to the sensor by two piezoresistive legs, wherein a torsion leads to a change in resistance. If a magnetization is induced that is neither parallel nor perpendicular to the applied field, Eq. (2.3) gives a non-zero torque  $\boldsymbol{\tau}$  that is read-out by the difference of resistance  $\Delta R = R_1 - R_2$  in the two piezoresistive paths, which is extracted by a Wheatstone bridge circuitry, as visualized in Fig. 2.1D. Two accurately known high-precision resistors are connected and a balancing voltage is used to determine  $\Delta R$ , which is induced in both legs by the proportional magnetic torque. The sensor chip is mounted on a horizontal rotator option, which provides a full rotation of the sample around an in-plane axis of the thin plate sample in the magnetic field. Therefore a full measurement of  $\boldsymbol{\tau}$  can be performed

<sup>2</sup>These measurements were performed by Vsevolod Ivanov at the Prokhorov General Physics Institute of the Russian Academy of Sciences.

with two complementary cuts of the investigated crystal. Nevertheless the sample size is limited due to the rather small size of the torque sensor chips ( $1.5 \times 1.5$  mm) and the maximum torque of  $10^{-5}$  Nm. Above this limit the torque magnetometer enters a non-linear regime and the chip can break. The gravitational background can be subtracted by a measurement of the paramagnetic samples in zero magnetic field. This setup provides the possibility to measure field scans of the magnetic torque for a fixed angle, or resolving the angular dependence of the torque at a fixed magnetic field.

### 2.3 Dynamic Properties Measurement Techniques

In addition to the investigation of static properties, a quasi-optical sub-THz Mach-Zehnder interferometer (Fig. 2.4) was used to explore dynamic phenomena. On the one hand this frequency range is perfect for electron spin- and ferromagnetic resonance spectroscopy, but on the other hand we also report the observation of an optical phonon, which is a rather unusual finding in this frequency range. The experimental setup is schematically shown in Fig. 2.4. The central element of the setup is the splitting of the electromagnetic wave into two separate beams, which interfere again before the signal is detected. The traveled distance of both light paths is equal, but while one beam travels only in free space, the second beam is transmitted through the sample. Since the samples refractive index deviates in general from the refractive index of air, the optical path length of both beams are usually not the same. However, the length of the sample beam path can be adjusted by an automatically movable mirror, which maintains a zero difference of both optical path lengths. The mirrors position can therefore be translated into the phase shift that occurs when the wave is transmitted through the sample. Hence, by simultaneously measuring the absorption coefficient, the complex refractive index  $n^*$  of the investigated material can be recalculated. The interferometer can also operate at a 'transmission-only' mode, where the reference beam is blocked and a mechanical chopper is installed in the main beam. This setting provides quicker and more accurate measurements of the transmission through the sample, while the phase information is lost. The absolute value of the transmission is determined in this case, by comparing the transmission through the sample with a reference measurement, in which the sample is removed from the beam.

The experimental setup allows for either frequency scans at a fixed applied magnetic field, or measuring at a fixed frequency while sweeping the magnetic field. In the following, we will have a closer look on the different elements of the Mach-Zehnder interferometer.

#### 2.3.1 Backward Wave Oscillator

To enable the investigation of a broad range of sub-THz phenomena the source of a Mach-Zehnder interferometer has to meet certain requirements, foremost the provision

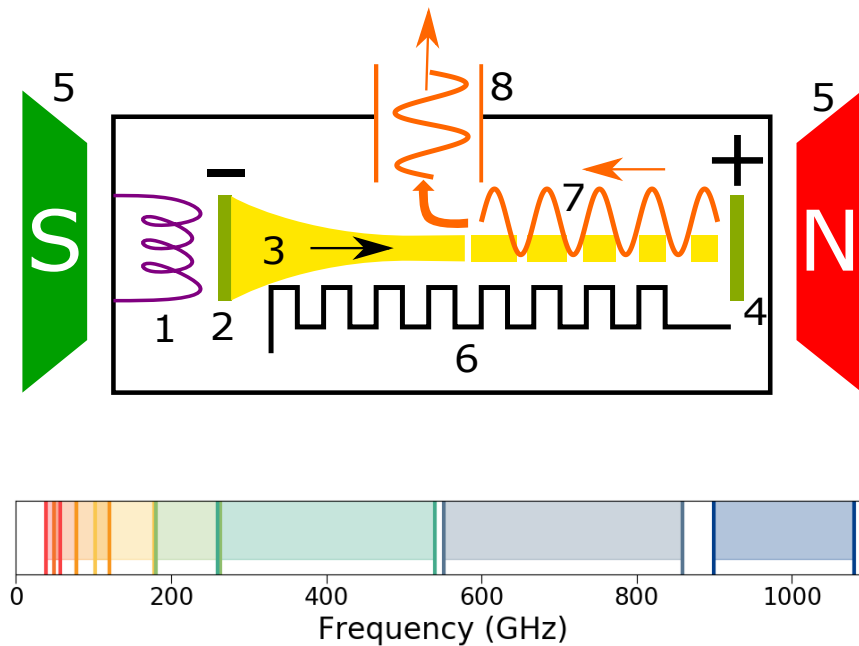


Figure 2.3: Schematic of a backward wave oscillator in accordance to [8] is shown on the **top**. The heater (1) induces the emission of electrons in the cathode (2), which are then accelerated onto the anode (4), forming an electron beam (3), which is collimated by a magnetic field (5). The periodic slow structure (6) induces a grouping of the electrons, which generates the electromagnetic wave (7) that is led out by a waveguide (8). The cooling system is not shown for the sake of simplicity. In the **bottom**, the frequency range of the eight backward wave oscillators of different construction. The overlap of a few lamps is useful to combine the spectra of different frequency ranges.

of monochromatic light in a broad frequency range with a reasonably high intensity. In the presented research a set of eight backward wave oscillators (BWO) was used to meet those requirements. BWOs are electrovacuum generators of continuous electromagnetic waves with tunable frequencies in the range of  $\pm 30\%$  around the central value and a characteristic output power of 10 mW, which can reach up to 200 mW for long wavelengths lamps [8], as shown in Fig. 2.3. The radiation is generated by a very delicate mechanism, including the need for high voltage, high vacuum and the resilience to high temperatures. A stream of electrons is created by a heated cathode and accelerated by the application of a high voltage of up to 6.5 kV onto an collector anode, while being collimated by an applied magnetic field. This electron beam travels over a comb-like electrode consisting of up to 200 closely placed plates, which functions as a slowing system. This leads to a periodical bunching of the electrons, which generates an electromagnetic wave that travels in the opposite direction of the electrons on a waveguide into free space; hence the name 'backward wave'. Since the frequency of the output radiation is determined by

the separation of the rods and the kinetic energy of the electrons, which is transferred by the slowing system onto the electromagnetic wave, the described frequency tuning can be achieved by a variation of the acceleration voltage. A frequency of approximately 0.03 - 1.1 THz is covered by a set of nine BWOs. Either air or water cooling is needed to establish a stable operation of the lamps. Even though BWOs are nearly perfect for these kind of scientific applications, the industrial production is nowadays strongly reduced.

### **2.3.2 Bolometer**

The sub-THz beam can be detected by any far-infrared detector. For this purpose a commercially available helium-cooled infrared bolometer was used, since it provides a significantly higher sensitivity than a comparable room-temperature device (e.g. Golay cell). The bolometers principle of operation is fairly simple. The incoming radiation is absorbed by a semiconductor, which leads to a rise of temperature that can be read out by the change of resistivity. To maintain a continuous operation mode, the heat has to be transferred quickly to the temperature reservoir. Therefore, a low specific heat of the semiconductor is desirable to allow for a high speed operation mode, as well as a large temperature coefficient to increase the bolometers sensitivity. In the case of a helium cooled bolometer, these quantities need to satisfy the requirements for temperatures around 4.2 K. A continuous comparison with the zero signal is needed to get good absolute values for the absorbed intensity and to increase the signal to noise ratio. This is either realized by operating at destructive interference (transmission and phase mode) or with a mechanical chopper (transmission only mode) and a lock-in amplifier. However, it should be mentioned that due to a possible change of transmission through the sample, the 'destructive interference' is just a minimum of the signal and only zero, if the amplitude of sample and reference beam are equal before interfering in the final polarizer.

### **2.3.3 Cryostat**

The sample is mounted in a magneto-optical cryostat with four Mylar windows, which provides magnetic fields of up to 7 T. The field is generated by a superconducting coil in a helium bath and can be applied in the horizontal plane either parallel (Faraday geometry) or perpendicular (Voigt geometry) to the beam path by rotating the cryostat. The sample can be cooled down to 1.8 K by pumping the sample chamber with liquid helium.

### **2.3.4 Optical Elements**

Due to the long wavelength of the sub-THz radiation, conventional glass lenses used for optical interferometers are not compatible with this setup. Therefore the lenses are made from polyethylene or teflon, materials that are transparent and have a low refractive

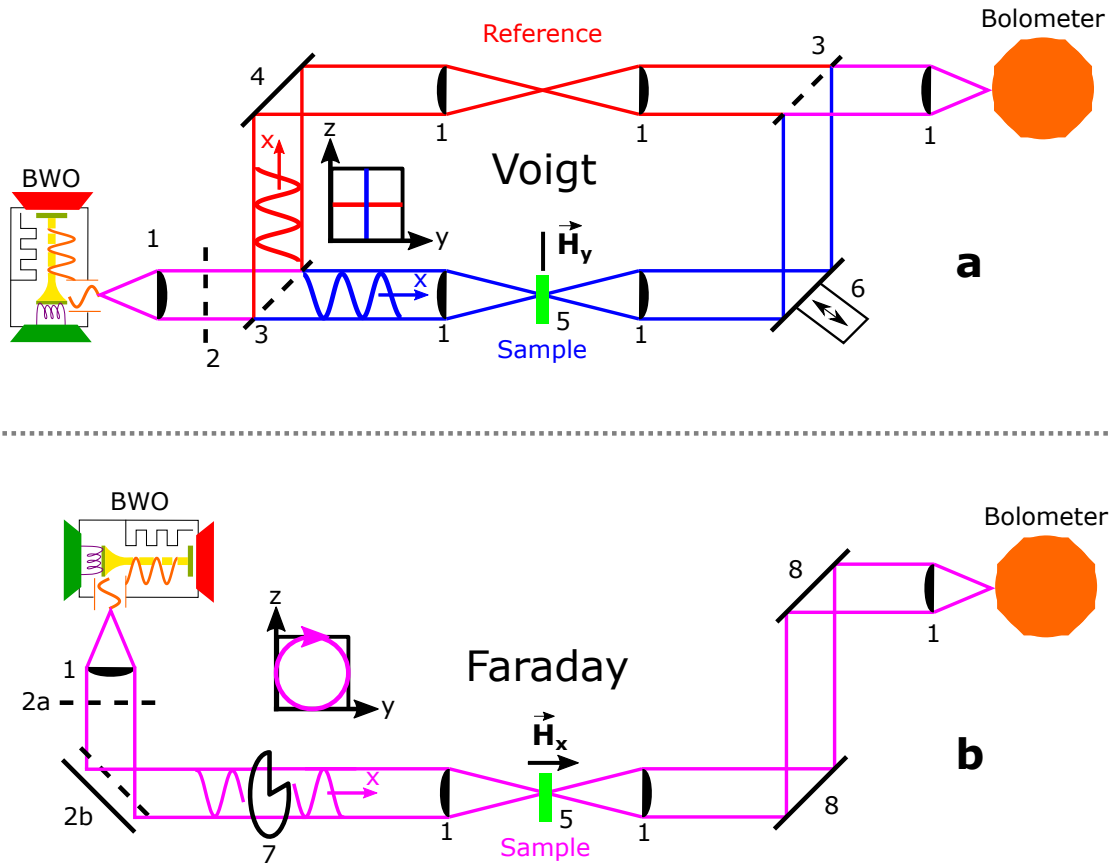


Figure 2.4: Schematic setup of the Mach-Zehnder interferometer. The operation principles of source (BWO) and detector (bolometer) are explained in the text.

**top** Voigt geometry: The spherical lenses (1) are used to either transform divergent light into parallel beams or focus the radiation onto the sample (5), which is mounted in a magneto-optical cryostat, or the detector. A metallic wire grid is used to linearly polarize (2) and split (3) the beam. A motorized mirror (6) is installed in the sample beam (blue), which adjusts its optical path length to interfere destructively with the reference beam (red), which runs over a modulating mirror (4).

**bottom** Faraday geometry: The linear polarizer (2a) is complemented with a circular polarizer (2b), as explained in the text. A chopper (7), coupled via a lock-in amplifier with the bolometer - is used to improve the absolute signal. No reference beam can be used in this setup, which therefore only allows for measuring in transmission mode. Due to this fact, the beam splitters and the motorized mirror can be removed and replaced by simple mirrors (8). Further optical elements like attenuators and additional polarizers were left out for the sake of simplicity. Both setups are explained in more detail in the text.

index in this frequency range. Here, we will shortly explain all optical elements of the interferometer ordered from source to detector (Fig. 2.4).

The first lens transfers the divergent radiation emitted by the BWO into a parallel beam. Since the intensity of the BWOs cannot be controlled directly, a set of four combinable attenuators is used, which transmit 30%, 10%, 3% or 1% of the signal, respectively. The next element on the beam path is only used for the 'transmission-only' mode: a mechanical chopper, operated at a frequency of 23 Hz and connected to the detection unit. It continuously provides a zero signal over the course of the complete measurement. Due to the fact that the light emitted by the lamp is monochromatic, but not always perfectly polarized, a wire grid polarizer, which consists of a parallel grid of thin tungsten wires, with an inter-wire distance of 0.03 mm, is installed to control the polarization based on the following principle. The unpolarized light can be described as the sum of two perpendicularly linear polarized waves. The wave that is polarized perpendicular to the wires is not affected by the grid (wave length  $\lambda \gg d_{\text{wire}}$  thickness of wire), but for the parallel wave the wires function as a metal surface: The electron gas is set into oscillation by the wave and emits a secondary wave; the beam is reflected. For achieving a circular polarization a combination of wiregrid and mirror is placed in a  $45^\circ$  angle to the light beam (shown in Fig. 2.4). The light polarized perpendicular to the wires passes the grid, is reflected by the mirror and passes the grid again, where it interferes with the parallel polarized light that is reflected by the grid. When the distance between grid and mirror is exactly a quarter of the wave length, hence giving this optical element the name  $\lambda/4$ -plate, the resulting wave will be circularly polarized. However, the circular polarized light can only be used in the 'transmission only' mode. Due to the described working principle of a linear polarizer, the same element is used as a beam splitter, splitting the light into reference and sample beam. The latter is focused by a lens onto the sample, which is mounted inside the magneto-optical cryostat and transferred back into a parallel beam by another lens. For a better comparability two equal lenses are installed in a similar manner in the reference beam. While the mirror in the sample beam is motorized to maintain the destructive interference as mentioned above, the mirror in the reference beam oscillates with a frequency of  $\Omega_{\text{mod}} \approx 28$  Hz and an adjustable amplitude. This modulation mirror is primarily used to provide the information about the transmission of the sample, as described below. A second beam splitter is installed to combine both beams again, which then interfere in another polarizer, before the combined light gets focused into the bolometer.

The phase shift can be read out directly by the movement of the motorized mirror, which maintains an equal optical path length. Therefore the reference and sample beam lengths have to be calibrated to find the movable mirrors 'zero position', by removing the sample out of the sample beam and finding the zeroth order of the destructive interference. The polarizer in front of the detector has to be set in such a way that the electric fields of reference  $E_{\text{ref}}(t)$  and sample beam  $E_{\text{sam}}(t)$  are subtracted from each

other. Therefore the intensity as measured in the bolometer is given by

$$\begin{aligned}
 I(t) &= |E_{\text{sam}}(t) - E_{\text{ref}}(t)|^2 \\
 &= |E_{\text{sam},0} e^{i(\omega t + \Delta\varphi)} - E_{\text{ref},0} e^{i(\omega t + A_{\text{PM}} \cos(\Omega_{\text{mod}} t))}|^2 \\
 &= E_{\text{sam},0}^2 + E_{\text{ref},0}^2 - 2E_{\text{ref}}E_{\text{sam}} \cos(\Delta\varphi - A_{\text{PM}} \cos(\Omega_{\text{mod}} t)),
 \end{aligned} \tag{2.4}$$

where the starting point of the time  $t = 0$  was chosen in such a way that the equations hold. Here  $\omega$  denotes the lights frequency and  $E_{\text{sam},0}$  and  $E_{\text{ref},0}$  are the amplitudes of sample and reference beam, respectively. While the phase shift between both beams  $\Delta\varphi$  is constant over time, the induced phase shift by the modulation mirror with an amplitude  $A_{\text{PM}}$  and a frequency  $\Omega_{\text{mod}}t$  is time dependent. The movable mirror adjusts the phase difference to  $\Delta\varphi = 2\pi m$  by moving to the closest minimum, where the integer  $m$  denotes the order of the minimum. The direction that it has to move to is obtained by analyzing the modulated signal. A measurement of the spectra can be used to confirm that in fact the zeroth order was achieved, via the position of the minimum

$$\Delta l = (n - 1)d - m\lambda, \tag{2.5}$$

where  $n$  ( $= 1$  for the calibration measurement) is the refractive index and  $d$  the thickness of the sample.  $\Delta l$  is only independent of the wavelength  $\lambda$  at  $m = 0$ , when the dispersion of  $n$  is small enough that  $\Delta n \cdot d \ll \lambda$  can be assumed.

While the transmission phase can be easily calculated by the position of the movable mirror, i.e. the minimum, the transmission is obtained by the curvature of the signal modulated around the minimum and extracted by the applied lock-in technique.

## 2.4 Summary

The experimental setups introduced above allow for an extensive investigation of magnetic and magnetoelectric compounds, as presented in Chapters 4-7. For this work, the direct observation of the magnetoelectric effect via the combination of an Electrometer and Physical Properties Measurement System is essential. The magnetic properties are investigated in the static regime by a Vibrating Sample Magnetometer and a Torque Magnetometer and complimented by dynamic measurements of the magnetic resonance in a Mach-Zehnder interferometer operating with monochromatic sub-THz radiation. The latter also allows for the investigation of other dynamic phenomena, like a low-frequency phonon (Chapter 5.3) and the magnetic equivalent of superradiance (Chapter 7).



# 3 Magnetolectric Effect

In this section the magnetolectric effect will be introduced, considering the historical background, prominent compounds and possible applications. Further details can be found in recent reviews about the linear [9] and higher order [10] magnetolectric effects (MEE) and magnetolectric multiferroics [11; 12]. Moreover, the quantum theory developed for describing the MEE in rare-earth ferrobates [6], which will be applied in Chapter 4 and expanded in Chapter 5 for the MEE in  $\text{Ho}_x\text{La}_{3-x}\text{Ga}_5\text{SiO}_{14}$ , is presented and discussed.

All materials that were investigated in this work are magnetolectric. While the rare-earth langasites are paramagnetic and dielectric (showing no ferroic order), yttrium iron garnet is ferrimagnetic and  $\text{SmFe}_3(\text{BO}_3)_4$  has even two coupled ferroic orders (antiferromagnetic and ferroelectric) and is, therefore, considered to be a magnetolectric multiferroic. While these materials are based on magnetic rare-earth ions, the samples investigated in Chapter 6 are transition metal magnetolectric multiferroics.

## 3.1 Introduction

The possibility of a correlation of magnetic and electric material properties were first discussed by Pierre Curie [3], as a consequence of his hypothesis: '[...] when certain causes produce certain effects, the elements of symmetry of the causes must be found in the effects produced'<sup>1</sup>, which became later known as Curie's principle. However, it took more than 65 years until the realization that a breaking of time-reversal symmetry is mandatory to get a magnetolectric response, as formulated by Lev Landau and Evgeny Lifshitz [4]. This led to the first observation of an intrinsic ME in the form of an induced magnetization by (and linearly on) the application of an electric field in  $\text{Cr}_2\text{O}_3$  [5]. It is quite remarkable that the reverse effect, an electric polarization induced by a magnetic field, was only measured a year later [13], since nowadays the latter effect is considered to be more easily detectable, which becomes obvious after the derivation of the essential equations, as discussed below. Both parts of the magnetolectric effect in  $\text{Cr}_2\text{O}_3$  revealed the same linear dependence, manifest in the linear magnetolectric susceptibility  $\alpha_{ij}$ , in consistence with the theory and as presented in the following.

The linear ( $\alpha_{ij}$ , SI-unit: s/m) and higher order ( $\beta_{ijk}$ , SI-unit: s/A;  $\gamma_{ijk}$ , SI-unit: s/V) magnetolectric effects emerge from the coupling of electric ( $\mathbf{E} = (E_x, E_y, E_z)$ ) and

---

<sup>1</sup>French original: 'Enfin, lorsque certaines causes produisent certains effets, les éléments de symétrie des causes doivent se retrouver dans les effets produits.', see [3].

magnetic ( $\mathbf{H} = (H_x, H_y, H_z)$ ) fields in a material's free energy, given in its most general form as

$$\begin{aligned} \mathcal{F}(\mathbf{E}, \mathbf{H}) = & \mathcal{F}_0 - P_i^s E_i - M_i^s H_i - \frac{1}{2} \varepsilon_0 \varepsilon_{ij} E_i E_j - \frac{1}{2} \mu_0 \mu_{ij} H_i H_j \\ & - \alpha_{ij} E_i H_j - \frac{1}{2} \beta_{ijk} E_i H_j H_k - \frac{1}{2} \gamma_{ijk} H_i E_j E_k - \dots, \end{aligned} \quad (3.1)$$

where  $P^s$  ( $M^s$ ) represents the spontaneous polarization (magnetization),  $\varepsilon_0$  ( $\mu_0$ ) and  $\varepsilon$  ( $\mu$ ) is the dielectric permittivity (magnetic permeability) of vacuum and the material, respectively, and the indices  $i, j, k$  denote the summation over the three spacial coordinates. In most of the cases, considering a specific compound simplifies this general expression by neglecting the terms that are prohibited by the material symmetry. The electric polarization and magnetization can be deduced by differentiating the free energy with respect to the electric and magnetic field, respectively:

$$\begin{aligned} P_i(\mathbf{E}, \mathbf{H}) &= -\frac{\partial \mathcal{F}(\mathbf{E}, \mathbf{H})}{\partial E_i} \\ &= P_i^s + \varepsilon_0 \varepsilon_{ij} E_j + \alpha_{ij} H_j + \frac{1}{2} \beta_{ijk} H_j H_k + \gamma_{ijk} H_i E_j \dots \end{aligned} \quad (3.2)$$

$$\begin{aligned} M_i(\mathbf{E}, \mathbf{H}) &= -\frac{\partial \mathcal{F}(\mathbf{E}, \mathbf{H})}{\partial H_i} \\ &= M_i^s + \mu_0 \mu_{ij} H_j + \alpha_{ij} E_i + \beta_{ijk} E_i H_j + \frac{1}{2} \gamma_{ijk} E_j E_k \dots \end{aligned} \quad (3.3)$$

Here we only included the first higher order magnetoelectric terms ( $\beta_{ijk}, \gamma_{ijk}$ ), while we left out the third rank tensors for the purely electrically induced polarization ( $\mathcal{F}_{3,E} = 1/6 \delta_{ijk} E_i E_j E_k$ ) and magnetically induced magnetization ( $\mathcal{F}_{3,H} = 1/6 \eta_{ijk} H_i H_j H_k$ ) of the same order and all higher orders (e.g.  $d_{ijkl} E_i E_j H_k H_l$ , where  $d_{ijkl}$  is a fourth rank tensor).

### 3.1.1 Linear Magnetoelectric Effect

In most of the experimentally investigated MEEs, the linear coupling dominates and therefore allows for neglecting the higher order terms (the magnetoelectric susceptibility is then often replaced by the dimensionless susceptibility  $\chi_{ij}^{\text{ME}} = c \alpha_{ij}$ , where  $c$  is the speed of light). With this approximation the magnitude of the change in polarization by a magnetic field compared to the complementary effect can be estimated, via

$$\Delta P_i = \alpha_{ij} H_j \quad (3.4)$$

$$\Delta M_j = \frac{1}{\mu_0} \alpha_{ij} E_i. \quad (3.5)$$

For example an  $\alpha = 10 \text{ ps m}^{-1}$  (corresponds to  $\chi \approx 3 \cdot 10^{-3}$ ) would result for an applied magnetic field of  $\mu_0 H = 1 \text{ T}$  in a polarization of  $P \approx 8 \mu\text{C m}^{-2}$ , which is quite easy to measure with a voltmeter and samples of reasonable size, whereas a rather strong electric field of  $1000 \text{ V/mm}$  would only lead to an induced magnetization of  $\mu_0 \Delta M = 0.01 \text{ mT}$ , which calls for experiments with magnetometers with a considerable sensitivity (e.g. SQUID magnetometers). The symmetry of the linear MEE (equal coupling between magnetically induced polarization  $\Delta P_i(H_j) \propto \alpha_{ij}$  and electrically induced magnetization  $\Delta M_j(E_i) \propto \alpha_{ij}$ ) follows from the symmetry of second derivatives, which applies to the twice differentiable free energy  $\mathcal{F}$  (equation 3.1).

From Curie's first prediction of the MEE on, symmetry considerations were the main drivers for finding magnetoelectric compounds. The first symmetry requirement for a linear MEE is the lack of an inversion center, which limits the candidates of linear magnetoelectric materials to non-centrosymmetric compounds or a breaking of the inversion symmetry, for example by a spin ordering, as in the case of the antiferromagnetic  $\text{Cr}_2\text{O}_3$ . Explaining the need for this requirement, offers an opportunity to demonstrate Curie's principle: the separation of electric charges (which is achieved in the MEE by an applied magnetic field) is a non-centrosymmetric effect, i.e. no inversion center can be found that leaves the constellation untouched. If an inversion center could be found and defined with the coordinates  $(0, 0, 0)$  there would be for each charge at the coordinates  $(x, y, z)$  an identical charge at  $(-x, -y, -z)$ , which would contradict the emergence of charge separation. Using now Curie's principle, it can be concluded that the causes for this non-centrosymmetric effect have to be non-centrosymmetric as well, and can be found for example in the broken spatial inversion symmetry of the crystal structure. As mentioned above, Landau and Lifshitz found the necessity of breaking the time-reversal symmetry to allow for a linear MEE. This can be achieved externally by applying a magnetic field or by moving the sample. The latter was actually shown already in 1888 by Wilhelm Röntgen [2], more than 70 years before the finding of the intrinsic MEE, by the observation of a magnetization that arose in a moving dielectric placed in an electric field. The experiment consisted of a glass disc rotating between two capacitor plates, while the movement of a magnetic needle placed closely above the upper plate was observed with an optical setup. Opposing to this extrinsic breaking of the time-reversal symmetry, the intrinsic breaking of this symmetry is achieved in  $\text{Cr}_2\text{O}_3$  by the presence of the spontaneous long-range magnetic order in the material.

However, after the first experimental confirmation of the magnetoelectric effect the interest in this physical phenomenon grew sparse over several decades: the search for new compounds turned out to be complicated and the effect in the first investigated compounds was too weak ( $\text{Cr}_2\text{O}_3$ :  $\alpha \approx 4 \text{ ps m}^{-1}$ ) to be of any use for promising applications. Thin films of the ferrimagnetic material Yttrium Iron Garnet (YIG), which are investigated in this thesis in respect to the emergence of magnetic superradiance, also exhibit a considerably strong magnetoelectric effect [14] with a linear magnetoelectric susceptibility of  $\alpha \approx 30 \text{ ps m}^{-1}$  [15] and higher order contributions [16]. Only in the recent years, several compounds surpassed the value of  $\alpha > 100 \text{ ps m}^{-1}$ , like compounds

of the  $M_2\text{Mo}_3\text{O}_8$  ( $M =$  transition ion) [17] or the  $\text{RMnO}_3$  [18] crystal families. The largest linear MEE is considered to be exhibited by  $\text{TbPO}_4$  at low temperatures [19], with  $\alpha = 730 \text{ ps m}^{-1}$  [10].

The upper bound serves as a tool for the efficient search for materials that exhibit a strong linear MEE. It was first calculated for the dimensionless magnetolectric susceptibility to be  $\chi_{ij}^{\text{ME}} < \sqrt{\epsilon_{ii}\mu_{jj}}$  [20] and later refined by an approximation for materials with localized permanent magnetic moments [21] to satisfy

$$\chi_{ij}^{\text{ME}} < \sqrt{\chi_{ii}^E \chi_{jj}^M}, \quad (3.6)$$

with the electric and magnetic susceptibility

$$\chi_{ij}^E = \epsilon_{ij} - 1 \quad \text{and} \quad \chi_{ij}^M = \mu_{ij} - 1, \quad (3.7)$$

respectively.

### 3.1.2 Higher Order Magnetolectric Effects

Compared to the vast amount of publications about the linear magnetolectric effect, the observations of higher order effects are reported much more rarely, even though the symmetry requirements are less strict and allow for example a bi-linear MEE in non-centrosymmetric magnets with an intact time-reversal symmetry [22], as we will see in the following. The first measurement of a so-called 'paramagnetolectric effect', emerging from a non-zero  $\beta_{ijk}$ , which leads to a term in the free energy proportional to **EHH** ('**EHH** magnetolectric effect'), was reported in  $\text{NiSO}_4 \cdot \text{H}_2\text{O}$  in 1965 [23] and is considered to be the most thoroughly investigated higher order MEE [9]. Similar quadratic magnetolectric effects were reported for example in  $\text{BiFeO}_3$  [24] or  $\text{Pb}(\text{Fe}_{1/2}\text{Nb}_{1/2})\text{O}_3$  [25].

A second order<sup>2</sup> MEE emerging from a non-zero  $\gamma_{ijk}$  (giving rise to a non-zero term in  $\mathcal{F} \propto \mathbf{HEE}$ , which will be denoted therefore as '**HEE** magnetolectric effect') was measured in yttrium iron garnet [14; 16], which can be described as a magnetic field dependent electric susceptibility [27].

As discussed above, the linear MEE is only permitted in media with certain symmetry requirements that can be described by a subgroup of 58 magnetic point groups (out of the total 122 Shubnikov groups [28]). However, the symmetry requirements for the second order MEE are somewhat different. In general the **EHH** magnetolectric effect is permitted in the 66 Shubnikov groups, which also allow for the piezoelectric effect (coupling between mechanical stress and electric polarization in certain materials [29]),

---

<sup>2</sup>In the literature the notation of 'second order' magnetolectric effects is used inconsistently. In this thesis we will denote with 'second order' MEE those effects that arise from non-zero third rank magnetolectric susceptibilities (e.g.  $\beta_{ijk}$ ). Consequently 'third order' MEE are connected to ME susceptibilities of the fourth rank (e.g.  $\pi_{ijkl}$ ). This nomenclature is consistent with [26].

while the **HEE** magnetoelectric effect is possible in the 66 piezomagnetic (see e.g. [30]) crystal classes [16]. In other words, the **EHH** magnetoelectric effect is allowed in time symmetric media, while the spatial symmetry still has to be broken. On the other hand, the necessity for a broken time symmetry remains intact for the **HEE** magnetoelectric effect, but it is allowed in centrosymmetric materials.

The third rank tensors for the higher order ME susceptibilities in equation (3.1) has to be symmetric in the last two components, leading for example for the tensor of the **EHH** term in the free energy to

$$\frac{1}{2}\beta_{ijk}E_iH_jH_k = \frac{1}{2}\beta_{ikj}E_iH_kH_j, \quad (3.8)$$

which reduces the number of independent components of  $\beta_{ijk}$  (and similarly of  $\gamma_{ijk}$ ) from 27 to only 18 components, as argued by [10], and is therefore often replaced by only two indices, e.g.  $\beta_{i\nu}$  could replace  $\beta_{ijk}$ , where  $\nu$  takes on the values from 1 to 6, which represents the combinations  $jk = 11, 22, 33, 12, 13, 23$ .

Even magnetoelectric effects above the third order (see footnote 2) were already elaborated in the 1960's in the form of the piezomagnetolectric effect [31; 32], where the stress tensor  $\sigma_{ij}$  is considered in the free energy

$$\mathcal{F}(\mathbf{E}, \mathbf{H}, \sigma)^\pi = -\pi_{ijkl}E_iH_j\sigma_{kl} \quad (3.9)$$

leads to an expansion of equation (3.2) by a term

$$P_i^\pi = -\frac{\partial \mathcal{F}^\pi}{\partial E_i} = \pi_{ijkl}H_j\sigma_{kl}, \quad (3.10)$$

where  $\pi_{ijkl}$  is the piezomagnetolectric tensor.

In a similar way, the tensor  $d_{ijkl}$  was considered in the measurement of a third order MEE in a spin glass system ( $\text{Sr}_{0.98}\text{Mn}_{0.02}\text{TiO}_3$ ) [33], giving similar equations:

$$\mathcal{F}(\mathbf{E}, \mathbf{H})^d = -\frac{1}{2}d_{ijkl}E_iE_jH_kH_l, \quad (3.11)$$

$$P_i^d = -\frac{\partial \mathcal{F}^d}{\partial E_i} = d_{ijkl}E_jH_kH_l. \quad (3.12)$$

Even though the higher order MEE is often dominated by the linear contribution, cases of a considerably strong higher order effect are known, as reported in the recently studied holmium hexaborate  $\text{HoAl}_3(\text{BO}_3)_4$ , with a magnetically induced electric polarization of  $3600 \mu\text{C m}^{-2}$  at an applied field of 70 kOe [34], which is much larger than the polarization induced by comparable field strengths of linear magnetoelectrics. Another strong higher order MEE will be presented in Fig. 5.4 and discussed in Chapter 5.

### 3.1.3 Microscopic Mechanism

An overview about possible microscopic theories of the linear magnetoelectric effect is given in [35]. The mechanisms that can induce a change of the magnetic properties of a compound by an applied electric field are discussed with respect to the possible interactions.

#### Single-Ion Anisotropy

The direction of the spins of an ion in a crystal depends on the magnetic field and the single-ion anisotropy. The latter provides the direction of the easy axis or easy plane, i.e. the preferable direction of the spins, while the magnitude of the anisotropy is a measure for how strong this preference is. In many cases, the spins are assumed as 'Ising-spins', which means that they are either parallel or antiparallel to the easy axis. This approximation is feasible, when the single-ion anisotropy is large ( $\gg |\mathbf{B}|$ ). In this so-called 'Ising-limit' the MEE can only occur, if the direction of the easy axis changes, which can happen when the electric field induces a change of the local symmetry by a movement of the ions relative to their ligands. On the other hand, a vanishing single-ion anisotropy leads to 'free spins' without any preferred direction that can align parallel to the magnetic field. The spin anisotropy energy for the  $i$ -th ion can be assumed to be proportional to the second power of the effective spin moment ( $\mathbf{S}$ )

$$E_i^{\text{single}} \propto (S_i^\rho)^2, \quad (3.13)$$

for the coordinates  $\rho = x, y, z$ . In general all even powers of spin operators have to be considered (satisfying the time-reversal symmetry), but since in all magnetic point groups, which allow for a MEE, the second order term is non-zero and dominates, this approximation is sufficient [35].

#### Symmetric Superexchange

The orbital overlap of two neighboring magnetic ions influences the exchange integrals and energies. However, more commonly the interaction of two magnetic ions is mediated by a non-magnetic ion inbetween, which is the so-called 'superexchange'. In a symmetric configuration this contribution takes on the form of

$$E_{ij}^{\text{symm}} \propto \mathbf{r}_{ij}(S_i^\rho S_j^{\rho'} + S_i^{\rho'} S_j^\rho), \quad (3.14)$$

where  $\mathbf{r}_{ij} = \mathbf{r}_i - \mathbf{r}_j$  is the distance between the two ions at  $r_i$  and  $r_j$  and  $\rho, \rho' \in \{x, y, z\}$ . An application of an electric field could induce a movement of cation and anion in opposite directions and modify their electron wave function, which can cause a change of the orbital overlap and equation (3.14). In this way the mechanism could give rise to a MEE.

### Antisymmetric Superexchange

In crystals with low symmetry the superexchange configuration may not be symmetric, e.g. the exchange interaction is mediated by a non-magnetic ion, which does not lie in the center of the connecting line between the two magnetic ions. The antisymmetric exchange is only allowed to be non-zero when the inversion symmetry of the bond direction is broken, which can be achieved by polarizing or moving the ions relatively to the cell by an external electric field. The superexchange term can be written as the antisymmetric version of equation (3.14):

$$E_{ij}^{\text{anti}} \propto \mathbf{r}_{ij}(S_i^\rho S_j^{\rho'} - S_i^{\rho'} S_j^\rho). \quad (3.15)$$

This contribution was elaborated by Dzyaloshinsky [36] and Moriya [37], hence the prominent name 'Dzyaloshinsky-Moriya interaction', and is considered to be substantially weaker than the symmetric contribution. However, the absolute change of both contributions by the described mechanisms might be of the same order of magnitude [9].

### Dipolar Interaction

The magnetic dipolar interaction is a long-range and rather weak interaction, which is responsible for determining the domain size in ferromagnetic materials. However, a considerable change of magnetic anisotropy might be induced in a piezoelectric material by an applied electric field, when the distortion leads to a change of the magnetic dipole fields by moving the magnetic ions in a nonuniform way. This interaction leads to a contribution

$$E_{ij}^{\text{dipol}} \propto \frac{\mathbf{m}_i \mathbf{m}_j}{r_{ij}^3} - \frac{3(\mathbf{m}_i \mathbf{r}_{ij})(\mathbf{m}_j \mathbf{r}_{ij})}{r_{ij}^5} \quad (3.16)$$

including the magnetic dipole moment  $\mathbf{m}_i$  for the  $i$ -th ion [35].

### Zeeman energy

The  $\mathbf{g}$ -tensor (often simply denoted as  $g$ -factor) links the magnetic moment of a particle to its quantum angular momentum. In the case of an atom with a spin angular momentum  $\mathbf{S}$  and an orbital angular momentum  $\mathbf{L}$  the  $g$ -factor takes on the form of the Landé  $g$ -factor,  $g_J$ , which can be approximated with assuming the electron orbital  $g$ -factor  $g_L \approx 1$  and the electron spin  $g$ -factor  $g_S \approx 2$  as:

$$g_J \approx \frac{3}{2} + \frac{S(S+1) - L(L+1)}{2J(J+1)}, \quad (3.17)$$

where  $J = |\mathbf{J}|$  ( $L, S$  are accordingly defined) with the total angular momentum  $\mathbf{J} = \mathbf{L} + \mathbf{S}$ . It determines the splitting  $\Delta E_Z$  of two degenerate energy levels of an atom in a magnetic

field with strength  $B$ , i.e. the Zeeman effect

$$\Delta E_Z = g_J \mu_B B, \quad (3.18)$$

where  $\mu_B$  is the Bohr magneton.

Even though the  $\mathbf{g}$ -tensor can be assumed to be isotropic whenever the spin-orbit coupling can be neglected, it is anisotropic in the general case and depends on the wave functions of the ground states, which are determined by the local symmetry of the magnetic ions. An applied electric field can modify the wave functions, in the sense of displacing the electrons from the equilibrium position around the core, which leads to a change of orbital momentum. This effect of an induced change of the local crystal symmetry would result in a change of the  $\mathbf{g}$ -tensor due its described definition. The contribution of this interaction is proportional to the local or applied magnetic field  $\mathbf{B}$ :

$$E_i^{\text{Zeeman}} \propto \mathbf{B}^\rho g_i^{\rho\rho'} \mathbf{S}_i^{\rho'} . \quad (3.19)$$

This effect is responsible for one of the strongest linear MEE, as measured in  $\text{TbPO}_4$  [19].

### 3.1.4 Magnetoelectric Multiferroics

Multiferroics are defined as materials that show more than one 'ferroic' property in the same phase [38]. Those properties are ferroelasticity, ferrotoroidicity, ferroelectricity and ferromagnetism, which is usually expanded by antiferromagnetism (and ferrimagnetism). This combination of properties can give rise to a coupling between both ferroic orders in such a way, that the field associated with one ferroic property can influence or control the second ferroic property. For the presented work, the most interesting subgroup of multiferroics are magnetoelectric multiferroics, which are again a subgroup of magnetoelectric materials, as discussed above, and combine (anti-)ferromagnetic ordering with ferroelectric properties. However, it should be noted that magnetoelectric multiferroics can only be understood as a subgroup of magnetoelectrics in the presented definitions of the notions, as pointed out in [39]. Deviating definitions of 'multiferroics', where antiferromagnetism and -electricity are excluded, and 'magnetoelectrics', which are sometimes restricted to materials that exhibit the linear magnetoelectric effect ( $\alpha_{ij} \neq 0$ ), exist in literature.

The combinations of (anti-)ferromagnetic and (anti-)ferroelectric properties attracted much scientific attention, as recently discussed in [12], due to the associated promising applications, e.g. magnetoelectric memory [40]. Moreover, novel phenomena were observed in multiferroics, like coupled magnetoelectric excitations, so-called 'electromagnons', which were first observed in rare-earth manganites  $R\text{MnO}_3$  ( $R = \text{Rare earth}$ ) [41], electric conductivity in multiferroic domain walls [42], the optical magnetoelectric effect, or nonreciprocal directional dichroism, as observed for example in  $\text{GaFeO}_3$  [43]

and many more [11]. The most studied magnetoelectric multiferroic is  $\text{BiFeO}_3$ , which exceptional nature arises, among other intriguing features, from a reported large remanent polarization of  $\approx 55 \mu\text{C}/\text{cm}^2$  in the ferroelectric hysteresis loops and ferroelectric and antiferromagnetic order well above room temperature in thin film heterostructures [44]. While the magnetism in bismuth ferrite originates from  $d$ -electrons, some multiferroics based on  $f$ -electron magnetism are known, like  $\text{Eu}_{0.5}\text{Ba}_{0.5}\text{TiO}_3$  [45]. As an additional approach in the search for new multiferroics, composite materials of two individual ferroic compounds were created and investigated, which allow for the same coupling and effects as conventional magnetoelectric multiferroics. Examples for such a composite multiferroic is the combination of the ferroelectric  $\text{BaTiO}_3$  with the magnetic  $\text{CoFe}_2\text{O}_4$  [46], the multilayer  $\text{LuFeO}_3/\text{LuFe}_2\text{O}_4$  [47] and many more are discussed in recent reviews [9; 12; 48].

### 3.1.5 Applications

The investigation of magnetoelectric materials and especially magnetoelectric multiferroics is driven by the prospect of potential applications (e.g. [11]), and is focused on microelectronic devices [12]. Additionally, it should be mentioned that especially in the early years the research of the MEE was supported by the outlook of promising applications in basic research, e.g. for determining magnetic symmetries or observing antiferromagnetic domains [38].

One of the most prominent examples is the use of the voltage-control of the magnetization to build a magnetoelectric random access memory (MERAM), which can combine the advantages of ferroelectric RAM (ultrafast electrical write-operation) with magnetic RAM (non-destructive read-operation), as proposed in [40]. A short and simplified description of the disadvantages of conventional magnetic memories and conventional random access memories can illustrate the motivation behind the development of magnetoelectric RAM, as follows. Magnetic storage devices are based on a simple mechanism: The binary information is stored on a magnetized medium by translating a '0' into one direction of magnetization and a '1' into the opposite direction. Recording data is therefore achieved by applying a magnetic field focused at the position of the bit. The recording or reading over several bits is usually implemented mechanically. The mechanical movement limits the speed, which is the main disadvantage of such storage devices. Faster recording and saving sequences can be achieved by storing the data electrically on random access memory. In such devices the data does not have to be recorded and read out in a certain order, hence the name 'random access', and the processing speed is not limited by mechanical components. The data is stored on capacitors, which have to be refreshed constantly to prevent losing the data due to a slow discharge. Therefore this type of memory is considered a volatile storage device; when the power supply is switched off, all data is lost. A possible combination of the non-volatility of magnetic memories with the high speed that arises from electrically addressing the storage in a 'random access-type' memory is the main advantage of memory devices based on

magnetoelectric multiferroics. Even though the same is already achieved with different technologies (e.g. floating gate MOSFET), the imaginable information density that can be reached with the development of a MERAM is still promising for intriguing benefits. In fact, recent reports show a noteworthy progress in engineering such a device [49].

Other technological implementations that are already remarkably advanced on the path to practical applications, reach from weak magnetic field detection (e.g. [50]) to voltage-controlled phase shifters in the sub-THz frequency regime (e.g. [51]). Further ideas are discussed in several reviews [9; 11; 12; 39], including voltage-tunable magnetoresistance, electric field-tunable microwave signal processing, spin-wave generation and many more.

## 3.2 Theory of the Magnetoelectric Effect in Rare-Earth Ferroborates

Rare-earth ferroborates attracted first scientific attention around the turn of the century due to their promising optical features, which are especially interesting for optical applications [52], and unusual magnetic properties [53]. First experimental observations of a magnetoelectric effect were made in  $\text{GdFe}_3(\text{BO}_3)_4$  in 2005 [7], which lead to further publications about measurements of the magnetoelectric nature of different rare-earth ferroborate compounds (e.g. [54]) and the modeling of the magnetoelectric effect [6] in this magnetically rather complex system. The particular interest in this material group arises from the peculiarly strong MEE and the unusual combination of two single-ions mechanisms behind it.

Rare-earth ferroborates (general formula:  $R\text{Fe}_3(\text{BO}_3)_4$ ;  $R$  = rare-earth ion) belong to the hexagonal  $R32$  space group; rhombohedral with a threefold and a twofold symmetry axis perpendicular to each other. The magnetic properties emerge from the  $\text{Fe}^{3+}$  and  $R^{3+}$  subsystems, which are coupled by exchange-interaction. The iron ions order below the Néel temperature ( $T_N \approx 32$  K for  $\text{SmFe}_3(\text{BO}_3)_4$  and in the same range for the other compounds) into two subsystems with magnetization  $\mathbf{M}_1$  and  $\mathbf{M}_2$ . The rare-earth ions are split in the same way into two sublattices ( $q = 1, 2$ ), which are assumed to be coupled by the exchange interaction mostly to the  $\text{Fe}^{3+}$  subsystem  $\mathbf{M}_1$  and  $\mathbf{M}_2$ , respectively. This leads to a total effective magnetic field at the rare-earth sites

$$\mathbf{h}_q = \mathbf{H} + \lambda\mathbf{M}_q, \quad (3.20)$$

in an external magnetic field  $\mathbf{H}$ , where  $\lambda$  is the constant of the molecular field of the iron sublattices. This expression is expanded to account for the antiferromagnetic ordering of the iron sublattices and their saturation at a field  $H_{\text{sat}} \approx 10^6$  Oe, leading to an effective

magnetic field

$$\mathbf{h}_q = \left( \frac{H_{\text{mol}}}{H_{\text{sat}}} \right) H \mathbf{e}_x + (-1)^q H_{\text{mol}} \sqrt{1 - \left( \frac{H}{H_{\text{sat}}} \right)^2} \mathbf{e}_y, \quad (3.21)$$

when the external field is applied along the  $a$ -axis. Here the strength of the molecular field  $H_{\text{mol}} = \lambda M_q$  was extracted to be  $H_{\text{mol}} = 50 \text{ kOe}$  for  $R = \text{Nd}$  ferroborate [55]. For  $R = \text{Sm}$  ferroborate it was estimated to be  $H_{\text{mol}} = 330 \text{ kOe}$  [6].

In the rare-earth ions the magnetism arises from the  $4f$ -electrons, which energy levels are degenerate in free space. However, assuming a rare-earth ion in a crystal, this degeneracy may be split by the electronic surrounding. This influence of the charge distribution on the magnetic ion is described by the crystal field Hamiltonian  $\mathcal{H}_{\text{CF}}$ , which takes on the general form

$$\mathcal{H}_{\text{CF}} = \sum_{t\tau k} B_\tau^t C_\tau^t(k), \quad (3.22)$$

where  $k$  is the wave vector,  $B_\tau^t$  are the crystal field parameters, which are usually determined by symmetry considerations and experimental techniques (e.g polarized absorption spectroscopy) and  $C_\tau^t(k)$  are the single-electron irreducible tensor operators, which describe the electron orbital configuration and are defined by the Laplace spherical harmonics<sup>3</sup>  $Y_\tau^t$

$$C_\tau^t(k) = \sqrt{\frac{4\pi}{2t+1}} Y_\tau^t(\theta, \phi), \quad (3.23)$$

which are defined as

$$Y_\tau^t(\theta, \phi) = \sqrt{\frac{(\tau-t)!}{(\tau+t)!}} P_\tau^t(\cos\theta) e^{it\phi} \quad (3.24)$$

where  $k$  is replaced by the two angles  $\theta$  and  $\phi$  and the associated Legendre polynomials of the order  $\tau$  and the power  $t$  are given as<sup>4</sup>

$$P_\tau^t(x) = (-1)^t (1-x^2)^{t/2} \frac{d^t}{dx^t} (P_\tau(x)), \quad (3.25)$$

where  $P_\tau(x)$  are the Legendre polynomials of order  $\tau$ . The non-zero crystal field parameters can be identified by considering the symmetry of the rare-earth sites, which are characterized by the  $D_3$  symmetry around the crystallographic  $c$ -axis (in the Cartesian system  $z$ ), which leaves us with

$$\mathcal{H}_{\text{CF}} = B_0^2 C_0^2 + B_0^4 C_0^4 + B_0^6 C_0^6 + iB_{-3}^4 (C_{-3}^4 + C_3^4) + iB_{-3}^6 (C_{-3}^6 + C_{-3}^6) + B_6^6 (C_6^6 + C_{-6}^6). \quad (3.26)$$

<sup>3</sup>In the literature the indices  $lm$  are used more commonly. The notation  $t\tau$  is used in consistency with [6] to prevent a confusion with the quantum numbers  $l$  and  $m$ .

<sup>4</sup>For the sake of simplicity, we only give the polynomials for  $\tau \geq 0$ .

As discussed previously, the magnetic field and temperature dependence of the electrical polarization is derived by considering the free energy, which emerges from the Hamiltonian describing the system. The complete derivation is rather complex and can be found in [6]. We will give here the final expressions for the electric polarization along the two in-plane axes  $x, y$ :

$$P_x = Qg_J\mu_B \sum_{q=1,2} h_q \chi(\mathbf{h}_q, T) (C_1(\gamma_{qy}^2 - \gamma_{qx}^2) - C_2\gamma_{qy}\gamma_{qz}) \quad (3.27)$$

$$P_y = Qg_J\mu_B \sum_{q=1,2} h_q \chi(\mathbf{h}_q, T) (2C_1\gamma_{qx}\gamma_{qy} + C_2\gamma_{qx}\gamma_{qz}). \quad (3.28)$$

Here  $Q$  is a constant, depending on the number of rare-earth ions and the distribution of energy levels of their electronic configuration;  $h_q$  is the absolute value of the effective magnetic field, which is given by Eq. (3.20);  $C_{1,2}$  are two constants, which are calculated to be  $C_1 = 4.92$  and  $C_2 = 7.09$  for samarium ferroborate;  $\gamma_{q\alpha}$  are the three components ( $\alpha = x, y, z$ ) of the unit vector along the effective magnetic field  $\mathbf{h}_q/h_q$ ; and finally the Brillouin function

$$\chi(\mathbf{h}_q, T) = \frac{1}{\Delta_q} \tanh\left(\frac{g_J\mu_B h_q}{k_B T} \Delta_q\right), \quad (3.29)$$

where the dimensionless anisotropy factor is given as

$$\Delta_q = \sqrt{g_{\parallel}^2 \gamma_{q\parallel}^2 + g_{\perp}^2 \gamma_{q\perp}^2}. \quad (3.30)$$

Here the magnetic spectroscopic factors for  $\text{SmFe}_3(\text{BO}_3)_4$  are  $g_{\parallel} = 0.379$  and  $g_{\perp} = 1.441$ , where  $\parallel, \perp$  denotes the components along and perpendicular to the  $c$ -axis, respectively. Unfortunately, the origin of these values is not indicated in [6].

Eq. (3.27) is used for fitting the high-field behavior of the magnetically induced polarization in samarium ferroborate, as seen in Fig. 4.3 and explained in Chapter 4.1.

The presented approximation does not account for a magnetically induced polarization along the crystallographic  $c$ -direction, due to neglecting higher order terms in the applied perturbation theory [6].

### 3.3 Summary

The magnetoelectric effect is the coupling of magnetic and electric properties in a solid. In the linear magnetoelectric effect the electrically induced magnetization is proportional to the applied electric field and vice versa. Higher orders, however, can lead to a more complex proportionality. The possible microscopic mechanisms that can lead to these effects span from the interaction of magnetic ions to a change of the single-ion anisotropy. Research for magnetoelectric materials attracted scientific interest throughout the past decades and offers the realization of many intriguing potential applications in microelec-

tronics. The presented theory of the magnetoelectric effect in rare-earth ferroborates is applied in the next chapter for  $\text{SmFe}_3(\text{BO}_3)_4$ .



# 4 Magnetolectric Effect in Samarium Ferroborate

As discussed in Chapter 3, rare-earth iron borates attracted much scientific attention due to the discovery of a strong magnetolectric effect, which is already extensively studied and well described by a quantum theory [6], as outlined in Chapter 3.2. Nevertheless, we were able to contribute to this field of research by two sets of measurement on  $\text{SmFe}_3(\text{BO}_3)_4$ . Firstly, our measurements provided new insights into the high-field behavior of the magnetically induced electric polarization along the crystal's  $a$ -axis,  $P_a$ , by an in-plane magnetic field. The experimental determination of the  $g$ -factor of the samarium ions in this system is noteworthy, since the values reported in literature are inconsistent (e.g. [6; 56]). Difficulties in determining the samarium  $g$ -factor arise from its rather small value. However, we present a method to accurately determine the  $g$ -factor with an error of only about one percent. Secondly, we observed an induced electric polarization along the crystallographic  $c$ -axis,  $P_c$ , corresponding to a MEE of the sixth order.

## 4.1 High-Field Magnetolectric Effect

The measurement of the high-field magnetolectric effect in [54] reveals not only a saturation of  $P_a$  for small magnetic fields along  $a$ - and  $b$ -axis, but also shows a decrease at fields above 5 T, which is accounted for in the theory by modifying the effective magnetic field (Eq. 3.21) with the introduced Fe-Sm molecular field of the strength  $H_{\text{mol}} = 330 \text{ kOe}$  [6]. However, theory and experiment did not show a perfect agreement and called for further investigations. Unfortunately, the origin of the chosen molecular field strength within [6] remains unclear and we will show that the actual value has to be modified. With this newly determined  $H_{\text{mol}}$ , the  $g$ -factor of the samarium-ions in this system can be calculated, based on the optically obtained value for the splitting of the ground state of  $\Delta = 13.2 \text{ cm}^{-1}$  [57]. The  $g$ -factor that will be determined in the following is more accurate than the strongly varying literature values ([6]:  $\approx 0.412$ , [56]:  $\approx 0.679$ ). In this section we only deal with the  $\perp$ -component of the  $g$ -factor (see Chapter 3.2).

We extend the discussed observations with measurements in a PPMS with static magnetic fields along the crystal's  $b$ -axis of up to 14 T (Chapter 2.2) and in a pulsed magnetic field with a strength of up to 56 T, where the decrease in polarization becomes more pronounced and thus gives additional data to determine the exact parameters  $H_{\text{mol}}$

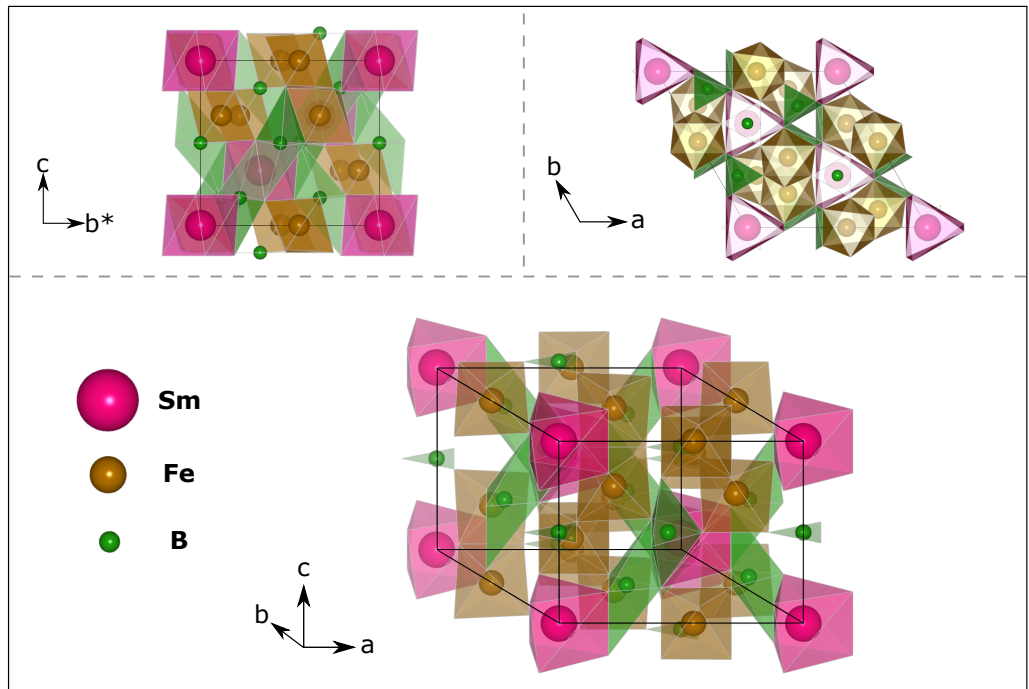


Figure 4.1: Structure of SmFe<sub>3</sub>(BO<sub>3</sub>)<sub>4</sub>. The oxygen-ions coordinating the cations are located at the corners of the polyhedra. Three different directions are shown: a three dimensional view (bottom) and the *a*-cut (top left) and *c*-cut (top right) directions. The compound consists of alternating layers of Sm-Fe and B-O ions along the *c*-direction.

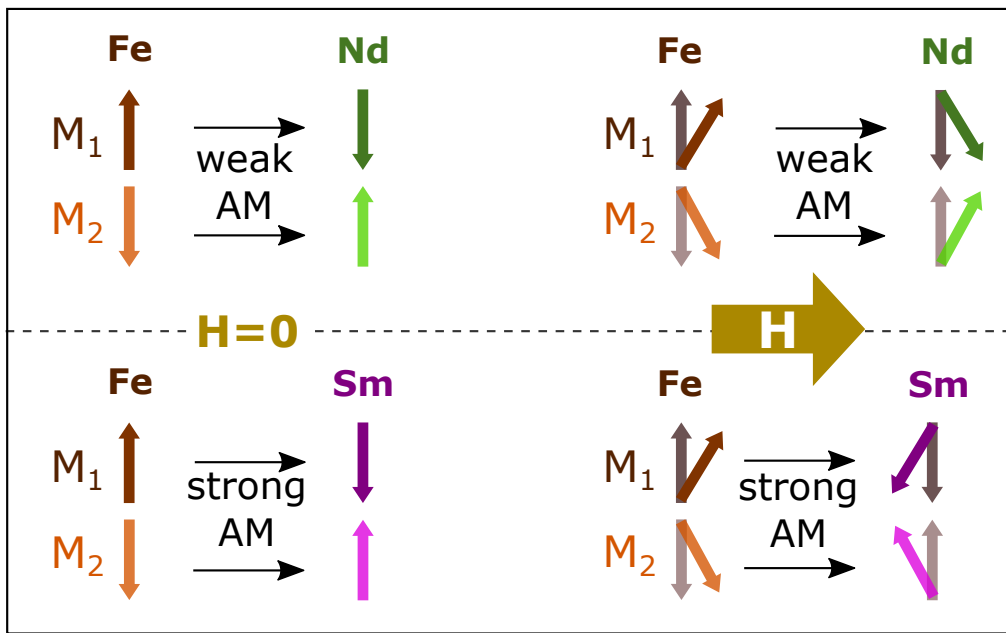


Figure 4.2: Illustration of the coupling as described in Chapter 3.2 between the rare-earth magnetic moments to the two magnetic iron subsystems  $M_1$  and  $M_2$ . This coupling is found to be antiferromagnetic [58]. However, the strength of this coupling can vary strongly in the different compounds of the rare-earth-ferroborate family. This simplified sketch demonstrates that the weakly coupled neodymium moments cant into the direction of the applied field of  $\mu_0 H > 5$  T, while the antiferromagnetic coupling of the samarium moments to the iron sublattices dominates for fields below  $\ll H_{\text{mol}}$ , which is determined in Table 4.1.

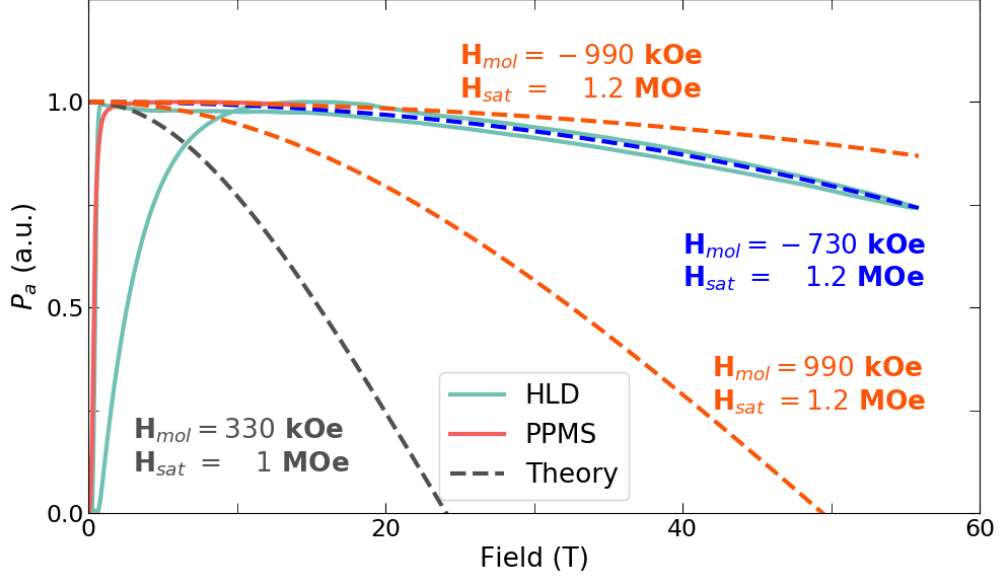


Figure 4.3: The electric polarization along the  $a$ -axis of  $\text{SmFe}_3(\text{BO}_3)_4$  induced by a magnetic field along the crystal's  $b^*$ -axis around 2 K (PPMS,  $T=2.2$  K; HLD,  $T=1.5$  K). Different parameters for describing the effective magnetic field in Eq. (3.21) were used, as discussed in the text.

and  $H_{\text{sat}}$ , i.e. the field on which the iron ions saturate, for this system.

In Fig. 4.3 the high-field electrical polarization  $P_a$  induced by a static and pulsed magnetic field is shown and compared with different sets of parameters of the molecular field  $H_{\text{mol}}$  and the saturation field  $H_{\text{sat}}$ . These parameters determine the effective magnetic field on the rare-earth ions, as expressed in Eq. (3.21), and thereby the polarization along the crystallographic  $a$ -axis (Eq. 3.25). It becomes evident that the parameters suggested in [6] ( $H_{\text{mol}} = 330$  kOe,  $H_{\text{sat}} \approx 1$  MOe) are not suited to describe the experimentally obtained magnetoelectric effect. To find a better set of parameters, we analyzed the magnetization curves as published in [59], which can be extrapolated to estimate a value for the saturation field of the iron-ions, i.e. the spin-flip field  $H_{\text{sat}}$ . The  $g$ -factor of the  $\text{Fe}^{3+}$ -ions is best approximated with the spin-only value  $g_{\text{Fe}} = 2$  (e.g. [60]), the spin moment is  $S_{\text{Fe}} = 5/2$  and taking into account the three iron sites in the unit cell, the saturation value of the magnetization can be assumed to be

$$M_{\text{sat}} = 3g_{\text{Fe}}S_{\text{Fe}} = 15 \frac{\mu_{\text{B}}}{\text{f.u.}}. \quad (4.1)$$

This extrapolates with a magnetization of  $1 \frac{\mu_{\text{B}}}{\text{f.u.}}$  at approximately 7.8 T [59] to a saturation field of  $H_{\text{sat}} \approx 1.2$  MOe.

For a first assumption of the Fe-Sm molecular field, the splitting of the ground state by  $\Delta = 13.2 \text{ cm}^{-1}$ , as obtained in [57], is taken into account. Namely, the degenerate

ground state (Kramers doublet) of the  $\text{Sm}^{3+}$ -ion is split by the local effective field of the Fe ions. With a  $g$ -factor of samarium  $g_{\text{Sm}}$  equal to the Landé value  $g_{J,\text{Sm}} = 2/7$  this would correspond, related by the so-called Larmor precession, to a strength of

$$H_{\text{mol}} = \frac{hc}{g_{\text{Sm}}\mu_{\text{B}}\mu_0} \Delta \approx 990 \text{ kOe}, \quad (4.2)$$

where  $h$  is the Planck constant.

Furthermore, the sign of the coupling between the samarium- and the iron-ions needs to be considered. By studying the possible exchange paths between rare-earth and iron ions, [58] concludes that the coupling is antiferromagnetic in gadolinium ferrobortate. This fits very well to the increase of the magnetization when admixing La-ions on the Sm-sites [59], indicating an antiferromagnetic coupling of Sm- and  $\text{Fe}^{3+}$ -ions. This can be considered in the effective magnetic field by an opposite sign of  $H_{\text{mol}}$  and  $H_{\text{sat}}$ . However, the set of parameters, which were estimated based on the literature, does not give a good agreement between theory and experiment (orange curves in Fig. 4.3). The most likely conclusion is that the molecular field  $H_{\text{mol}}$  is deviating from Eq. (4.2), because the Sm  $g$ -factor differs from the Landé value  $g_{\text{Sm}} \neq 2/7$  and the value of 0.412 as assumed in [6]. Therefore, we extract its actual value by fitting our data with a fixed spin-flip field and a fixed splitting  $\Delta$ . The result for the different theoretical curves, as shown in Fig. 4.3 are given in Table 4.1, including the refined value of the samarium  $g$ -factor of  $\approx 0.39$ , which is substantially larger than the originally assumed value ( $g_{J,\text{Sm}} = 2/7 \approx 0.29$ ). The error in the fit is considerably small and only of about 1%. The experimental error is also small, since only relative field strengths play a role in this analysis. Therefore we can conclude that the presented value of  $g_{\text{Sm}}$  is accurate and can replace the strongly varying literature values.

	[6]	[57] & [59]	Fit
$\Delta$	<b>6.3 cm<sup>-1</sup></b>	<b>13.2 cm<sup>-1</sup></b>	<b>13.2 cm<sup>-1</sup></b>
$g_{\text{Sm}}$	<b>0.412</b>	2/7	0.388
$H_{\text{mol}}$	<b>330 kOe</b>	<b>990 kOe</b>	<b>730 kOe</b>
$H_{\text{sat}}$	<b>1 MOe</b>	<b>1.2 MOe</b>	<b>1.2 MOe</b>

Table 4.1: Different parameters for fitting the electrical polarization  $P_a$  induced by a high magnetic field. Bold values were fixed, based on literature values and estimations, as discussed in the text. The value of  $\Delta$  in the first column is derived in accordance to the values given for  $g_{\text{Sm}}$  and  $H_{\text{mol}}$  in [6]. The Sm-Fe molecular field  $H_{\text{mol}}$  depends on the samarium  $g$ -factor  $g_{\text{Sm}}$  and its splitting  $\Delta$ , which is fixed to  $13.2 \text{ cm}^{-1}$  for the last two columns. In the last column the molecular field was fitted (blue) to estimate the actual  $g$ -factor.

## 4.2 Induced Polarization along the $c$ -axis

So far only the magnetoelectric effect with an electric polarization along the  $a$ -axis of rare-earth ferroborates has been reported in the literature. Nevertheless, a possible occurrence of a magnetically induced  $P_c$  is already mentioned in [6]. Here we report the experimental observation of this higher order MEE and show that it satisfies a simple phenomenological model, based solely on symmetry arguments. The observed effect is very similar to the MEE in  $\text{Ho}_x\text{La}_{3-x}\text{Ga}_5\text{SiO}_{14}$ , which will be discussed in Chapter 5, where a microscopic model is developed. However, the simple symmetry-based model is sufficient to provide a first explanation of the effect in  $\text{SmFe}_3(\text{BO}_3)_4$ .

The similarity of the MEE in both compound families can be understood by the two different space groups, which share an important feature: in space group  $P321$  (langasites) and  $R32$  (ferroborates) the threefold  $c$ -axis and the twofold symmetry axis perpendicular to  $c$  are present. Therefore it can already be concluded that any polarization along the threefold axis induced by a magnetic field, which is rotated in the  $ab$ -plane has to satisfy at least a sixfold symmetry, which emerges from the crystal's (threefold) and the time reversal symmetry of the electric polarization (twofold). Due to the twofold symmetry axis along  $a$ , no  $P_c$  can be expected when the magnetic field is applied along the main crystallographic axes  $a, b, c$ . Therefore the magnetic field was rotated in steps of  $5^\circ$  in the  $ab$ -plane to search for this higher order magnetoelectric effect. And indeed we were able to experimentally obtain an electric polarization along the crystal's  $c$ -axis, as shown in Fig. 4.4.

However, the polarization is so small that it is likely dominated from a stray polarization along the  $a$ -axis, since  $P_a$  is already for rather low fields in the range of several hundred  $\mu\text{C m}^{-2}$ . To remove this distortion of the signal, the twofold symmetry of  $P_a$  was used, which emerges when the magnetic field is rotated in the  $ab$ -plane. Therefore the  $P_c$  was extracted by subtracting the angular dependence with a  $\sin(2\phi)$  fit. We were able to show (Fig. 4.5) that the resulting polarization along the  $c$ -axis convincingly satisfies the expected sixfold symmetry, as argued above. It is noteworthy that the values of  $P_c$  decrease for larger fields. This cannot be explained by the presented simple model and, therefore, calls for an approach considering the microscopic magnetic structure of  $\text{SmFe}_3(\text{BO}_3)_4$ .

## 4.3 Summary

In this Chapter, we successfully refined the theory of the magnetoelectric effect in rare-earth ferroborates [6]. With the literature values for the splitting of the lowest lying doublet,  $\Delta$ , and the saturation field,  $H_{\text{sat}}$ , we extracted the molecular field,  $H_{\text{mol}}$ , by fitting the high-field magnetoelectric effect. This led to an accurate determination of the samarium  $g$ -factor. Furthermore, we were able to show the presence of a higher-order MEE for  $P_c$ .

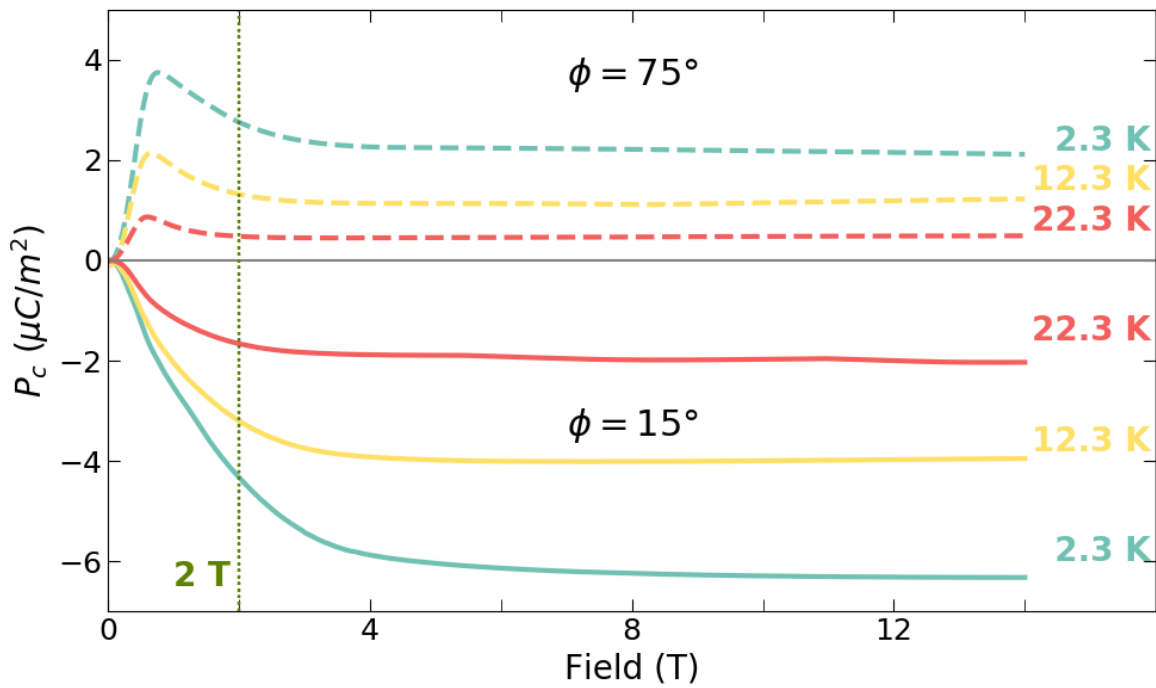


Figure 4.4: The electric polarization along the  $c$ -axis of  $\text{SmFe}_3(\text{BO}_3)_4$  induced by a magnetic field applied in the  $ab$ -plane with an angle of  $15^\circ$  (solid) and  $75^\circ$  (dashed) to the  $a$ -axis, respectively. The angular dependence were extracted from these and further measurements by reading out the polarization at different temperatures (color) and different fields (2 T and 14 T) and are analyzed in Fig. 4.5.

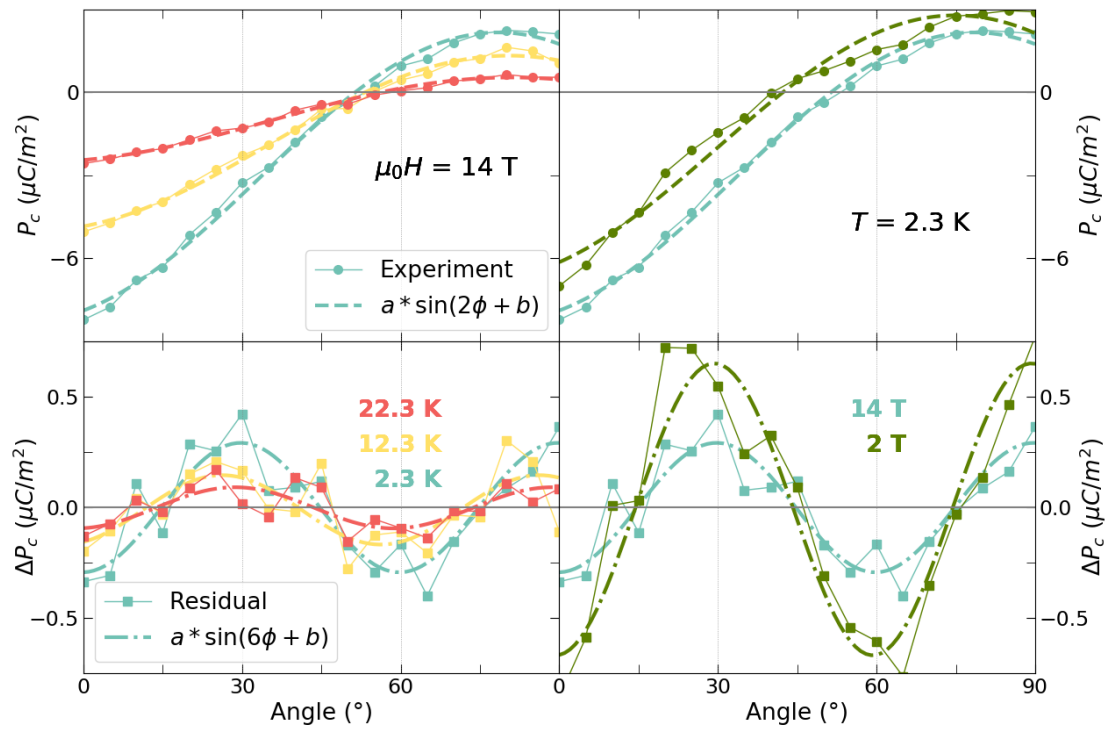


Figure 4.5: Analysis of the electric polarization along the  $c$ -axis induced by magnetic fields rotated in the crystal's  $ab$ -plane for different temperatures at a fixed magnetic field (left) and different field strengths at a fixed temperature (right), respectively. The theoretical lines (dashed) are simple fits with sine curves. The residual  $\Delta P_c$  (bottom) is the difference of the experimental curve (top) and the corresponding fit.

# 5 Magnetic Properties and the Magnetoelectric Effect in Ho-Langasite

The finding of a puzzling combination of a linear and a higher order MEE in holmium-doped langasite [61] motivated a thorough investigation of the magnetic properties of this compound. The main features of the dependence of the induced electric polarization on the magnetic field vector can be explained by a simple phenomenological model, which will be introduced in Chapter 5.1. However, no perfect agreement with the low-temperature magnetoelectric effect and magnetization curves is achieved and further inconsistencies are revealed by measurements of the angular dependence of the magnetization and the magnetic torque, as presented in Chapter 5.2. Therefore the first approximation will be extended in Chapter 5.2 by taking into account a more complex magnetic structure. These studies led to the unexpected discovery of the magnetic field sensitivity of a strong low-frequency phonon, which exhibits some sensitivity to magnetic fields, as discussed in Chapter 5.3.

## 5.1 Simple Phenomenological Model of the Magnetoelectric Effect

We present the experimental study of the holmium-doped langasite  $\text{Ho}_x\text{La}_{3-x}\text{Ga}_5\text{SiO}_{14}$ , which exhibits a puzzling combination of linear and highly non-linear magnetoelectric responses in the disordered paramagnetic state, as published in [61]. While the magnetic field scans of the electric polarization show quasi-linear dependence, the induced polarization oscillates six times upon the rotation of the magnetic field vector. Even though straightforward symmetry considerations are sufficient to qualitatively describe the observed angular dependence, a derivation of the phenomenological Hamiltonian based on the microscopical mechanisms is necessary, to be able to explain the obtained combination of a linear and higher-order MEE.

### 5.1.1 Holmium Langasite

Langasite,  $\text{La}_3\text{Ga}_5\text{SiO}_{14}$ , and related compounds were first synthesized in the 1980s in Russia and actively studied since then for a wide range of interesting properties, as their

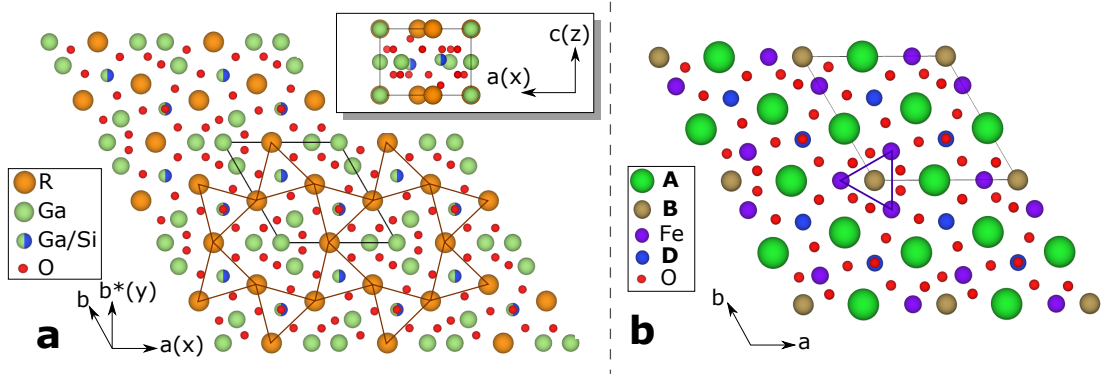


Figure 5.1: The structure of rare-earth langasite with the general formula  $R_3Ga_5SiO_{14}$  (a) and iron containing langasite with the general formula  $A_3BFe_3D_2O_{14}$  (b). The lines illustrate the antiferromagnetic interactions that give rise to a geometric frustration of the rare-earth ions on the distorted kagomé lattice (left) and the iron ions on the triangle lattice (right).

non-linear optical, elastic and piezoelectric properties [62; 63], and associated applications, with early implementation as surface and bulk acoustic wave filters [64]. Various high-temperature piezoelectric applications, including gas sensing and deposition rate monitoring for vapor-phase deposition, were suggested for bulk acoustic wave resonators, which can operate at up to 900 °C [65] or further high-temperature applications, like sensing pressure, force and acceleration [66]. The recent progress in electro-optical applications is also noteworthy, as reported for example in [67; 68].

The compounds of the langasite family belong to the non-centrosymmetric crystallographic space group  $P321$ , which allows for optical rotation and piezoelectricity, but not for spontaneous electric polarization due to the presence of orthogonal threefold and twofold symmetry axes, which can easily be identified in the structure [69; 70], visualized in Fig. 5.1.

The study of magnetoelectric properties was focused on Fe-substituted langasites (general formula:  $A_3BFe_3D_2O_{14}$ , where  $A$ ,  $B$ ,  $D$  denote the three substitutable cation sites) showing non-collinear periodically modulated orders of Fe-spins [71]. The interplay between magnetic frustration, structural and spin chiralities gives rise to a rich variety of multiferroic behaviors in these compounds [72; 73]. The magnetic frustration does not only play a role in the Fe-langasite, where the antiferromagnetically interacting  $Fe^{3+}$ -ions lie on the three corners of an equilateral triangle in the crystallographic  $ab$ -plane, as visualized in Fig. 5.1b, but also in rare-earth langasites, where the magnetic ions form in the  $ab$ -plane a distorted kagomé lattice [70], i.e. corner sharing triangles (Fig. 5.1a), which can give rise to exotic low temperature effects like a spin-liquid phase [74; 75]. However, in the compound that this work is focused on, the rare-earth site is mostly occupied by non-magnetic ions (La) and only a small percentage of magnetic ions (Ho),

lifting the geometric frustration.

The investigated samples are single crystals of magnetically diluted holmium langasite:  $\text{Ho}_x\text{La}_{3-x}\text{Ga}_5\text{SiO}_{14}$ , with  $x = 0.043 \pm 0.005$ , which were grown by the Czochralski technique. For the electric polarization experiments a plane-parallel plate with thickness  $d = 2.13 \text{ mm}$  and area  $A = 106 \text{ mm}^2$  has been cut with the flat surfaces of the sample parallel to the  $ab$ -plane. Additional samples of smaller size were used for the preliminary VSM measurements, originating from the same batch. The crystals were proven to be right-handed single domain [64; 69], which is likely a result of the growth procedure. This was confirmed by obtaining a homogeneous polarization rotation of about  $5^\circ$  for green light along the crystallographic  $c$ -axis for the described sample, which is in reasonable agreement with the literature data [76].

Within the unit cell of Ho-langasite there are three equivalent rare-earth positions ( $R=\text{La}, \text{Ho}$ ) with a rather low  $C_2$ -symmetry along the  $a$ -axis of the crystal, allowing for electric dipole moments on  $R$ -sites, which in the case of magnetic Ho-ions can depend on an applied magnetic field. The electronic configuration of the  $\text{Ho}^{3+}$ -ions is  $4f^{10}$  and the ground state is  $^5I_8$ .

The local axes are denoted with  $\hat{X}_i, \hat{Y}_i, \hat{Z}_i$  for the three sites, distinguished by  $i = 1, 2, 3$ , with local  $C_2$ -symmetry axes along  $\hat{Z}_i$ , which are related by  $120^\circ$ -rotations around the crystallographic  $c$ -axis ( $C_3$  symmetry axis). For  $i = 1$  the axes are chosen in such a way that the following relation between the unit vectors in the hexagonal  $(a, b^*, c)$ , Cartesian  $(x, y, z)$  and the three local frames holds:

$$\begin{cases} \hat{Z}_1 &= \hat{\mathbf{a}} &= \hat{\mathbf{x}}, \\ \hat{X}_1 &= \hat{\mathbf{b}}^* &= \hat{\mathbf{y}}, \\ \hat{Y}_1 &= \hat{\mathbf{c}} &= \hat{\mathbf{z}}. \end{cases} \quad (5.1)$$

On all three sites  $\hat{Y}_i = (0, 0, 1)$  in the Cartesian coordinates,  $\hat{Z}_{2,3} = (-\frac{1}{2}, \pm\frac{\sqrt{3}}{2}, 0)$  and  $\hat{X}_{2,3} = (\mp\frac{\sqrt{3}}{2}, -\frac{1}{2}, 0)$ .

### 5.1.2 Magnetization

The Ho-doped langasite is paramagnetic and does not order down to the lowest temperatures. However, the magnetization saturates already at fields  $\approx 1 \text{ T}$  at low temperatures, inducing a long-range order. These small saturation fields suggest that the magnetism of the  $\text{Ho}^{3+}$ -ions is dominated by the two lowest-energy levels split by the crystal field from the other states of the  $J = 8$  multiplet. The level splitting  $\Delta$  in this so-called non-Kramers doublet<sup>1</sup> is estimated to be 3.1 K. A more accurate value is extracted by quasi-optical measurements of the paramagnetic resonance (Chapter 5.2.5) and will be implemented in the expansion of the presented model in Chapter 5.2. The magnetic moments of the Ho-ions are assumed to be of Ising-type. The magnetic field dependence

---

<sup>1</sup> $\text{Ho}^{3+}$  has an even number of  $f$ -electrons and is therefore considered a non-Kramers ion.

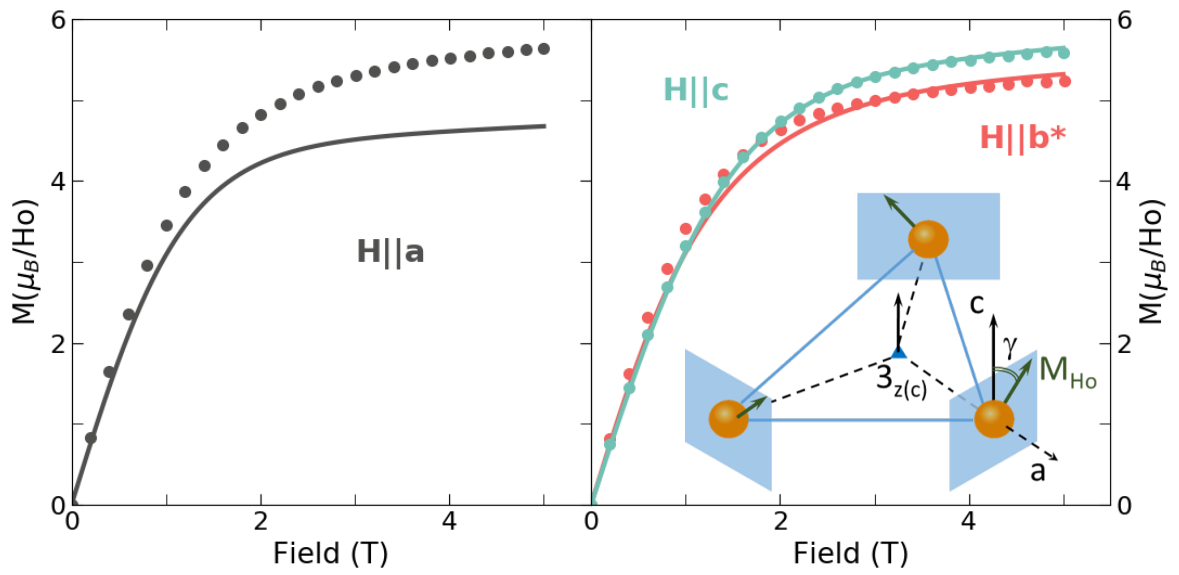


Figure 5.2: Magnetization curves as obtained in a vibrating sample magnetometer along the main crystallographic axis (dots) at a temperature of 5 K. The magnetization for  $\mathbf{H} \parallel \mathbf{a}$  (left) was separated from the two other axes for the sake of clarity. The derivation of the theoretical curves (lines) is explained in the text.

**Inset:** Visualization of the magnetic moments on the three equivalent Ho-sites in the unit cell, as assumed for developing the model.

of the magnetization along the main crystallographic axes are shown in Fig. 5.2. As discussed below, due to the  $C_2$ -symmetry at the Ho-sites, only two options are considered for the direction of the magnetic moments: either parallel or perpendicular to the local  $\hat{Z}_i$ -axes. Since a non-zero magnetization was obtained along the crystallographic  $c$ -direction, the moments are assumed to lie within the  $\hat{X}_i\hat{Y}_i$ -plane, with an angle  $\gamma \approx 30^\circ$  with the crystallographic  $c$ -axis fitting the magnetization data the best.  $\gamma$  is the only free magnetic anisotropy parameter in our model that reproduces well the field dependence of the magnetization along the  $b^*$ - and  $c$ -axes (see Fig. 5.2), but underestimates the magnetization for  $H\|a$ , which is indicative of deviations of the magnetic moments from the  $X_iY_i$ -plane (see discussion below). However, a different approach for the magnetic anisotropy will be presented in Chapter 5.2.

### 5.1.3 Magnetoelectric Effect

Fig. 5.3 shows the angular dependence of the electric polarization along the  $c$ -axis,  $P_c$ , for the magnetic field vector,  $\mathbf{H}$ , rotated in the  $ac$ - and  $ab$ -planes. The complex angular dependence is indicative of a high-order MEE resulting from the  $C_3$  symmetry of langsite. Although the expansion of the magnetically-induced electric dipole of the Ho-ion in powers of  $H$  begins with terms  $\propto H^2$ , the bilinear MEE is cancelled in the sum over the dipole moments of the Ho-dopants in the three La sublattices.

The lowest-order phenomenological expression for  $P_c$  allowed by  $C_3$  and  $C_2$  symmetries is

$$P_z^{(4)} = a_4(T)H_xH_z(H_x^2 - 3H_y^2), \quad (5.2)$$

where we use the Cartesian coordinates with  $\hat{\mathbf{x}} = \hat{\mathbf{a}}$ ,  $\hat{\mathbf{y}} = \hat{\mathbf{b}}^*$ ,  $\hat{\mathbf{z}} = \hat{\mathbf{c}}$  and  $a_4(T)$  is a material constant. Fourth-order MEE in crystals with trigonal crystal symmetry have been discussed earlier [55; 77; 78]. Eq. (5.2) implies that  $P_z \propto \sin^2\theta \sin 2\theta \cos 3\varphi$ , where  $\theta$  and  $\varphi$  are, respectively, the polar and azimuthal angles describing the magnetic field direction. This angular dependence is in good agreement with the results of experimental measurements at high temperatures shown in Fig. 5.3a, whereas at low temperatures the experimental  $\theta$ -dependence becomes more complex, indicating substantial higher-order contributions to the MEE.

The fourth-order MEE described by Eq. (5.2) gives zero electric polarization for a magnetic field in the basal  $ab$ -plane. However, the experimentally measured electric polarization shown in Fig. 5.3b is of the same order as that for out-of-plane fields. The electric polarization shows a periodic dependence on the azimuthal angle,  $\varphi$ , with the period of  $60^\circ$  apparently resulting from a sixth-order MEE. The lowest-order expression for the electric polarization induced by an in-plane magnetic field is, indeed, of sixth order in  $H$ :

$$P_z^{(6)} = a_6(T)H_xH_y(H_x^2 - 3H_y^2)(3H_x^2 - H_y^2) \propto \sin 6\varphi. \quad (5.3)$$

The sixth-order magnetoelectric response has not been discussed so far in the literature. The right-hand side of Eq. (5.3), found using symmetry arguments [55; 77; 78], is

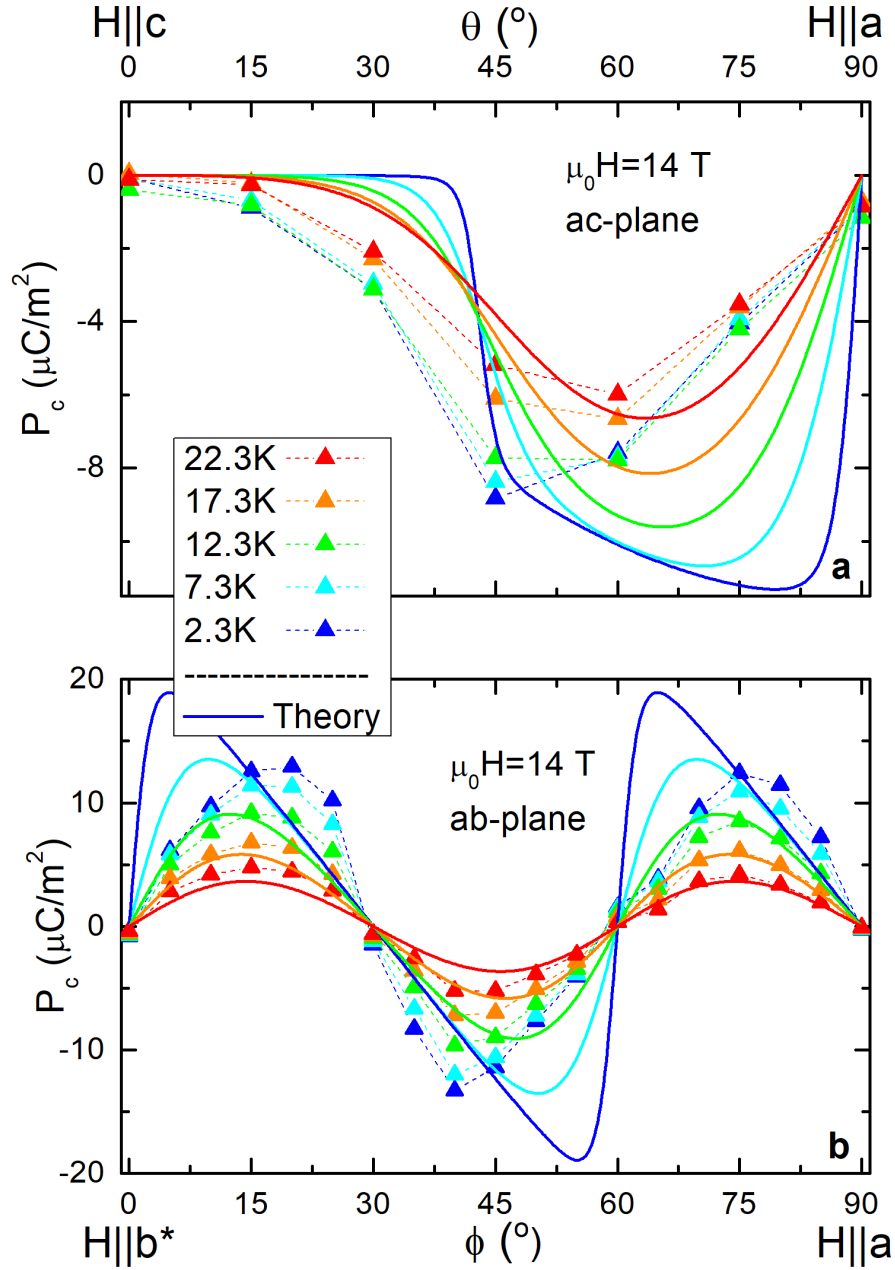


Figure 5.3: Angular dependence of the static electric polarization along the  $c$ -axis. **a.** Dependence of  $P_c$  on the polar angle  $\theta$  between the applied magnetic field,  $\mathbf{H}$ , and the  $c$ -axis, for  $\mathbf{H}$  rotated in the  $ac$ -plane at several temperatures. **b.** Dependence of  $P_c$  on the azimuthal angle  $\phi$  for  $\mathbf{H}$  rotated in the  $ab$ -plane. The modulation with the  $60^\circ$  period is indicative of a high-order MEE (see Eq. (5.3)). Experimental data are shown with symbols, and solid lines are calculated within the model described in Chapter 5.1.

the lowest-order polynomial of  $H_x$  and  $H_y$  that transforms as  $P_z$ . The saw-tooth shape of the angular dependence of the polarization at low temperatures (Fig. 5.3b) indicates contributions of MEEs of yet higher orders.

Eqs. (5.2) and (5.3) imply that the electric polarization is proportional to the 4<sup>th</sup> or 6<sup>th</sup> power of the applied magnetic field, depending on the orientation of  $\mathbf{H}$ . Instead, at low temperatures we observe a nearly linear dependence of  $P_z$  for any field direction (see Fig. 5.4). Importantly, phenomenological Eqs. (5.2) and (5.3) only hold for weak magnetic fields,  $|\mu_{\text{Ho}}H| \ll \max(\Delta, k_{\text{B}}T)$ ,  $\mu_{\text{Ho}}$  being the saturated magnetic moment of a  $\text{Ho}^{3+}$ -ion. At low temperatures, their validity is limited to fields  $\lesssim 1$  T (see Fig. 5.4b). The saturation of the Ho magnetic moment at higher magnetic fields gives rise to higher-order harmonics in the observed angular dependence of the electric polarization.

Counterintuitively, the onset of a more complex  $\theta$ - and  $\varphi$ -dependence correlates with the crossover to a *linear* dependence of  $P_z$  on the magnitude of the magnetic field (Fig. 5.4). The calculation of the final expressions are given in [61] and will be outlined in the following.

In the absence of inversion symmetry, the rare-earth ions interact with the electric field,  $\mathbf{E}$ , through an effective dipole moment operator,  $\hat{\mathbf{d}}$ , which in the subspace of the ground-state multiplet can be expressed in terms of the quadrupole and higher-order magnetic multipole moments of the ions [6]. The spectrum of the low-energy states depends then on both electric and magnetic fields, which gives rise to a magnetoelectric response of the rare-earth ions. The description of the MEE in Ho-langasite can be simplified by projecting the Hamiltonian describing the magnetoelectric behavior of the ground-state multiplet on the subspace of the two states forming the lowest-energy non-Kramers doublet [61].

The energies  $+\epsilon_i$  and  $-\epsilon_i$  ( $i = 1, 2, 3$ ) of the two states forming the doublet are in zero electric field given as

$$\epsilon_i = \sqrt{(\boldsymbol{\mu} \cdot \mathbf{H}_i)^2 + (\Delta/2)^2}, \quad (5.4)$$

where  $\boldsymbol{\mu}$  is the magnetic moment of the  $\text{Ho}^{3+}$ -ion and  $(\boldsymbol{\mu} \cdot \mathbf{H}_i) = \mu_x H_{X_i} + \mu_y H_{Y_i}$ . With this we can calculate the free energy of the doublet

$$f = -\frac{1}{3}n_{\text{Ho}}k_{\text{B}}T \sum_{i=1}^3 \ln \left( 2 \cosh \frac{\epsilon_i}{k_{\text{B}}T} \right), \quad (5.5)$$

which leads to a magnetically-induced electric polarization of

$$\langle P_c \rangle = -\frac{n_{\text{Ho}}}{3} \sum_{i=1}^3 \left( \frac{\partial f_i}{\partial E_c} \right)_{E_c=0} = g_{YZ} \frac{n_{\text{Ho}}}{3} \sum_{i=1}^3 H_{Z_i} M_i, \quad (5.6)$$

where  $n_{\text{Ho}}$  is the density of Ho-ions,  $g_{YZ}$  is a real number and  $M_i$  is related to the average

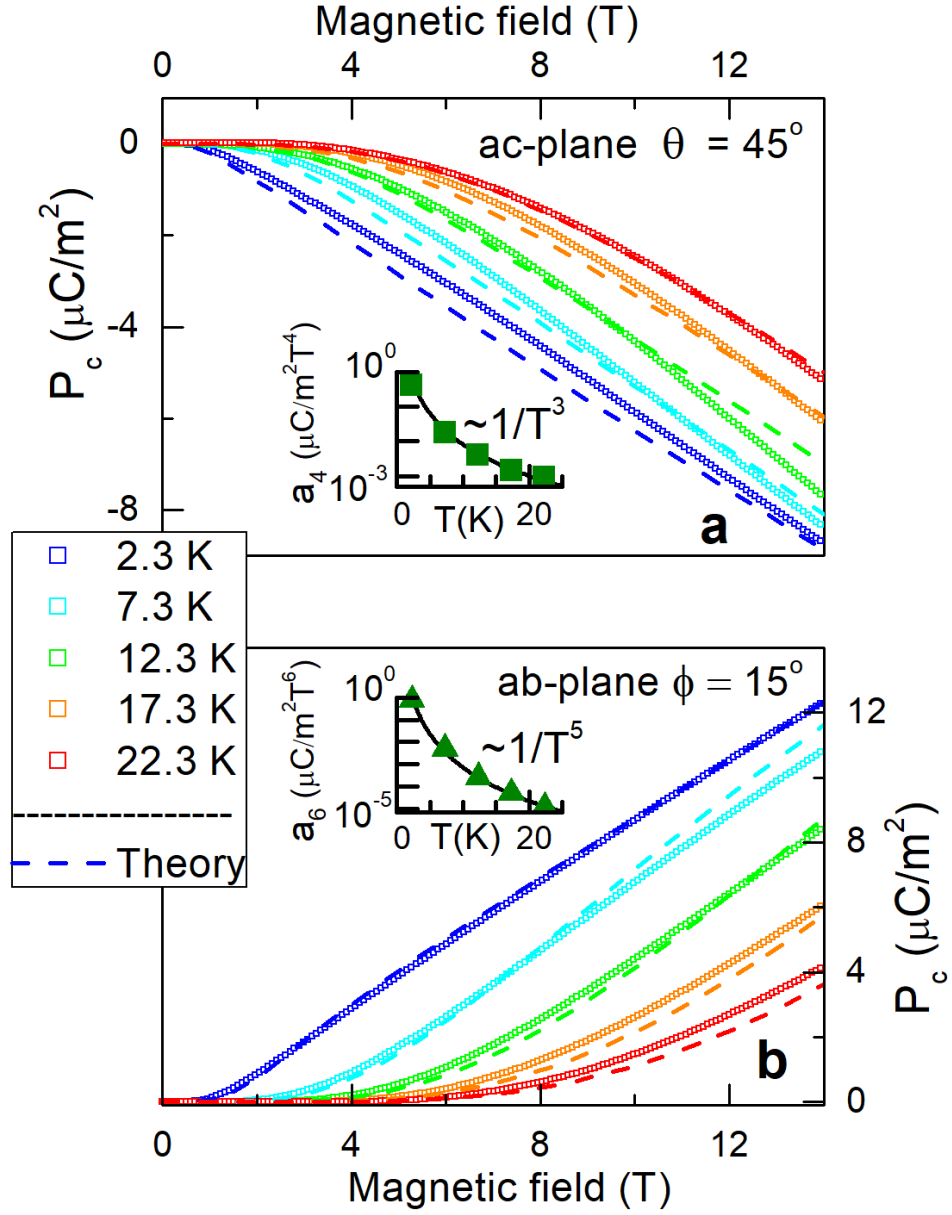


Figure 5.4: Linear magnetoelectric effect in Ho-langasite. **a.** Electric polarization for magnetic fields in the  $ac$ -plane with  $\theta = 45^\circ$  (see also Fig.5.3a). Symbols are experimental data, dashed lines are results of theoretical calculations, as described in Chapter 5.1. The inset shows temperature dependence of the strength of the 4<sup>th</sup>-order magnetoelectric response,  $a_4$  in Eq. (5.3), obtained from the low-field slopes. Symbols are experimental data; the line is the  $T^{-3}$  fit. **b.** Magnetic field dependence of the electric polarization,  $P_c$ , for applied magnetic fields rotated in the  $ab$ -plane through  $15^\circ$  from the  $b^*$ -axis (see also Fig. 5.3b). The inset shows temperature dependence of the strength of the 6<sup>th</sup>-order magnetoelectric response,  $a_6$  in Eq. (5.3), obtained from the low-field slopes. Symbols are experimental data; the line is the  $T^{-5}$  fit.

magnetic moment of the  $i$ -th Ho-ion by  $\langle \boldsymbol{\mu}_i \rangle = (\mu_X, \mu_Y, 0)M_i$  and equals to

$$M_i = \frac{\tanh \beta \epsilon_i}{\epsilon_i} (\boldsymbol{\mu} \cdot \mathbf{H}_i), \quad (5.7)$$

where  $\beta = 1/k_B T$ .

Summing Eq. (5.7) over the three Ho-sites gives an average magnetic moment at zero applied electric field of

$$\mathbf{M} = \frac{n_{\text{Ho}} \mu_0^2}{3} \sum_{i=1}^3 \boldsymbol{\mu}_i (\boldsymbol{\mu}_i \cdot \mathbf{H}) \frac{\tanh(\beta \epsilon_i)}{\epsilon_i}. \quad (5.8)$$

The largest discrepancy between theory and experiment is found in the angular dependence of the electric polarization shown in Fig. 5.3. The main reason for this deviation is the intrinsic disorder in the langasite crystal structure (Fig. 5.1). The four positions in the local surrounding of rare-earth ions are randomly occupied by two Si and two Ga ions [64; 69] resulting in 6 inequivalent Ho-ions in each sublattice and the concomitant lattice distortions affect the magnetic anisotropy and magnetoelectric interactions of the ions. This will be considered in the extension of this model, as discussed in Chapter 5.2. Importantly, our simple model<sup>2</sup> based on average symmetry of rare-earth ions captures the basic physics of the magnetoelectric response of Ho-langasite.

In the limit of strong fields and low temperatures,  $|\boldsymbol{\mu} \cdot \mathbf{H}_i| \gg \Delta, k_B T$ , when the magnetic moment saturates, the electric polarization,

$$P_c = \frac{1}{3} n_{\text{Ho}} g_{YZ} \sum_{i=1}^3 H_{Z_i} \text{sign}(\boldsymbol{\mu} \cdot \mathbf{H}_i), \quad (5.9)$$

shows a complex saw-tooth dependence on the direction of the magnetic field in the  $ab$ -plane (due to the sign-functions) and, at the same time, a simple linear dependence on the strength of the magnetic field, in agreement with our experimental observations.

In the opposite limit of weak fields and high temperatures,  $k_B T \gg |\mu_0 H|, \Delta$ ,

$$P_c \approx \frac{n_{\text{Ho}} g_{YZ} \mu_0^3 H^4}{4(k_B T)^3} \sin \gamma \cos^2 \gamma \cos \theta \sin^3 \theta \cos 3\varphi, \quad (5.10)$$

where  $H$  is the magnitude of the magnetic field and  $\gamma = \arccos(\mu_Y/\mu_0)$ , which agrees with Eq. (5.2) obtained by symmetry and gives  $a_4(T) \propto T^{-3}$ . At zero temperature,  $(k_B T)^3$  in Eq. (5.10) is replaced by  $\Delta^3/12$ .

For magnetic field applied in the  $ab$ -plane, the electric polarization at high tempera-

<sup>2</sup>In the following the model developed in Chapter 5.1 is referred to as the 'simple model'.

tures,

$$P_c \approx \frac{n_{\text{Ho}} g_{YZ} \mu_0^5 H^6}{240 (k_B T)^5} \cos^5 \gamma \sin^6 \theta \sin(6\varphi), \quad (5.11)$$

is proportional to  $H^6$  and oscillates six times as  $\varphi$  varies by  $2\pi$ , in agreement with Eq. (5.3) ( $a_6 \propto T^{-5}$ ). At zero temperature,  $(k_B T)^5 \rightarrow \Delta^5/90$ .

The coefficients  $a_4$  and  $a_6$  in Eqs. (5.2, 5.3) can be estimated from the low-field slopes of experimental data shown in Fig. 5.4. As demonstrated in the insets to Fig. 5.4, they indeed follow the expected  $a_4 \propto T^{-3}$  and  $a_6 \propto T^{-5}$  behavior.

For a more detailed discussion of the microscopic model, see [61] and Refs. [79; 80; 81; 82]. The resulting magnetic field-dependence of the electric polarization (dashed lines in Figs. 5.3 and 5.4) is in reasonable agreement with experimental data.

## 5.2 Extended Model of Magnetic Structure in Ho-LGS

Even though the main features of the observed magnetoelectric effect can be reproduced by the first model presented above, many discrepancies remain to be explained, calling for an extension of the model. In particular the magnetization curve (Fig. 5.6) indicates that the magnetic structure of this compound is more complex than accounted for in the first model. To resolve the actual magnetic structure measurements of the magnetization as a function of the magnetic field direction in a SQUID magnetometer were performed and combined with further measurements in a torque magnetometer. As presented in Chapter 5.2.2 and 5.2.3, these measurements show clearly the need for extending the first approximation of the model (Chapter 5.1).

### 5.2.1 Breaking of Local $C_2$ Symmetry

As a starting point for extending the simple model (Chapter 5.1), it is useful to revisit the assumptions we made previously. The possible orientation of the Ising-type magnetic moment of the Ho-ion is limited by the  $C_2$ -symmetry to be either in the perpendicular plane or parallel to the  $a$ -axis of the crystal. Considering that the crystal  $C_2$ -symmetry relies on averaging the random distribution of the Ga- and Si-ions, which occupy the 2d-position (see Fig. 5.1), a local breaking of this symmetry becomes possible in cases of an uneven distribution. For estimating the possible influence of the 2d-position on the magnetic moment of the Ho-ions the nearest and next-nearest 2d-sites should be taken into account, since they have a similar distance to the rare-earth site ( $d_1 = 3.42$  and  $d_2 = 3.66$ , respectively). These four positions can be occupied by 16 different combinations of Ga- and Si-ions, of which only four possibilities preserve the  $C_2$ -symmetry, as visualized in Fig. 5.5.

Therefore it seems reasonable to consider additional easy axes which do not follow the crystal's  $C_2$ -symmetry. Nevertheless it is important to note that those additional easy axes may break the symmetry locally, but an averaging over the whole crystal should

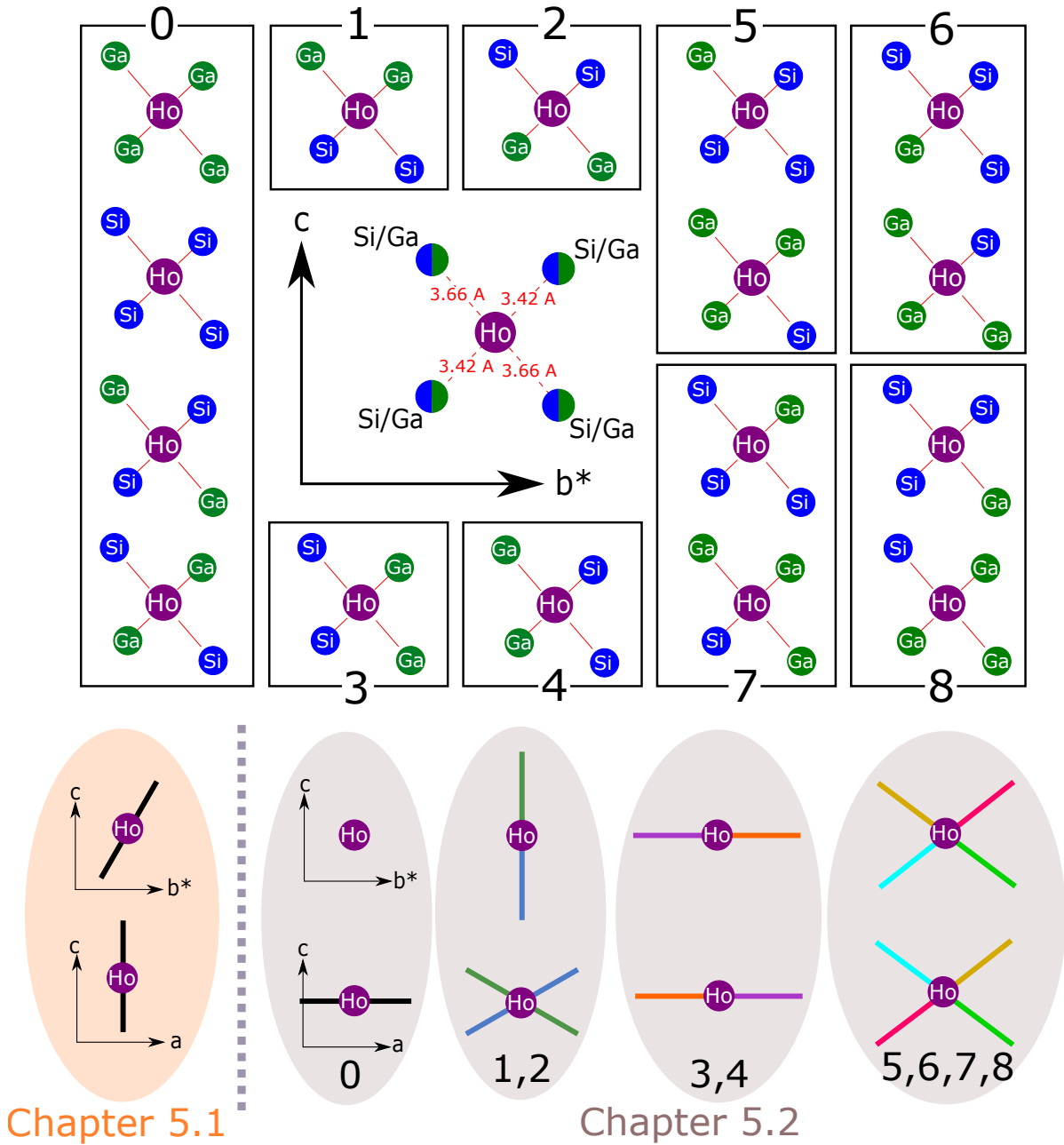


Figure 5.5: The 16 different distributions of Ga/Si-ions in the close vicinity of the magnetic Ho-ion (top), which lead to 9 different possible directions of the magnetic moment (bottom right) are shown schematically as a projection onto the  $b^*c$ -plane (and  $ac$ -plane). Note that the relative length of the projected distance is exaggerated in the 16 distributions to clarify the symmetry. The actual ratio is shown in the general scheme in the center. In the model presented in the text, both distances were assumed to be of equal length. The model of Chapter 5.1 is shown in the bottom left.

still restore the  $C_2$ -symmetry. Therefore for each easy axis, which does not satisfy the symmetry, a second easy axis has to be assumed in such a way that the twofold rotation around the  $a$ -axis projects those two axes onto each other. In the following section the measurements of the magnetic torque of Ho-LGS are presented and analyzed to identify which directions of the Ising-type magnetic moments are present in the investigated sample.

### 5.2.2 Magnetization

The magnetization of a single Ho-ion becomes in this extension of the model slightly more complex as compared to Eq. (5.7), since a summation over the different easy axes  $\mathbf{e}_i$  is needed, resulting in

$$\boldsymbol{\mu}_{\text{Ho}}(\mathbf{H}) = \sum_{\mathbf{e}_i} w_i \cdot \boldsymbol{\mu}_i (\boldsymbol{\mu}_i \cdot \mathbf{H}) \frac{\tanh \frac{\Delta}{k_B T}}{\Delta}, \quad (5.12)$$

where the moments of the different easy axes are weighted with  $\sum_i w_i = 1$  and  $\boldsymbol{\mu}_i = m_{\text{tot}} \mathbf{e}_i$ , with the length of the magnetic moment  $m_{\text{tot}}$ . So far only the magnetization emerging from the lowest-energy doublet,  $M_{2\text{lvl}}$  was considered. The higher energy levels can be included in this expression via the temperature-independent van-Vleck paramagnetism [83]. This additional values to the magnetization can be extracted from the high-field region of the magnetization curve. Here the change of  $\mathbf{M}_{2\text{lvl}}$  becomes negligible and the van-Vleck slopes dominate the change of magnetization. Therefore we extended the set of measurements with new measurements performed with a vibrating sample magnetometer in a PPMS, which provides magnetic field strengths of up to 14 T (Fig. 5.6). The investigated sample has a nearly cubical shape and originates from the same batch as the other cuts of  $\text{Ho}_x\text{La}_{3-x}\text{Ga}_5\text{SiO}_{14}$ , which were measured in this work. The slope of the linear fits of the magnetization above 13 T were used to get the three different van-Vleck parameters  $V_a \approx 55.9 \frac{\mu_B/\text{Ho}}{\text{kT}}$ ,  $V_{b^*} \approx 60.2 \frac{\mu_B/\text{Ho}}{\text{kT}}$  and  $V_c \approx 29.2 \frac{\mu_B/\text{Ho}}{\text{kT}}$ , which can be used to calculate the van-Vleck magnetization

$$\mathbf{M}_{\text{vV}} = \begin{bmatrix} V_a & 0 & 0 \\ 0 & V_b & 0 \\ 0 & 0 & V_c \end{bmatrix} \cdot \mathbf{H}. \quad (5.13)$$

The magnetization of the two level system and the van-Vleck magnetization sum up to the total magnetization

$$\mathbf{M}_{\text{tot}} = \mathbf{M}_{2\text{lvl}} + \mathbf{M}_{\text{vV}}. \quad (5.14)$$

Due to the presence of the threefold rotation axis, which is along the crystal's  $c$ -axis, the van-Vleck parameter should be constant in the  $ab$ -plane. Nevertheless the parameters  $V_a$  and  $V_{b^*}$  were not observed to be exactly the same, which might be due to a small misalignment of the sample in the measurement. Even though a significant improvement

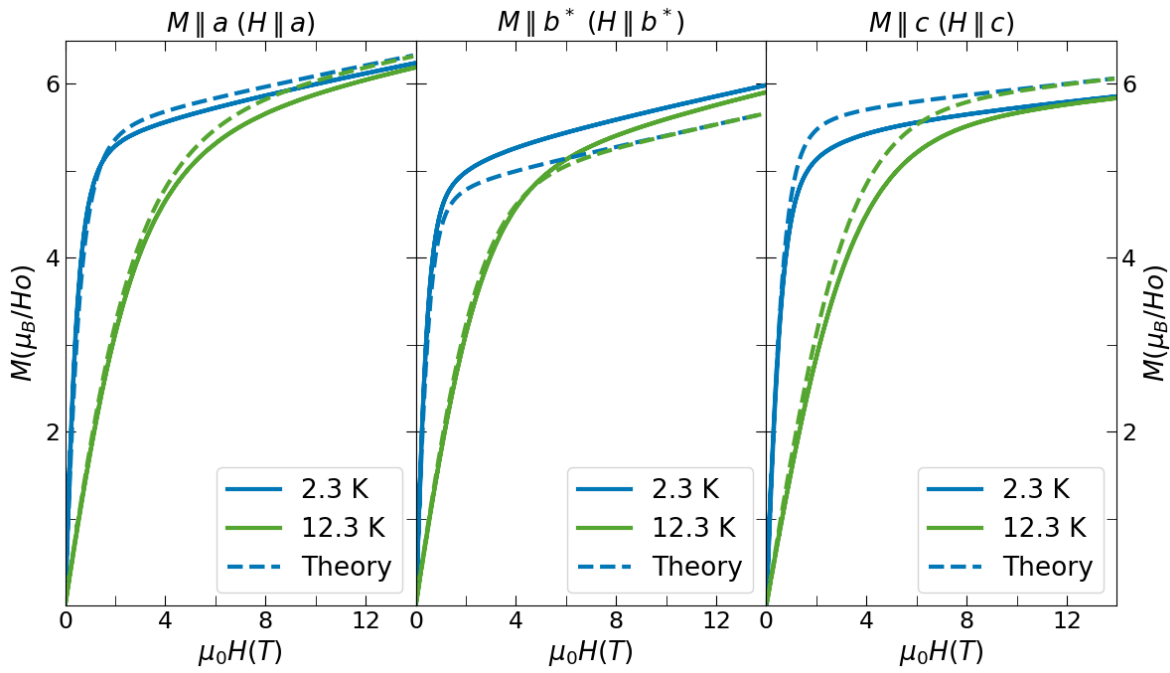


Figure 5.6: The field scans of the magnetization along the main crystallographic axes, measured at 2.3 K (blue) and 12.3 K (green). The theoretical curve (dashed) is calculated according to the extended model, as outlined in the text.

can be achieved by the new model, an error in the range of 5% remains. In the other hand we observed that the magnetization curve was not reproduced accurately in the various sets of measurements, which were measured with different samples. Therefore it is not unlikely that this error can be attributed to experimental artifacts.

With the equations given above, it is not only possible to calculate the magnetization as a function of the applied magnetic field, but also the angular dependence of the magnetization for a fixed field strength. The corresponding measurements, which were taken in a SQUID magnetometer, are presented in Fig. 5.7. The thin red line shows the theoretical prediction based on the simple model and thus confirms again the need for a more accurate model, as developed in this chapter and shown in the Fig. 5.7 (cyan).

### 5.2.3 Magnetic Torque

In Fig. 5.8 we compare the experimental result of the magnetic torque for the three main crystallographic axes with the prediction of the simple model (red) and the fitting of the improved model, which will be developed in the following sections. The measurement of  $\tau_c$  reveals the same sixfold oscillation that was observed in the measurement of the electric polarization along the crystal's  $c$ -direction while rotating the magnetic field in the  $ab$ -plane (Figs. 5.3 and 5.14). In both cases the simple model fails to reproduce the position of the sharp jumps, which occur whenever the magnetic field is parallel to the local  $\hat{y}$ -direction of one of the three Ho-sites. The definition of the magnetic torque is given in Eq. (2.3) as  $\boldsymbol{\tau} = \boldsymbol{\mu} \times \mathbf{H}$ . Hence, the step-like jumps can be interpreted as a switching of one of the three Ising-type local magnetic moments, which occurs, whenever the magnetic field sweeps across the projection of an easy axis onto the  $ab$ -plane, leading to a change of sign of the corresponding local magnetic moment. This is an indication that the projection of all easy axes onto the  $ab$ -plane are parallel to the local  $\hat{x}$ -axis of the Ho-ions, i.e. are in the local  $\hat{x}\hat{z}$ -planes. This is a distinct contradiction to the simple model, where the magnetic moments were assumed to lie in the local  $\hat{y}\hat{z}$ -planes. The measurement of the magnetic torque in the  $ac$ -plane,  $\tau_{b^*}$ , confirms the assumptions that at least two easy axes are present for each Ho-ion, since the change of sign from positive to negative torque is splitted into two separate jumps (Fig. 5.8).

### 5.2.4 Fitting the Magnetic Structure

As discussed previously, each Holmium-ion can be surrounded by 16 different combinations of Ga- and Si-ions on the shared atomic site, leading to the assumption that the  $C_2$ -symmetry might be locally broken. Nevertheless it has to be noted that 4 of the 16 different distributions do satisfy the symmetry, suggesting that an undistorted easy axis is present in the sample, which is then complemented by up to eight distorted easy axes (Fig. 5.5). Contrary to the assumption of the simple model, we assume as a conclusion of the previously presented analysis of the torque measurement that the undistorted easy axis is along the local  $\hat{x}$ -axis. This is allowed, since the main argument for choosing the

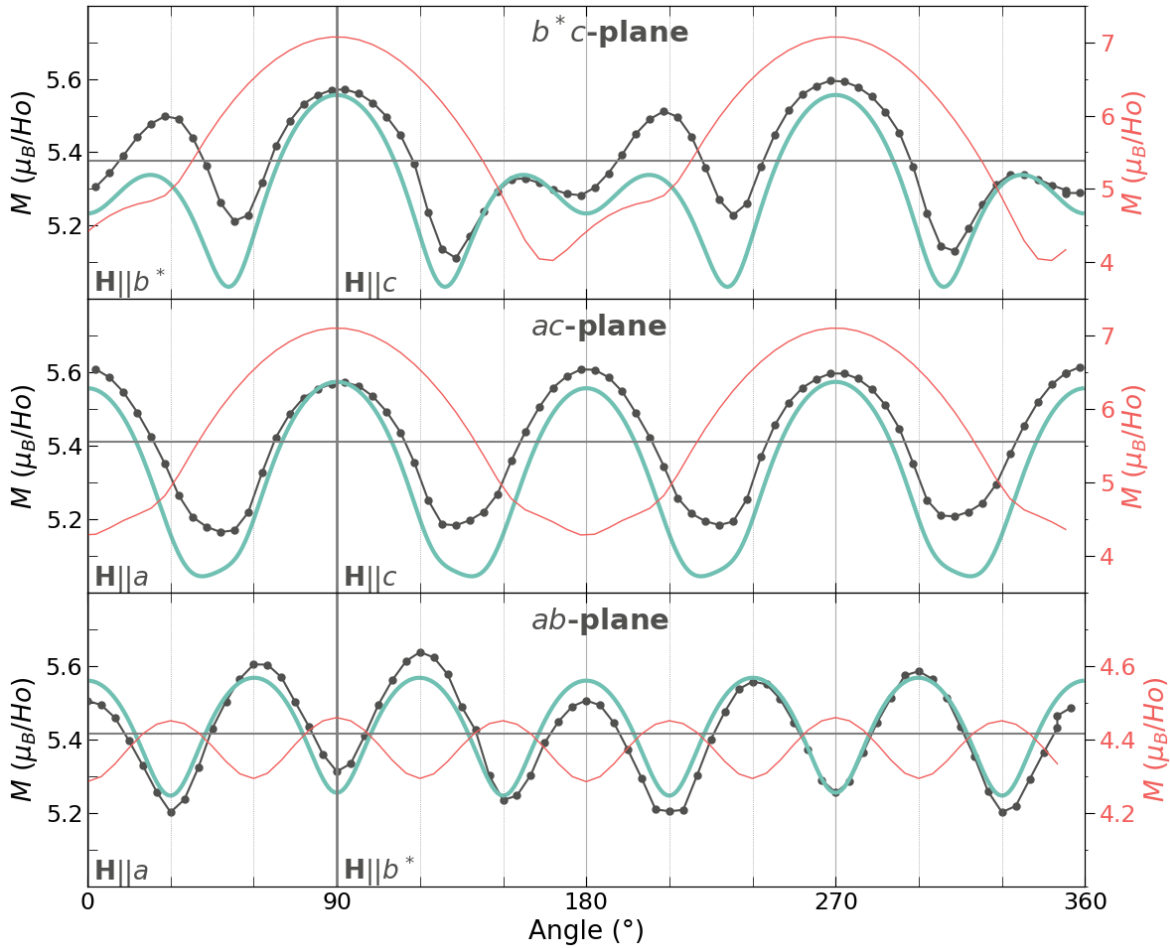


Figure 5.7: The experimental result (black) of the magnetization along the direction of the applied magnetic field is compared to the theoretical predictions of the simplified (red, Chapter 5.1) and extended model (cyan, Chapter 5.2). Note that the scale had to be adjusted for the simple model (right) as an attempt to compare the main features of both models. The measurements were taken at 5 K and at a magnetic field of 5 T, which was rotated in the samples  $b^*c$ - (top),  $ac$ - (middle), and  $ab$ -plane (bottom).

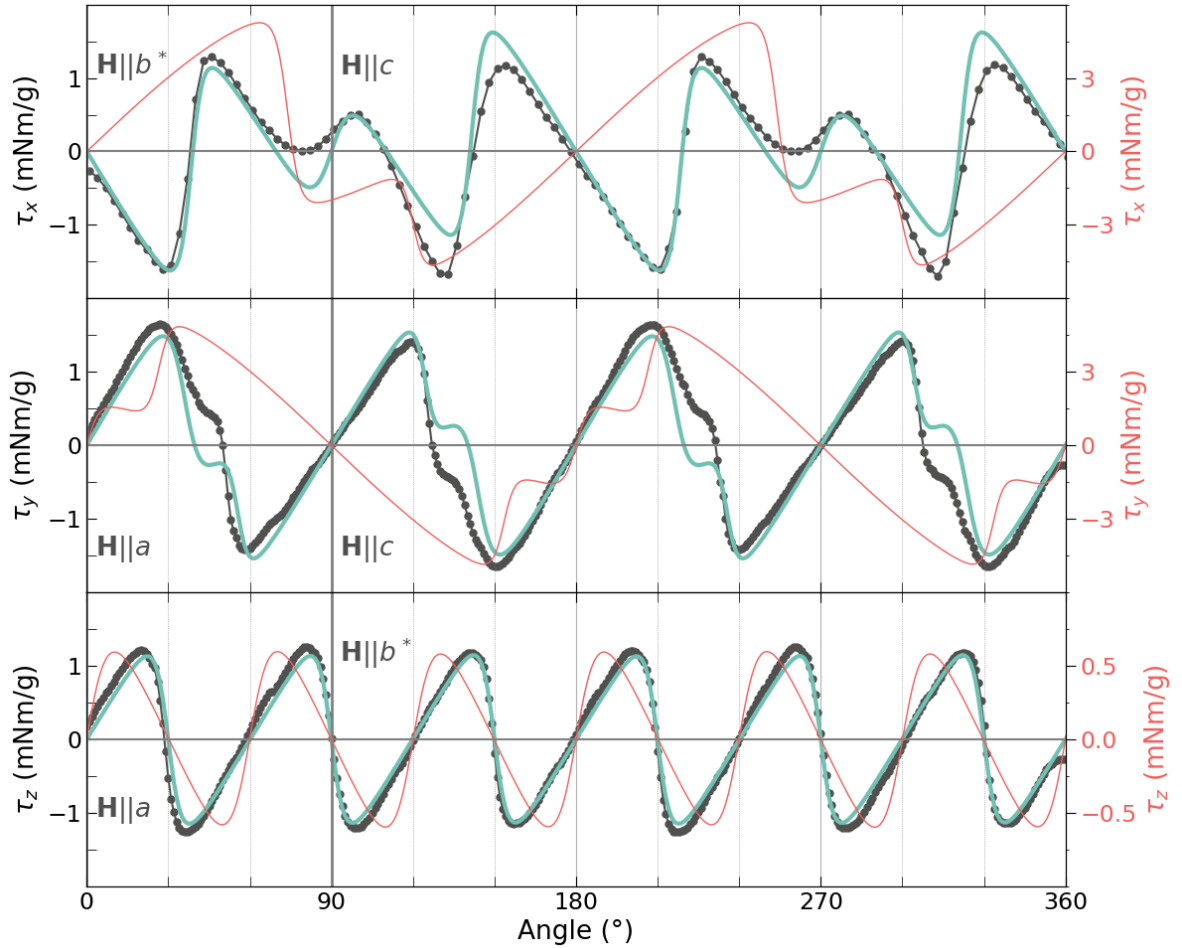


Figure 5.8: The experimental result (black) of the magnetic torque is compared to the theoretical predictions of the simplified (red, section) and extended model (cyan, section). Note that the scale had to be adjusted for the simple model (right) as an attempt to compare the main features of both models. The measurements were taken at 2.3 K and at a magnetic field of 6 T, which was rotated in the samples  $b^*c$ - (top),  $ac$ - (middle), and  $ab$ -plane (bottom).

easy axis to be in the  $\hat{y}\hat{z}$ -planes, i.e. the non-zero magnetization in  $c$ -direction, is not valid anymore, due to the assumption of additional distorted easy axes<sup>3</sup>.

Having this in mind, we can identify the nine possible easy axes  $\mathbf{e}_i$  as visualized in Fig. 5.5 and describe them by only four angles  $\theta_1$ ,  $\phi_2$ ,  $\theta_3$  and  $\phi_3$  as given in Table 5.1. Here we neglected the small difference in distance between the Ho-ion and the nearest and next-nearest Ga/Si-sites, respectively, and assume a mirror symmetry around the  $c$ -axis, which translates  $\mathbf{e}_5$  into  $\mathbf{e}_7$  and  $\mathbf{e}_6$  into  $\mathbf{e}_8$ . Hence, we are able to describe those four easy axes by only two angles  $\theta_3$  and  $\phi_3$ .

In this table we assigned to each easy axis a weight  $w_i$ , representing the relative abundance of the  $i$ -th easy axis, by assuming a random distribution of the Ga- and Si-ions. Nevertheless we used the weights as additional free parameters in the fitting procedure, to account for possible deviations of the random Ga/Si-distribution in the vicinity of a Ho-ion. However, the weights need to satisfy the conditions  $w_1 = w_2$ ,  $w_3 = w_4$  and  $w_5 = w_6 = w_7 = w_8$  due to symmetry arguments, while also  $\sum_i w_i = 1$  has to be fulfilled. Therefore only three additional parameters are needed to cover all possible relative abundances of the  $\mathbf{e}_i$ .

$i =$	0	1, 2	3, 4	5, 6, 7, 8
$\mathbf{e}_i$	$\begin{pmatrix} 1 \\ 0 \\ 0 \end{pmatrix}$	$\begin{pmatrix} \cos(\theta_1) \\ 0 \\ \pm \sin(\theta_1) \end{pmatrix}$	$\begin{pmatrix} \cos(\phi_2) \\ \pm \sin(\phi_2) \\ 0 \end{pmatrix}$	$\begin{pmatrix} \cos(\phi_3) \sin(\theta_3) \\ \pm \sin(\phi_3) \sin(\theta_3) \\ \pm \cos(\theta_3) \end{pmatrix}$
$w_i$	1/4	1/16	1/16	1/8

Table 5.1: The directions and weights of the easy axes  $\mathbf{e}_i$  that can be assumed for a random distribution of Ga- and Si-ions, as visualized in Fig. 5.5.

First results of this new model revealed the need for an additional scaling parameter,  $\lambda$ , to scale the magnetic torque and the change of  $M_H$ , i.e. the magnetization projected onto the direction of the applied magnetic field, via

$$\tau(\mathbf{e}_i, w_i, \lambda) |_{\mathbf{H}} = \lambda (\mathbf{M}_{\text{tot}}(\mathbf{e}_i, w_i) |_{\mathbf{H}} \times \mathbf{H}) \text{ and} \quad (5.15)$$

$$M_{\mathbf{H},j}(\mathbf{e}_i, w_i, \lambda) = \overline{M}_{\mathbf{H},j} + \lambda (M_{\mathbf{H}}(\mathbf{e}_i, w_i) - \overline{M}_{\mathbf{H},j}) , \quad (5.16)$$

respectively. Here  $\overline{M}_{\mathbf{H},j}$  is the experimentally determined average magnetization along the magnetic field direction for each of the three sets of measurements (gray horizontal line in Fig. 5.7) and  $j = a, b^*, c$  denotes the rotation of the magnetic field through the samples  $b^*c$ -,  $ac$ - and  $ab$ -plane, respectively. Without the parameter  $\lambda$  no quantitative agreement between experimental and theoretical curves can be achieved for Figs. 5.7 and 5.8. Instead the model overestimates the magnetic anisotropy without this parameter.

<sup>3</sup>The fitting procedure was repeated with an easy axis in the  $\hat{y}\hat{z}$ -planes as a starting point. However, the experiments could not be described very well. Therefore only the model with an easy axis along the local  $\hat{x}$ -axis as a starting point is presented in this chapter.

In total this leads us to a set of eight parameters (4 angles, 3 weights, 1 scaling factor) to fit six sets of measurements (Figs. 5.7 and 5.8) simultaneously. The straight-forward fitting procedure would consist of calculating the residual for every possible combination of values for the eight parameters, down to a predefined threshold. Unsurprisingly, this brute-force search would take too much computational cost to be feasible and was therefore replaced by a more delicate approach. First of all it is essential to define how the residuals are calculated for a given set of parameters  $\mathbf{p}$ , since the weighting can influence the outcome. For each of the six sets of measurements, the residual is calculated in the same way (here given for  $\tau_x$ ):

$$\rho_{\tau,x} = \frac{n_{\tau,x}}{\sum_i \tau_{\text{exp},x_i}} \left( \frac{\sum_{x_i} (\tau_{\text{exp},x_i} - \tau_{x_i}(\mathbf{p}))^2}{n_{\tau,x}} \right)^{1/2}, \quad (5.17)$$

where the sum over the  $x_i$  denotes the summation over all points of the given measurement and the subscript 'exp' is used to distinguish the experimental values from the theoretically calculated. The summation of all  $n = 6$  residuals gives the total residual

$$\rho = \frac{\sum_j \rho_j}{n}, \quad (5.18)$$

which will be minimized by a variation of the Hooke's algorithm (Fig. 5.9), as explained in the following paragraph.

In this approach a certain number of points are randomly generated in the eight dimensional parameter space, which is constrained by the predefined limits. The angles can be set due to symmetry reasons to  $< 90^\circ$  and the weights are  $w_i < 1$ . In each iteration of the following algorithm every point moves in the parameter space in the way, which is visualized in the schematic Fig. 5.9. In the first phase of every iteration the optimal direction is determined, by varying every coordinate, i.e. parameter, one after another by a predefined step-size, first in the positive and, if this does not reduce the residual, in the negative direction. If the residual is decreased by the step, the new coordinate is saved, before this procedure is repeated for the next coordinate. After all eight coordinates are varied, the algorithm moves either on to phase 2a or, if no further reduction was reached, reduces the step size (phase 2b). The phase 2a was implemented to reduce the computational cost considerably. Instead of finding a new optimal direction (phase 1), the point moves in the previously determined direction as long as no further reduction of the residual can be achieved. Only when this is the case a new iteration is started with phase 1. This procedure is repeated until a predefined cut-off step-size is reached in phase 2b.

This explanation is still simplified and it is important to pay attention to some possible disadvantages of this approach. First of all the term 'best direction' is not accurate, since one parameter is varied after another and saved as soon as the value of the residual is reduced. Hence, not all directions are actually tested. A quite common disadvantage of

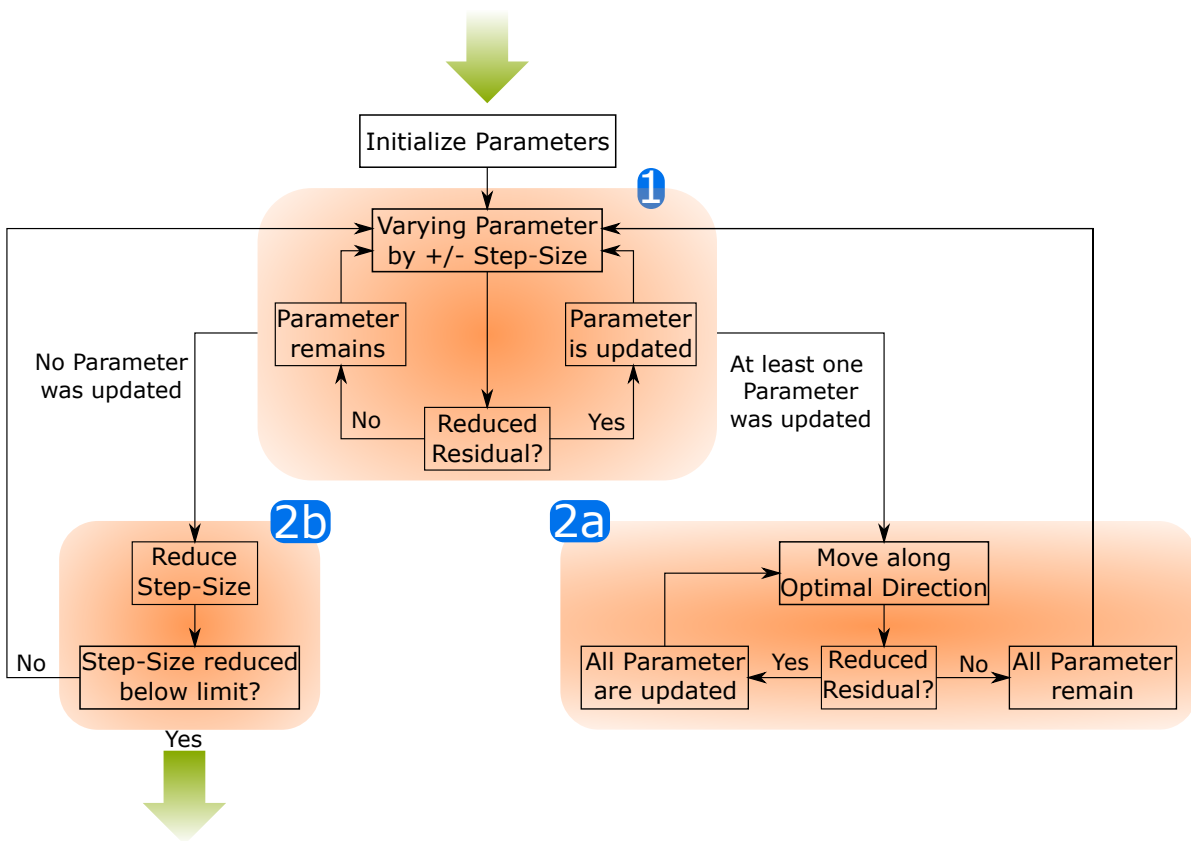


Figure 5.9: A schematic of the fitting algorithm is shown. The three different phases 1, 2a and 2b are explained in the text in more detail.

several fitting algorithms is the risk of ending up in local minima. However, this issue can be overcome by initializing not just one, but several random points in the parameter space. In this way it is easy to estimate the risk of being stuck in a local minima. In the presented case all points ended up with a very similar set of parameters, which confirms that we did find indeed the global minimum. The fitting leads to a rather interesting outcome, which is shown in Table 5.2.

#free parameters	$\theta_1(^{\circ})$	$\phi_2(^{\circ})$	$\theta_3(^{\circ})$	$\phi_3(^{\circ})$	$w_0$	$w_{1,2}$	$w_{3,4}$	$w_{5,6,7,8}$	$\lambda$
8	32.12	11.31	38.50	2.51	0.00	0.31	0.00	0.08	0.49
2	34.30	<b>x</b>	<b>x</b>	<b>x</b>	<b>0</b>	<b>0.5</b>	<b>0</b>	<b>0</b>	0.47

Table 5.2: The parameters, which minimize the residuals for the magnetic torque and the angular dependence of the magnetization, as determined by the fitting algorithm, which is discussed in the text. In a second fitting procedure, only the two easy axes  $\mathbf{e}_{1,2}$  were taken into account, by fixing the weights of the other seven easy axes to zero (bold). This means that the number of free parameters (blue) were reduced to only two. The definition of the easy axes are shown in Table 5.1. A visualization of both sets of parameters are given in Fig. 5.10.

The values for  $w_0$  and  $w_{3,4}$  are fitted to be close to zero, giving rise to the conclusion that neither the 'undistorted' direction ( $\mathbf{e}_0$ ) nor the easy axes within the  $ab$ -plane ( $\mathbf{e}_{3,4}$ ) are present in the compound. Furthermore the polar angle describing  $\mathbf{e}_{5,6,7,8}$  is very close to  $\theta_3 \approx 0^{\circ}$ , which also describes  $\mathbf{e}_{1,2}$ .  $\phi_2$  and  $\phi_3$  have similar values. Therefore it seems likely that the magnetic structure can be explained by only the two easy axes  $\mathbf{e}_{1,2}$  alone. To confirm this hypothesis a second fitting was performed, where the number of parameters were reduced, as shown in Table 5.2. And indeed, the agreement of theoretical data and experiment was substantially of the same quality. Both sets of parameters of this refined model are visualized in Fig. 5.10. The model does not only reproduce the measurements of the magnetic torque (Fig. 5.8) and the magnetization (Fig. 5.7) in a reasonable matter, but it also improves the fits of the magnetoelectric effect (Fig. 5.13). Furthermore, this hypothesis goes very well with the observation of only two modes of the paramagnetic resonance, as discussed in the following section.

## 5.2.5 Paramagnetic Resonance

To get an accurate understanding of the magnetic structure of the investigated compound, it is important to identify the crystal field splitting of the lowest lying doublet. In Chapter 5.1 we assumed a value for this splitting of  $\Delta = 3.1 K$ , which was taken from measurements of the paramagnetic resonance in a quasi-optical sub-THz interferometer (Chapter 2.3). Here we present those measurements and compare them to the theoretical

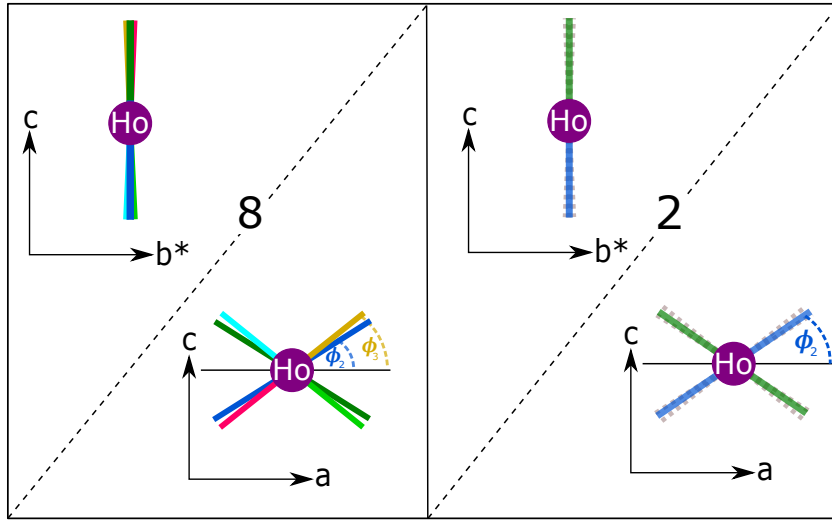


Figure 5.10: Visualization of the easy axes as given in Table 5.2 for eight (left) and two (right) parameters. Only the axes with non-zero weights are drawn. The dashed lines on the right panel indicate the position of the easy axes with eight parameters (left panel). The projections of the easy axes onto the  $ac$ - and  $b^*c$ -plane were chosen in accordance to Fig. 5.5.

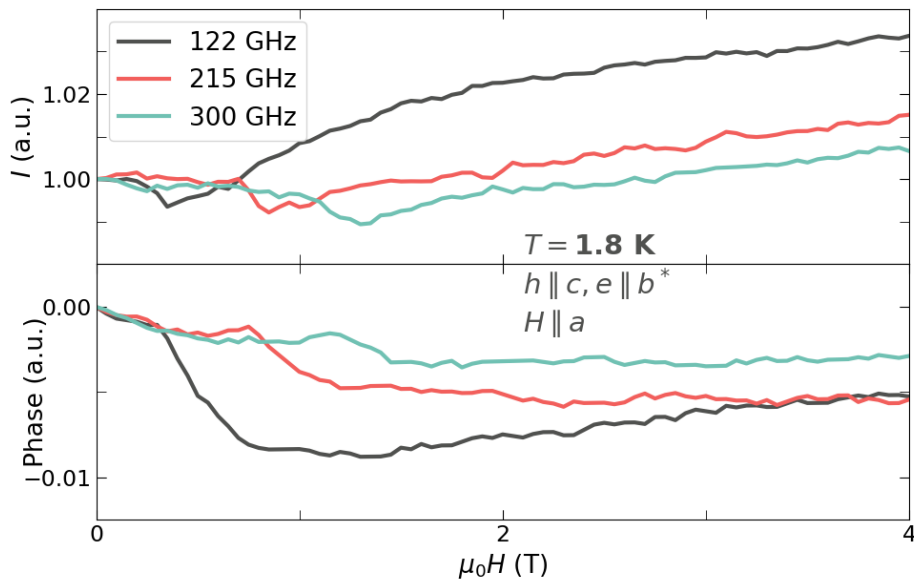


Figure 5.11: Examples of a paramagnetic resonance, as measured in the Mach-Zehnder interferometer at different frequencies in Faraday geometry. The shift of the resonance frequency can be identified in intensity and phase.

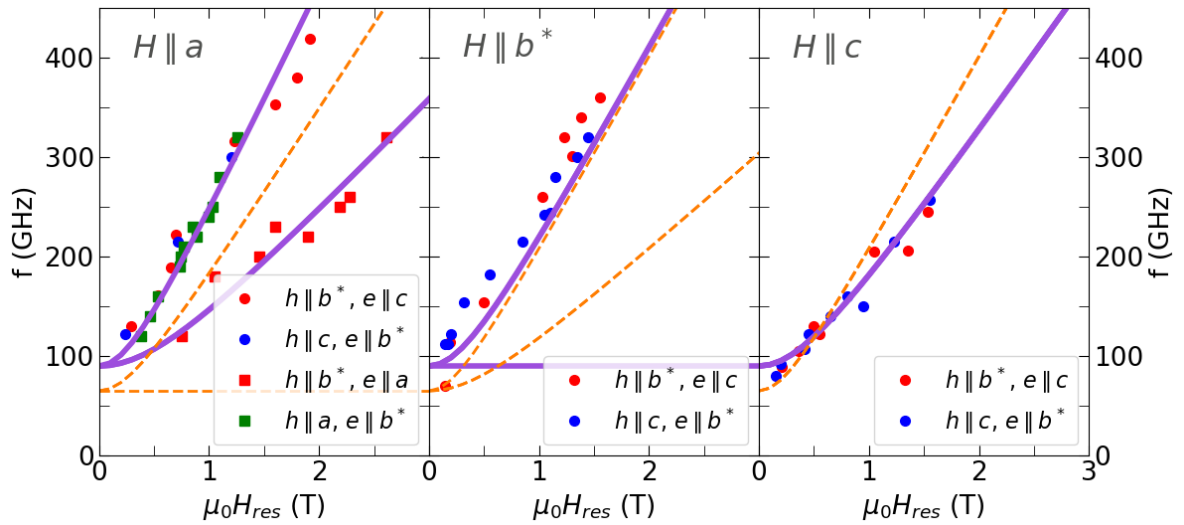


Figure 5.12: The different modes of the paramagnetic resonance are plotted for the external field along the main crystallographic axes ( $a$  - left,  $b^*$  - middle,  $c$  - right). All possible polarizations were measured for the  $a$ -cut sample (circles) and complemented by two sets of measurements on the  $c$ -cut sample (squares) for  $H \parallel a$ , to cover most of the possible excitation conditions (green -  $h \parallel a$ , red -  $h \parallel b^*$ , blue -  $h \parallel c$ ). The model from Chapter 5.1 (dashed orange) is assumed a splitting of  $\Delta = 65$  GHz. The extension of the model, as developed in Chapter 5.2 (solid violet) assumed  $\Delta = 90$  GHz, as explained in more detail in the text.

prediction of the new model. Furthermore the value of  $\Delta$  will be adjusted by a more accurate analysis of the data.

As shown in Fig. 5.11 the paramagnetic resonance appears in field scans at fixed frequencies as a distorted Lorentzian in the relative transmission and phase shift. By fitting both curves simultaneously, the resonance field can be extracted, even though the change in signal is rather small and somewhat distorted, possibly due to the small amount of Ho-ions in the compound. The resonance fields extracted are shifted to slightly larger field strengths compared to the values, which were simply read out of the raw data and used for the simple model (Chapter 5.1). In general the gyromagnetic ratio  $g$  can be different for different directions of applied field and different polarizations of the magnetic  $ac$ -field of the incoming light beam. Therefore we tested all possible combinations within the  $a$ -cut sample and complemented it with two measurements of the  $c$ -cut sample ( $h \parallel a$  and  $h \parallel b^*$  for an applied field  $H \parallel a$ ). Plotting the resonance fields as a function of the frequency of the incoming light reveals the expected linear behaviour at larger fields, with a slope corresponding to the  $g$ -factor (Fig. 5.12). At low fields the resonance frequencies converge to the value of the splitting of the non-Kramers doublet, where the frequency of

90 GHz corresponds to a splitting of  $\Delta = 4.3$  K. This is slightly larger than the previous estimate, due to the refined fitting of the data, as mentioned above.

Another valuable information that can be gained by analyzing this set of measurements is the number of modes that can be excited for each direction of magnetic field. While two modes are observed for an applied magnetic field along the  $a$ -axis, only one mode is observed for  $H \parallel b^*$  and  $H \parallel c$ , respectively. However, it is essential to note that only a minimum number of modes can be identified for certain, since the modes might be so close to each other that they cannot be separated due to the unevenly shaped absorption line. Nevertheless, the model fits the experimental data so well that it confirms the assumption of only two easy axes being present for each of the three Ho-sites. However, it remains unclear why the two modes for  $h \parallel b^*$  for an applied field  $H \parallel a$  appear in two different cuts of the sample.

### 5.2.6 Induced Electric Polarization

The derivation of the electric polarization at a given Ho-site induced by an external magnetic field was based on the  $C_2$ -symmetry of the magnetic moments. Since the presented extension of the model allows for a local breaking of this symmetry a more general approach has to be chosen. As we are only interested in the polarization in  $c$ -direction of the sample, it is sufficient to consider only the energy terms, which include the  $\hat{\mathbf{z}}$ -component of the electric field:

$$\begin{aligned} \mathcal{H}_z(E_z) = & -C_1 E_z H_x \mu_y - C_2 E_z \mu_x H_y - C_3 E_z \mu_x \mu_y - C_4 E_z H_x H_y \\ & -C_5 E_z H_x \mu_z - C_6 E_z \mu_x H_z - C_7 E_z \mu_x \mu_z - C_8 E_z H_x H_z. \end{aligned} \quad (5.19)$$

Here  $C_{1-8}$  denote different constants. Higher orders were neglected for simplicity. The electric polarization of a single Ho-ion can be derived by taking the partial derivative in respect to  $E_z$  (see Eq. 3.2). This expression can then be simplified in two steps. First, by considering that the magnetic moment lies in the  $\hat{\mathbf{x}}\hat{\mathbf{z}}$ -plane of each ion ( $\mu_y = 0$ ). Second, the summation over all three Ho-sites

$$P_z = \sum_{i=1}^3 p_z^i \quad (5.20)$$

leads to a cancellation of a few terms, due to the threefold symmetry of the crystal's  $c$ -axis. The final expression consists of only three terms<sup>4</sup>

$$p_z = -\frac{\partial \mathcal{H}_z}{\partial E_z} = c_1 \mu_x H_y + c_2 \mu_z H_x + c_3 \mu_x H_z. \quad (5.21)$$

<sup>4</sup>For the sake of simplicity, we redefined the constants  $c_1 = C_2, c_2 = C_5, c_3 = C_6$

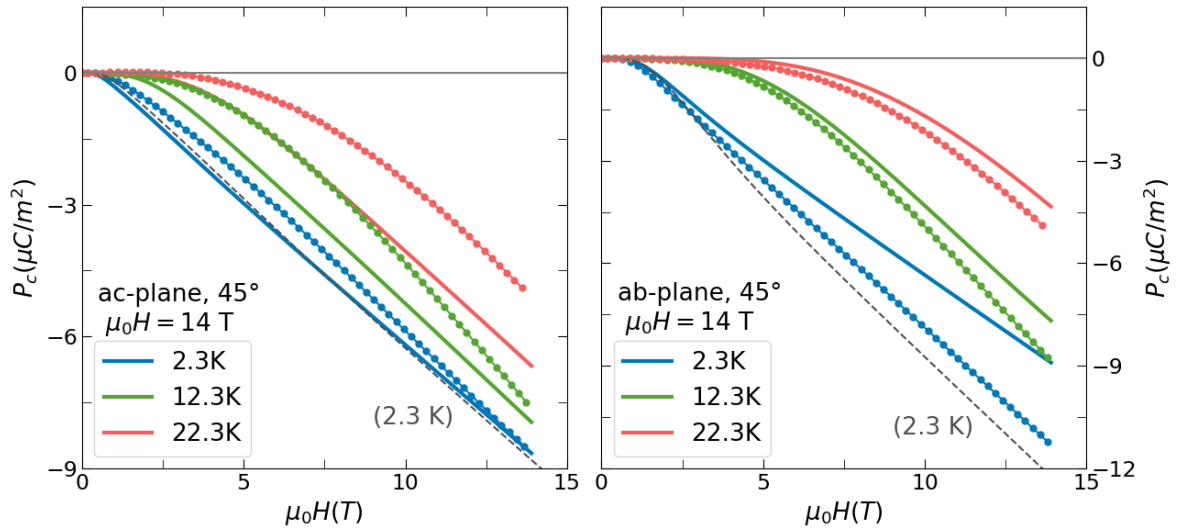


Figure 5.13: The magnetolectric effect can be directly observed by measuring the electric polarization for an applied magnetic field. Here the polarization along the samples  $c$ -axis is measured, while the magnetic field is applied in the  $ac$ -plane (left) and the  $ab$ -plane (right) under an angle of  $45^\circ$  with respect to the  $a$ -axis in both cases. The theoretical curve of the model presented in Chapter 5.1 is shown for 2.3 K (dashed). No magnetolectric effect can be observed for magnetic fields along the main crystallographic axes.

Therefore only three parameters<sup>5</sup> ( $c_1, c_2, c_3$ ) had to be fitted, using a similar fitting algorithm, as presented above, resulting in the values, which are given in Table 5.3.

$c_1$	$c_2$	$c_3$
0.151	0.288	0.089

Table 5.3: Constants determined from the fitting of the polarization, as given by Eq. (5.21).

The main disadvantage of the simple model was the poor agreement of the shape of the electric polarization, when plotted as a function of the magnetic field direction (Figs. 5.3 and 5.14). While the sweeping of the field in the  $ac$ -plane results in a peak, which is shifted compared to the simple model, the measurement in the  $ab$ -plane led to a different position of the sharp jumps in polarization, analogous to the measurement of the magnetic torque in that plane. As shown in Fig. 5.14, both inconsistencies were overcome by the extended model. The remaining difference of the new model and the experiment

<sup>5</sup>The magnetic structure assumed in Chapter 5.1 did lead only to two terms in this expression:  $C_1\mu_y H_x + C_5\mu_z H_x$ .

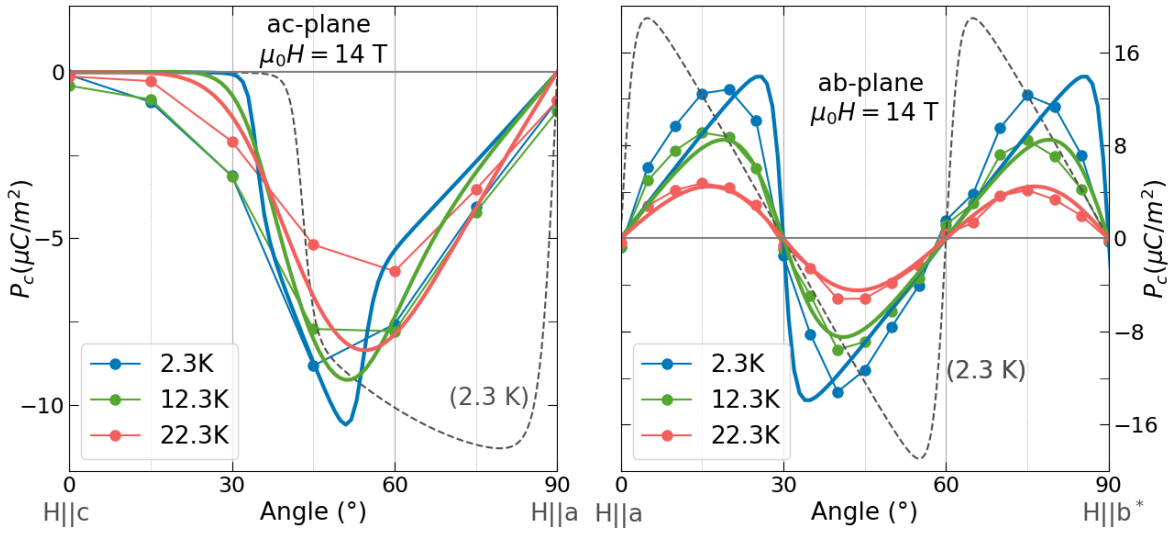


Figure 5.14: The electric polarization induced by an applied magnetic field as the function of the field direction. The measurement points were extracted from the 14 T field scans (see Fig. 5.13), where the field was rotated across the crystal's *ac*-plane (left) and *ab*-plane (right). The theoretical curve of the model presented in Chapter 5.1 is shown for 2.3 K (dashed). In agreement with symmetry considerations, no magnetoelectric effect could be observed for fields in the  $b^*c$ -plane.

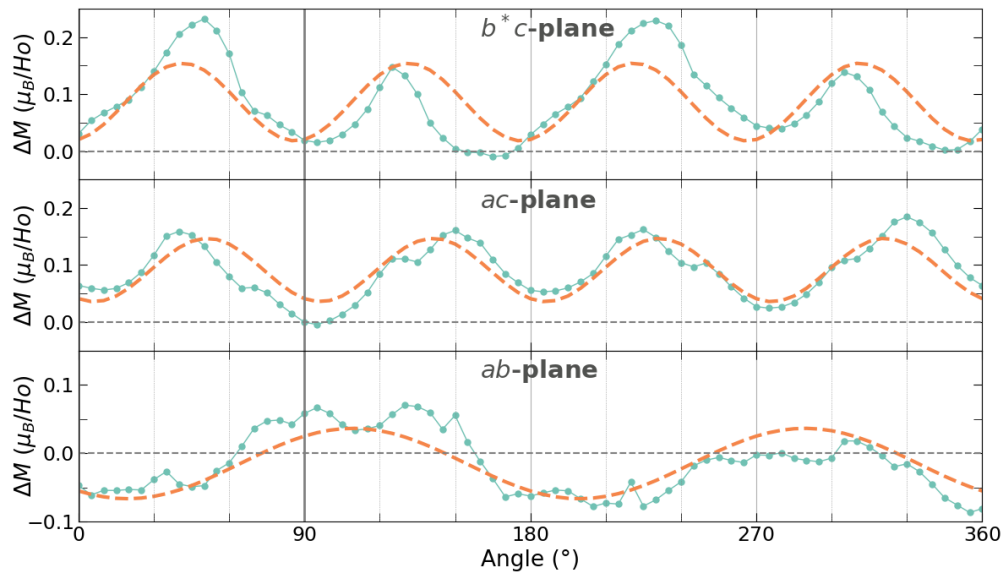


Figure 5.15: The difference of theoretically predicted and experimentally attained angular dependence of the magnetization at 5 K and 5 T (see Fig. 5.7). Dashed lines are fits with sine curves, as discussed in the text.

might be explained by small misalignments of the sample (Fig. 5.13). However, the polarization as a function of the magnetic field strength seems to fit better to the simple model (Fig. 5.4).

### 5.2.7 Open Questions

As described above, the extended model manages to reproduce the presented measurements reasonably well, even though no perfect agreement is achieved. In most cases this might be explained by a misalignment of the sample in the measurements or other experimental artifacts. Nevertheless, this has to be analyzed thoroughly, the remaining drawbacks in the presented model need to be discussed and the open questions will be formulated in the following.

As given in Table 5.2, the largest disagreement in describing the magnetic torque and the angular dependent magnetization might be found in the scaling parameter  $\lambda = 0.47$ , which suggests that the magnetization in the sample is in fact more isotropic than calculated in the model. However, even with this scaling factor a systematic error is present, when comparing experiment and theory, which is shown by their subtraction in Fig. 5.15 for the magnetization and in Fig. 5.16 for the torque measurements. A very stable periodicity catches the eye in both cases, which is illustrated by fitting the residuals with sine curves. For the magnetization of  $b^*c$ - and  $ac$ -plane a fit with a  $\sin(4\theta)$  is presented and for the  $ab$ -plane a fit with a  $\sin(2\phi)$  curve. The residuals of the magnetic

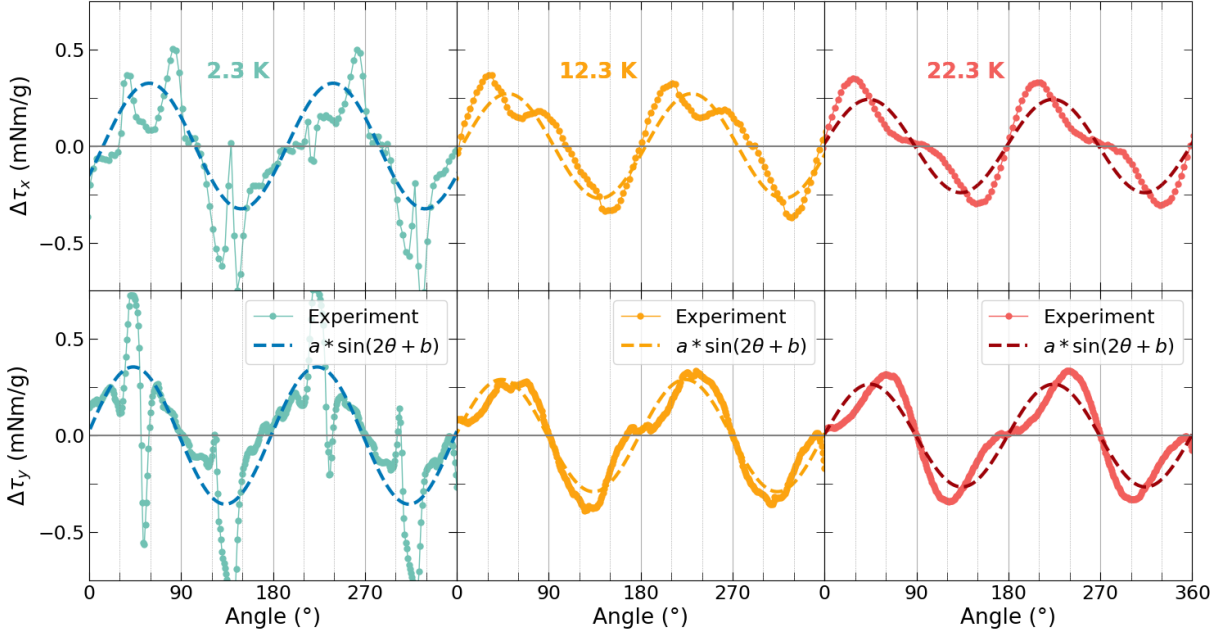


Figure 5.16: The difference of theoretically predicted and experimentally attained magnetic torque (Fig. 5.8) in  $b^*c$ - (top) and  $ac$ -plane (bottom) at 2.3 K, 12.3 K and 22.3 K (left to right). Dashed lines are fits with sine curves.

torque reveals also a  $\sin(2\delta)$  for all sample planes. A connection between these residuals and the sample symmetry (cubic for magnetization, thin plate for torque) is so far merely speculative, but calls for further investigation. This additional contribution to the magnetization leads to a problematic asymmetry of the magnetization around the crystal's  $c$ -axis in the  $b^*c$ -plane, as seen in Fig. 5.7, which contradicts the symmetry of the model. However, we neglected in this approach the small difference of the distance  $d_1$  and  $d_2$  of the Si/Ga- to the Ho-sites. This approximation might be the reason for this discrepancy.

In both previously described models, the induced magnetization and the magnetoelectric effect are driven by the lowest lying doublet, whilst other levels are only accounted for in the van-Vleck paramagnetism, which assumes the next level is at an energies  $E_1$ , which satisfy  $E_1 - E_0 \gg k_B T$ , where  $E_0$  is the ground level [84]. Therefore no deviations of the linear relation between magnetic field and induced electric polarization at larger fields are expected in these approaches. Nevertheless, we were able to explore the magnetoelectric effect beyond the model, by measurements in pulsed magnetic fields of up to 56 T, which are presented in Fig. 5.17. The induced electric polarization along the  $c$ -axis was measured for different directions of magnetic field in the  $ab$ - and  $ac$ -plane, respectively. The observed high-field anomalies are of a strikingly different nature for the two planes: while a decrease of electric polarization can be observed for certain directions of

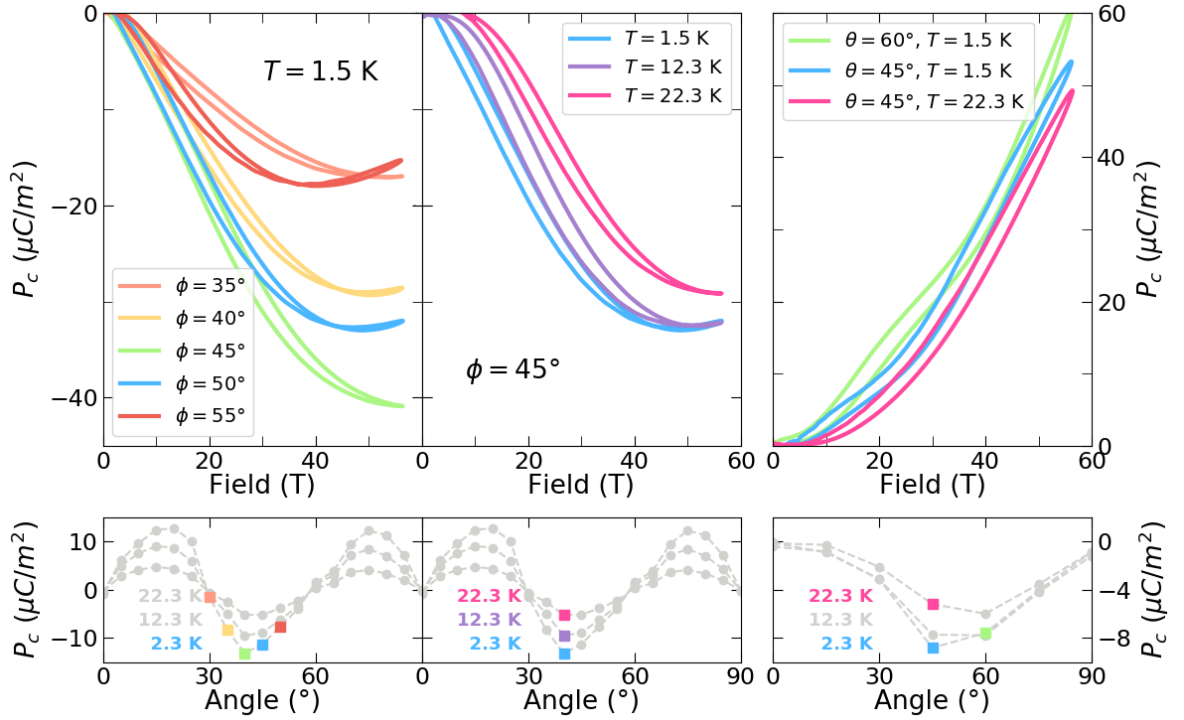


Figure 5.17: **top** The induced electric polarization by a pulsed magnetic field of up to 56 T for certain directions in the  $ab$ - (left) and  $ac$ -plane (right), respectively. The combination of field direction and temperature, which was used for each pulse, is shown in the legend in each plot. **bottom** The corresponding low field (14 T) measurement points (see Fig. 5.6) are presented to facilitate the identification of the high-field features. Note that a different base temperature was used to allow for stable measurements.

fields in the  $ab$ -plane, there is no such slow-down of the effect for fields in the  $ac$ -plane. Quite the contrary, the linear magnetoelectric effect, which is observed at low temperatures above a few Tesla, transforms into a second linear regime with an even larger slope at field strengths between 20-40 T. The temperature dependence reveals expectedly a slight weakening of the MEE at larger temperatures.

These high-field features most likely correspond to the admixture of higher levels, which is not accounted for in the presented model and, therefore, requires a further expansion. The experimental identification of the crystal field levels by spectroscopic methods would be strongly desired to complete the description of the system. Resolving the occupation of the Ga/-Si sites in the vicinity of the magnetic Ho-ions would be an additional major help in confirming the presented theory and answering the open question, along with further measurements, like repeating the investigations on  $\text{Ho}_x\text{La}_{3-x}\text{Ga}_5\text{SiO}_{14}$  with different Ho-content.

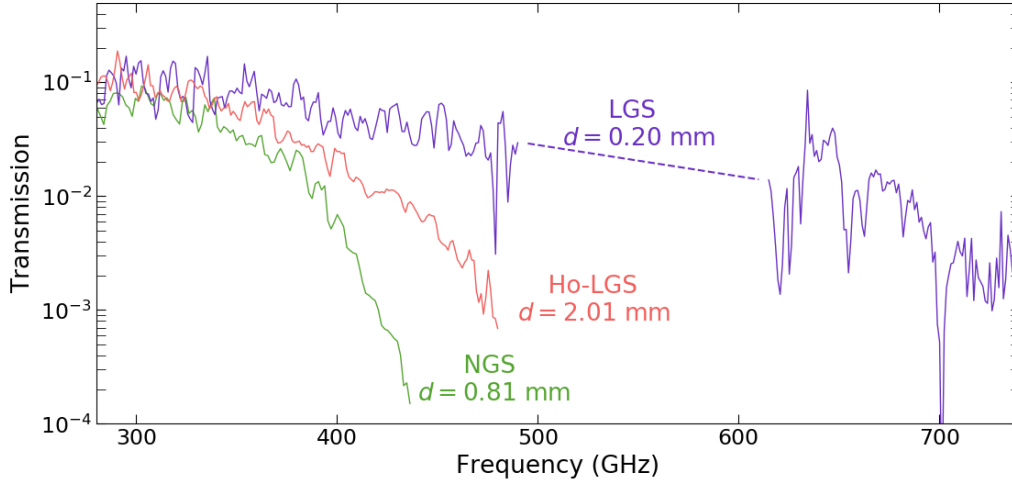


Figure 5.18: Transmitted intensity of three different compounds of the rare-earth langasite family at 1.8 K. The different thicknesses of the plane-parallel  $a$ -cut samples from  $\text{La}_3\text{Ga}_5\text{SiO}_{14}$  (violet),  $\text{Ho}_x\text{La}_{3-x}\text{Ga}_5\text{SiO}_{14}$  (red) and  $\text{Nd}_3\text{Ga}_5\text{SiO}_{14}$  (green) are given in the plot.

### 5.3 Electron-Phonon Coupling in Rare-Earth Langasites

As described in Chapter 5.2.5, we measured the paramagnetic resonances in a sub-THz interferometer. In this section we will discuss the finding of another intriguing feature of Ho-LGS, which was observed in frequencies  $< 500$  GHz. As presented in Fig. 5.18 a strong absorption at zero magnetic field was discovered in the investigated sample of  $\text{Ho}_x\text{La}_{3-x}\text{Ga}_5\text{SiO}_{14}$  and other compounds of the langasite family (not all shown), including the prototype  $\text{La}_3\text{Ga}_5\text{SiO}_{14}$ , which we identify as a strong low-frequency phonon. Nevertheless this experimental setup could only reveal the left side of the mode, since the sample is not transparent up to at least 1 THz - the cut-off of the high frequency backward wave oscillator. Therefore, the phonon spectra were further studied in the infrared frequency range by thoroughly measurements in [85] with a Fourier-transform interferometer. However, the combination of the considerable frequency resolution of the backward wave oscillators with the 7 T magnet allowed the discovery of a sensitivity of this phonon to magnetic fields. As discussed in the following, an applied field along the crystal's  $c$ -axis seems to lead to a narrowing of the phonon mode, while the application of magnetic fields along  $a$ - and  $b^*$ -axis did not reveal any impact.

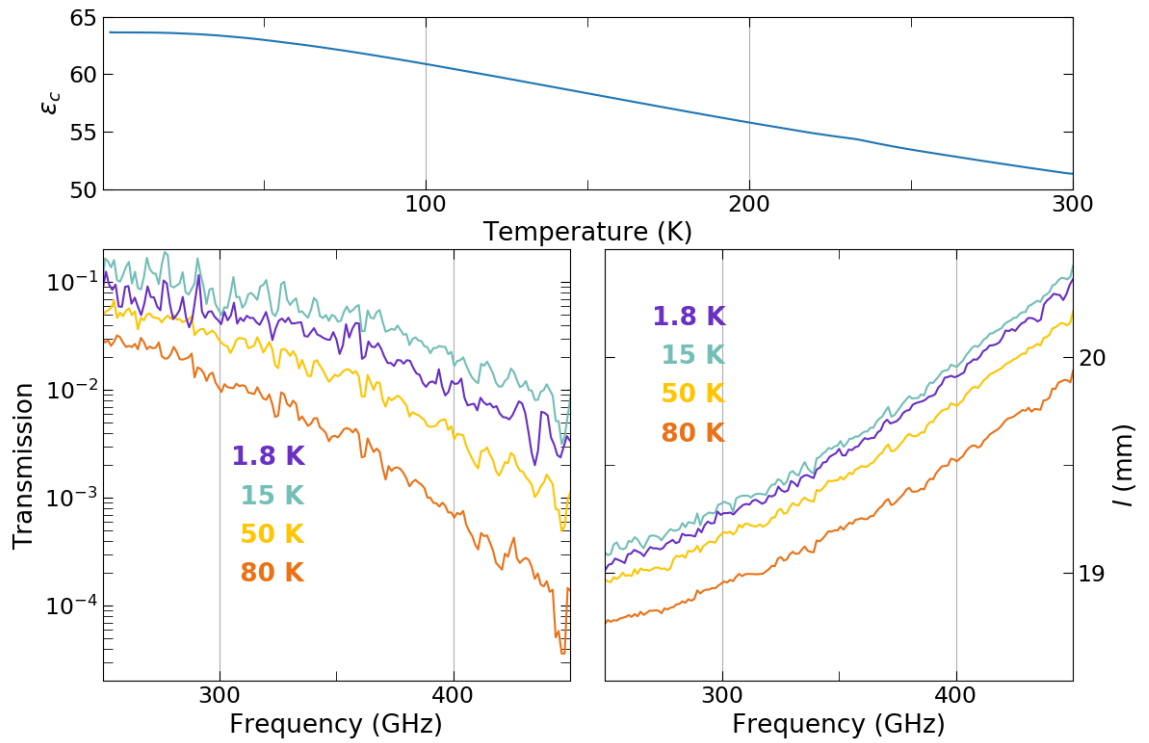


Figure 5.19: **top** The dielectric permittivity measured along the crystal's  $c$ -axis as a function of temperature, measured at a frequency of 1 kHz. **bottom** Transmission (left) and optical thickness  $l = nd$ , where  $n$  is the refractive index and  $d$  the geometrical thickness of the sample (right) of a linearly polarized ( $h \parallel b^*$ ,  $e \parallel c$ ) monochromatic electromagnetic wave through a Ho-LGS sample ( $a$ -cut), measured at zero magnetic field and different temperatures (color).

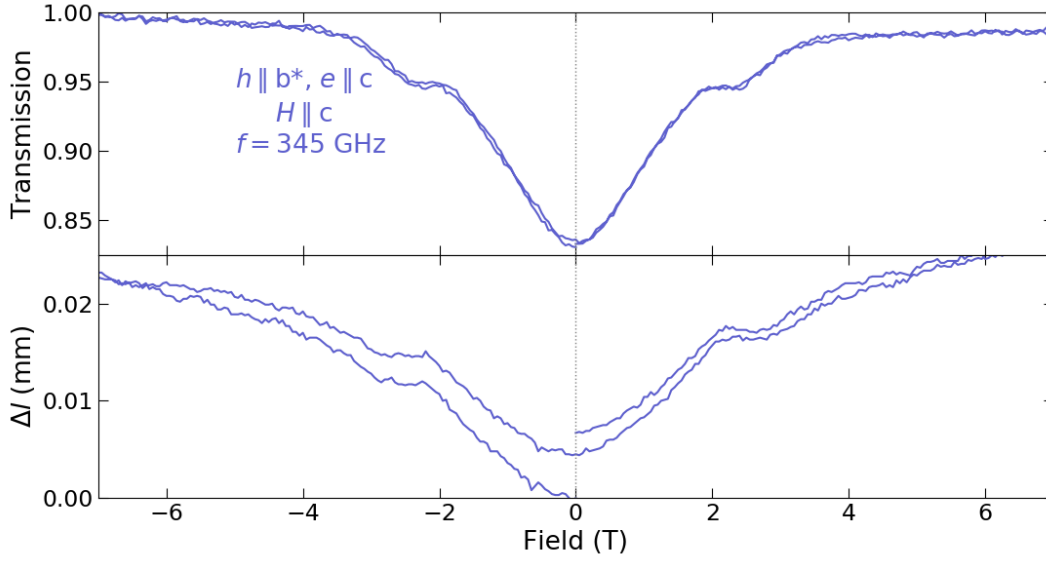


Figure 5.20: The change of transmission (top) and change of optical thickness  $l$  (bottom) of an electromagnetic wave with a frequency of 345 GHz, which is linearly polarized with  $h \parallel b^*$  and  $e \parallel c$ , under the variation of an external magnetic field  $H \parallel c$ .

## 5.4 Excitation in the Complex Transmission

The dielectric permittivity  $\varepsilon_c$  of compounds of the langasite family are known to have relatively large values [64]. The doping of the prototype LaGaSiO with 1.5% Ho-ions does not effect the temperature dependence by much, as shown in the top panel of Fig. 5.19. Nevertheless, we are the first to measure a low frequency phonon, which can be partly attributed for the large value of  $\varepsilon_c$  (Fig. 5.18).

The sensitivity to magnetic field of the phonon was first observed in an attempt to measure the paramagnetic resonance at 345 GHz in a magnetic field scan (Fig. 5.20). The absorption at the resonance field of about 2 T is dominated by a strong absorption in the range of 0-4 T. The measurement of the spectra at different magnetic field strengths (Fig. 5.21) confirms that this effect seems to be well pronounced at fields below 4 T and decreases for larger fields (see Fig. 5.20). Using its thickness, the transmission and phase shift of an electromagnetic wave through the sample can be converted into the complex dielectric permittivity  $\varepsilon^*$ . The excitation of the phonon can be observed in the spectrum of  $\varepsilon^*$  as a Lorentzian function

$$\varepsilon^*(\omega) = \varepsilon(0) + \Delta\varepsilon \frac{\omega^2 + i\omega\gamma}{\omega_0^2 - \omega^2 - i\omega\gamma}. \quad (5.22)$$

Therefore we can extract the static dielectric permittivity  $\varepsilon(0)$ , the strength of the exci-

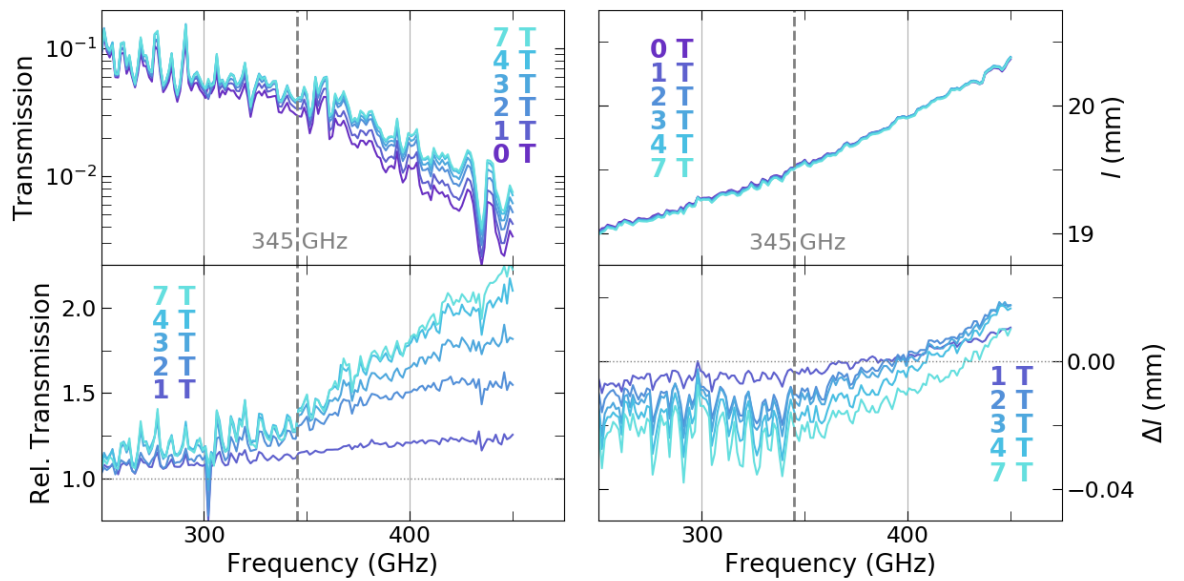


Figure 5.21: Field dependence of the phonon at 1.8 K. The frequency of Figure 5.20 (345 GHz) was indicated by a gray dashed line. **top** Transmission (left) and optical thickness  $l$  (right) of a linearly polarized ( $h \parallel b^*$ ,  $e \parallel c$ ) monochromatic electromagnetic wave through a Ho-LGS sample ( $a$ -cut), measured at different strengths (color) of the magnetic field, which was applied in along the crystal's  $c$ -axis (Voigt geometry). **bottom** For a better visualisation of the change of signal (and optical thickness), it was divided (subtracted) by the zero field signal (optical thickness).

tation  $\Delta\varepsilon$ , the resonance frequency  $f_{\text{res}} = \omega_0/2\pi$  and the damping parameter  $\gamma$  by fitting the measured complex transmission for different temperatures (Fig. 5.22). However, since only the information of the phonon's left side is given, we had to acknowledge that this set of parameters provided too many degrees of freedom to fit the subtle differences under the application of magnetic field. This can be understood, when approximating  $\omega \ll \omega_0$  in Eq. 5.22. In this limit, we can assume the real and imaginary part to be

$$\varepsilon'(\omega) \approx \varepsilon(0) - \frac{\Delta\varepsilon}{\omega_0^2}\omega^2 \quad (5.23)$$

and

$$\varepsilon''(\omega) \approx \frac{\Delta\varepsilon}{\omega_0^2}\gamma\omega, \quad (5.24)$$

respectively. While the real part allows for determining  $\varepsilon(0)$  by the zero-frequency limit and  $\frac{\Delta\varepsilon}{\omega_0^2}$  by its quadratic slope, the imaginary part can be used for extracting  $\gamma$ . However, a separation of  $\Delta\varepsilon$  and  $\omega_0$  cannot be achieved in this frequency regime, if the changes are small. Therefore, we fixed one of the two parameters ( $\Delta\varepsilon$ ), when fitting the magnetic field dependence.

This analysis provided several interesting insights. First of all, the increase of the static permittivity along the  $c$ -axis for a decrease of temperature cannot be explained by the change of the low-frequency phonon, since its static contribution,  $\Delta\varepsilon$ , unexpectedly decreases with decreasing temperature. Even more interestingly, we can attribute the change of complex transmission under the application of a magnetic field of up to 4 T to a decrease of  $\gamma$ , i.e. a narrowing of the phonon. Above this field no significant changes of the phonon parameters can be identified. The origin of this sensitivity to magnetic fields might be a coupling of the crystal field levels of the magnetic Ho-ion to the vibrational phonon mode. However, the determined parameters suggest a variation of  $\varepsilon_\infty = \varepsilon(0) + \Delta\varepsilon$ , i.e. a sensitivity to magnetic fields of excitations at higher frequencies. Nevertheless, understanding the microscopic mechanisms behind the excitation and alteration of the phonon calls for further investigation in complementary experimental setups.

Even though the high frequency side of the phonon excitation can be observed in a Fourier-transform infrared spectrometer, an attempt to get further information about the sensitivity to magnetic fields failed. Unfortunately the resolution is not sufficient to reveal any signal in the relative spectra.

For a comprehensive study of the phonon spectra with special attention to the temperature dependence of Ho-langasite and further compounds of the langasite family, we refer to [85].

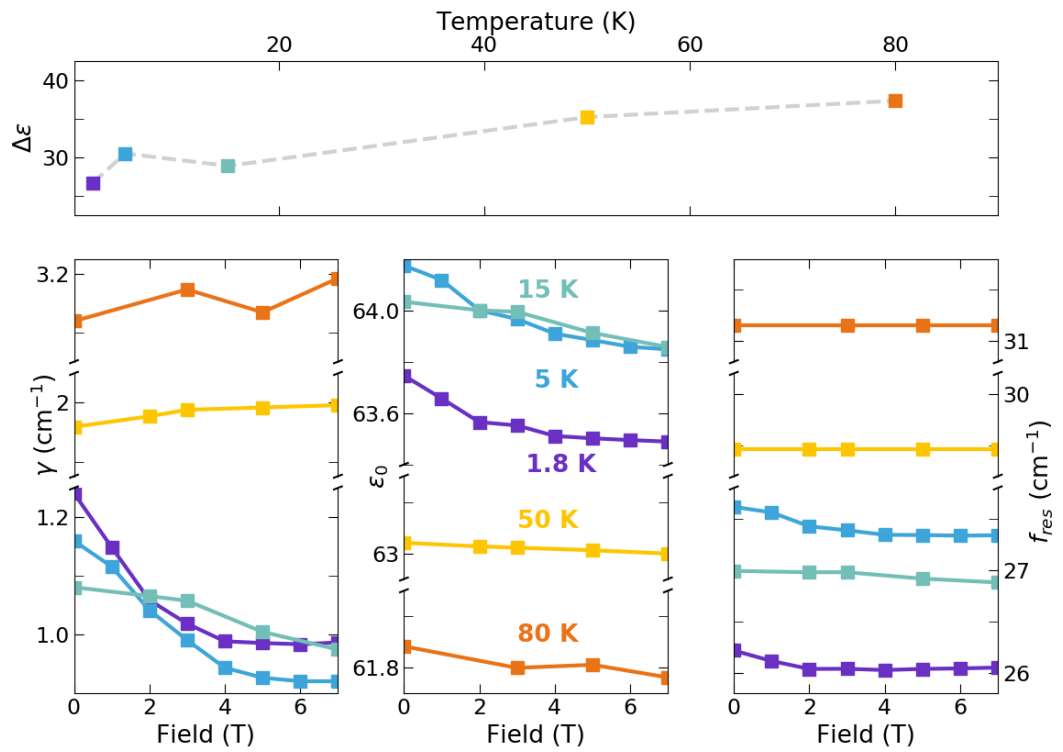


Figure 5.22: Parameters for fitting the the low-frequency phonon (Fig. 5.21 and 5.19) as a Lorentzian, as described in Eq. (5.22).  $\Delta\epsilon$  (top) was assumed to be independent on the magnetic field, while the change of  $\gamma$ ,  $\epsilon_0$  (along  $c$ -axis) and  $f_{\text{res}}$  are shown (bottom) for each temperature (color).

## 5.5 Summary

We presented an extensive study of the magnetic and magnetoelectric properties of  $\text{Ho}_x\text{La}_{3-x}\text{Ga}_5\text{SiO}_{14}$ . An unusual MEE was discovered for the polarization along the crystal's  $c$ -direction, which is linearly dependent on the strength of the magnetic field, but oscillates six times upon the rotation of the field in the  $ab$ -plane of the compound. This effect could be qualitatively modeled by two approaches, assuming two different magnetic structures of the system. Already the assumption of one local easy axis for each of the three Ho-sites is sufficient to reproduce the main features of the observed phenomenon. However, the investigation of the magnetic properties revealed a more complex magnetic anisotropy, indicating the presence two local easy axes for the Ho-ions. However, a scaling factor had to be introduced, to be able to model the magnetic and magnetoelectric properties simultaneously. Furthermore, a coupling of an applied magnetic field to a low-frequency phonon was observed. By extracting the parameters describing this excitation, we concluded that the application of a magnetic field along the crystal's  $c$ -axis leads to a narrowing of the phonon resonance.



# 6 Identifying Quantum Phase Transitions by Torque Magnetometry

In this chapter, two realizations of resolving the magnetic phase diagrams of two magnetoelectrics by torque magnetometry are presented. In many cases the measurement of the magnetization curves is not sufficient to indicate the correct microscopical structure of the magnetic moments, but additional information about the magnetic anisotropy is needed, which can be provided by measuring the magnetic torque. At least, an accurate measure, which is complementary to measuring the induced magnetization, of the exact transition fields and temperatures can be offered by this experimental method, as presented for two different materials, namely in the polar magnetoelectric multiferroics  $\text{GaV}_4\text{S}_8$  [86; 87] and  $\text{Mn}_2\text{Mo}_3\text{O}_8$  [88; 89].

## 6.1 Transition of Cycloidal Phase to Skyrmion Lattice in $\text{GaV}_4\text{S}_8$

The polar magnetic semiconductor  $\text{GaV}_4\text{S}_8$  is paramagnetic down to a temperature of 13 K. Below this temperature it presents delicate structured magnetic phase diagram, including a cycloidal phase and the first observation of a Néel-type skyrmion lattice phase in a bulk crystal ever reported [90]. In this section we show the proof of principle that such a quantum phase diagram can easily be resolved by the torque magnetometer option of a PPMS (Chapter 2.2.4).

### Skyrmions in Lacunar Spinel Chalcogenides

Recent scientific attraction was caused by the experimental observation of topologically-stable magnetic vortex textures [91], so-called skyrmions, which have been already theoretically studied since 1989 [92] and are thought to have intriguing applications as spintronic devices, like transistors or memory devices [93]. Skyrmions are distinguished by the type of rotation of the spins into Bloch- and Néel-type skyrmions (schematically shown in Fig. 6.1), while also a novel combination of both types were recently observed, the so-called anti-skyrmions [94].

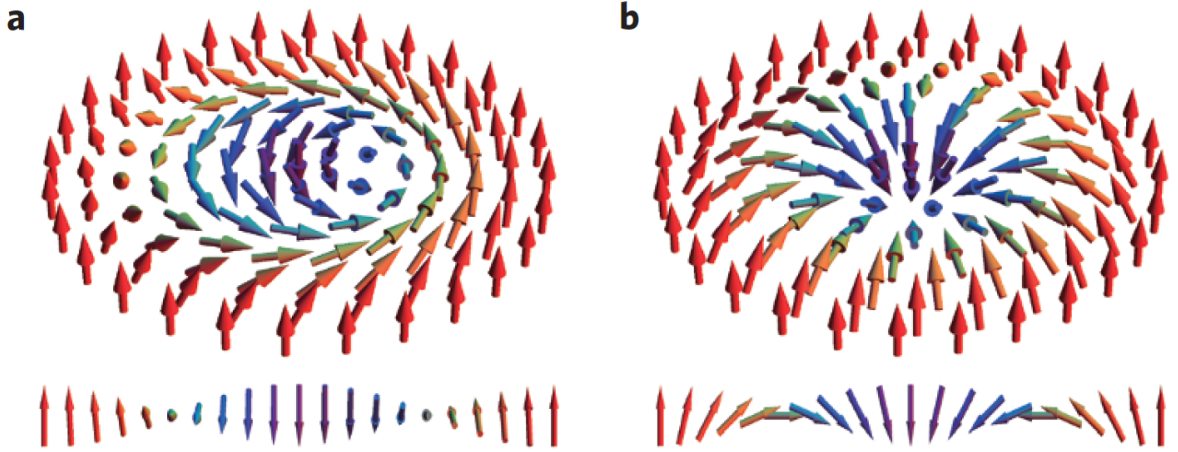


Figure 6.1: Spin structure of a Bloch- (a) and Néel-type skyrmion and the corresponding cross-sections. The image was directly taken from [90].

The family of lacunar spinel chalcogenides  $AM_4X_8$  ( $A = \text{Ga, Ge}$ ;  $M = \text{V, Nb, Ta}$ ;  $X = \text{S, Se}$ ) consist of transition metal clusters  $M_4$  as the magnetic building blocks, which large separation induces a Mott insulators state in the crystal. Furthermore, these compounds were investigated for a rich variety of interesting physical phenomena, like pressure-induced superconductivity [95], colossal magnetoresistance [96] and magneto-electric multiferroicity [97].

The compound  $\text{GaV}_4\text{S}_8$  belongs at room temperature to the  $F\bar{4}3m$  space group, but undergoes a structural transition by cooling below a temperature of  $T_S \approx 40 \text{ K}$  into the rhombohedral  $R3m$  space group [86; 98], followed by a magnetic transition at  $T_C = 13 \text{ K}$ , first solely connected to the emergence of a ferromagnetic order [98]. However, a more complicated magnetic phase diagram was resolved, which lead to the first observation of a Néel-type skyrmion in a bulk crystal [90].

The magnetic phases and the corresponding phase transitions below  $T_C$  were identified in [90] by measuring the magnetization curves along three crystallographic axes ( $[100], [110], [111]$ ). Within the  $M(H)$  measurement, the transitions can be observed as direction-dependent step-like features. However, it could be argued that the steps are not very well pronounced, which brings some difficulties in pinpointing the exact transition field and temperature. Therefore we examine the phase transition by torque magnetometry (Chapter 2.2.4) and propose this approach to measure and identify quantum phase transitions.

### 6.1.1 Identifying Phase Transitions by Magnetic Anisotropy

The investigated sample is a thin plane-parallel plate, cut along the  $[111]$ -plane. As described in [90], the crystal has four different easy axes ( $[111], [11\bar{1}], [\bar{1}11], [\bar{1}\bar{1}\bar{1}]$ ). For

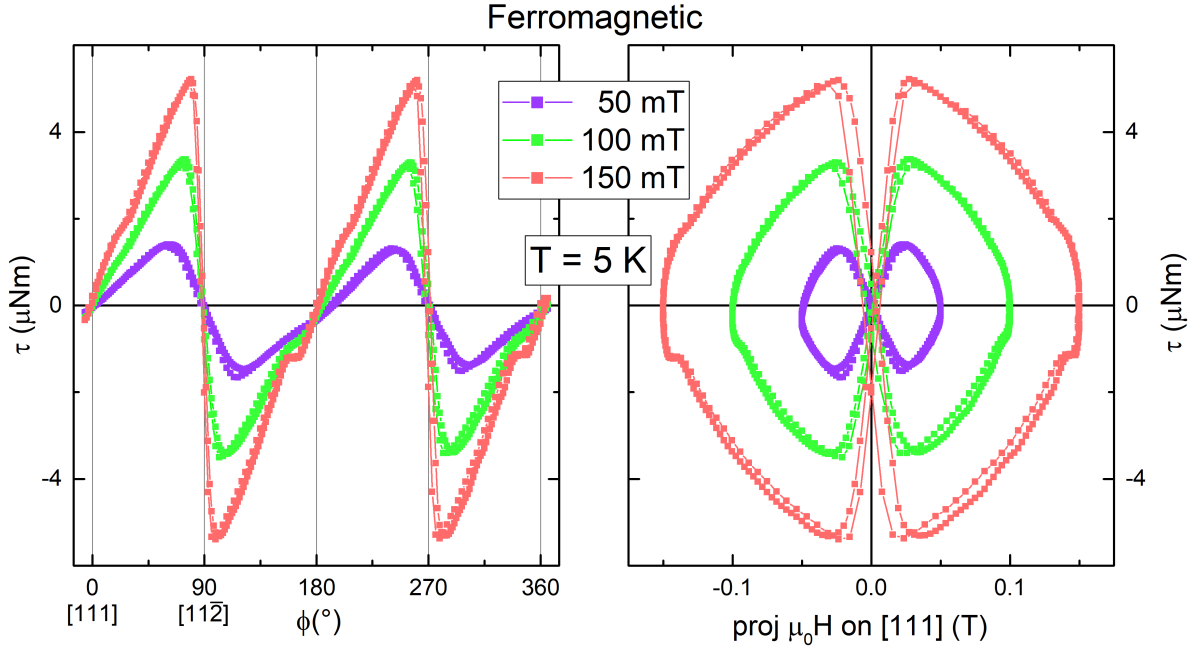


Figure 6.2: The magnetic torque along the  $\text{GaV}_4\text{S}_8$  crystal's  $[1\bar{1}0]$  direction at a temperature of 5 K at different field strengths after cooling in a magnetic field of 9 T along the crystal's  $[111]$  axis. The sharp jump at  $\phi = 90^\circ$  in the angular dependence (left) indicates that the easy axis is along the crystal's  $[111]$  direction ( $\phi = 0^\circ$ ). This is visualized in plotting the magnetic torque against the projection of the magnetic field on the  $[111]$  axis (right): The sign of  $\tau$  changes simultaneously with the sign of the projected  $\mathbf{H}$ . The observation of only one easy axis confirms that a magnetic single domain state was achieved during cooling in the magnetic field.

achieving a single domain state, a magnetic field of  $\mu_0 H = 9 \text{ T}$  was applied along the crystal's  $[111]$  direction in the cubic phase, while cooling it down until the rhombohedral phase was reached. To check if the selection of one single easy axis was successful, the magnetic torque  $\tau$  was measured as a function of the field direction in the  $[1\bar{1}0]$  plane. The results, shown in Fig. 6.2, reveal that indeed this single domain state was achieved, with the easy axis along  $[111]$ . Plotting the magnetic torque versus the projection of the magnetic field on this axis is a useful visualization of this spin flip.

Next, the cycloidal phase was characterized by measuring the magnetic torque at small magnetic fields of  $\mu_0 H = 20 \text{ mT}$  and at temperatures of 8.5 K and 10 K, where no unexpected features were observed. The angular dependence resembles a  $\sin(2\phi)$ , which satisfies the symmetry of the rotation of a thin plate sample in a fixed magnetic field. The small values correspond to the small net magnetization as measured in [90].

Finally, the transition of the cycloidal phase into a skyrmion lattice was determined

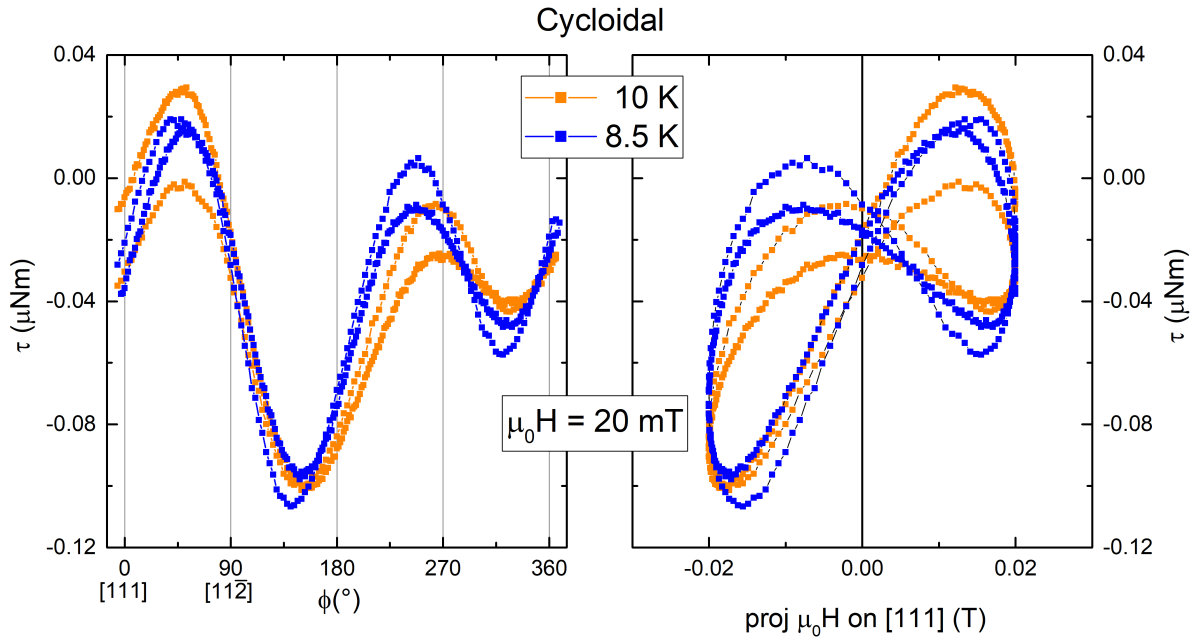


Figure 6.3: The magnetic torque along the  $\text{GaV}_4\text{S}_8$  crystal's  $[1\bar{1}0]$  direction in an applied magnetic field of 200 Oe and at temperatures of 10 K (orange) and 8.5 K (blue) after cooling in a magnetic field of 9 T along the crystal's  $[111]$  axis. The observed magnetic torque is rather small and exhibits an uneven shape. This might be a result of experimental artifacts like some misalignment of the sample or mechanical stress in the sensor.

(Fig. 6.4). For this purpose it is important to bear in mind that only one easy axis is present in the sample. Therefore it proves useful to take into the projection of the magnetic field onto the  $[111]$  direction, as shown in Figs. 6.2, 6.3, 6.4 on the right side. In this way, the exact position of the transition in the field-temperature diagram can be determined. We extract by the two presented measurements that the magnetic transition occurs for a temperature of 11 K at a field of 30 mT and for 12 K at 25 mT. This fits very well the previously determined values in [90].

## 6.2 Magnetic anisotropy in the antiferromagnetic multiferroic $\text{Mn}_2\text{Mo}_3\text{O}_8$

As reported in [99], the polar ferrimagnet  $\text{Mn}_2\text{Mo}_3\text{O}_8$  undergoes three different magnetically ordered phases, when an external field of up to 14 T is applied along the crystal's  $c$ -axis, as detectable by the different slopes in the magnetization curve Fig. 6.5b. To complement these measurements with additional information about the magnetic anisotropy, the magnetic torque around the crystal's  $c$ -axis was measured (Fig. 6.6). An extended

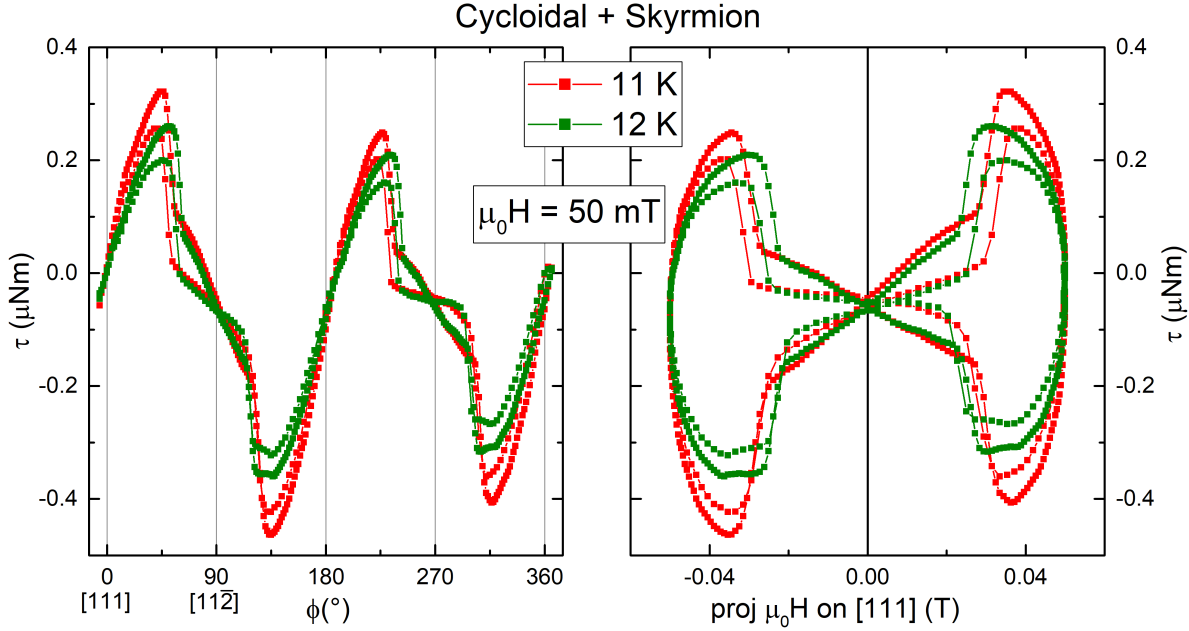


Figure 6.4: The magnetic torque along the  $GaV_4S_8$  crystal's  $[1\bar{1}0]$  direction at a temperature of 11 K (red) and 12 K (green) after cooling in a magnetic field of 9 T along the crystal's  $[111]$  axis. The two sharp jumps in the angular dependence (left) correspond to phase transitions between the cycloidal- and skyrmion-phase. For a better visualization  $\tau$  is plotted against the projection of the magnetic field on the  $[111]$  direction. The shift of the transition to lower fields for 12 K is in agreement with the literature values [90].

two-sublattice antiferromagnetic classical mean-field model was developed in [99], which is in good agreement with the experiment, as discussed in the following.

### 6.2.1 Manganese Molybdenum Oxide

The investigated sample, Manganese Molybdenum Oxide, is a compound of the  $M_2Mo_3O_8$  ( $M$  = transition metal) crystal family, which belongs to the polar  $P6_3mc$  space group. Interest in this material group arises from the exhibition of a strong magnetoelectric effect, which was recently observed in  $M = Fe$  and is considered the largest magnetically switchable electric polarization among single-phase multiferroic crystals [17; 100]. Furthermore, a vast amount of different spin structures, which can be transformed into each other by an external magnetic field, were observed in this material class, which still awaits for being fully described microscopically. For a first understanding of the magnetic properties of this crystal family, the measurement of three magnetic phases in the compound  $Mn_2Mo_3O_8$  offers a reasonable starting point [99]. The magnetic properties arise from the  $Mn^{2+}$ -ions ( $S = 5/2$ ,  $L = 0$ ) occupying sites, which are half octahedrally

coordinated and half tetrahedrally coordinated by oxygen anions.

## 6.2.2 Magnetization

Below the Néel temperature of  $T_N = 41.5\text{ K}$  the spins of the octa- and tetrahedral sites align antiparallel along the hexagonal axis of the crystal, i.e. the easy axis in the ferrimagnetic ground state [88]. At the lowest temperature the magnetic moments of both sites compensate each other, which is not the case at higher temperatures, indicating different temperature dependencies, giving rise to a spontaneous non-zero net magnetization. However, at lowest temperature the compensation of both moments can be lifted by the application of an external magnetic field [89], as measured in a Vibrating Sample Magnetometer for field strengths of up to 14 T and shown in Fig. 6.5. For fields perpendicular to the hexagonal  $c$ -axis a linear increase of magnetization is induced, while a field along the  $c$ -axis only induces a magnetization at field strengths above 4 T. While the compensation of moments still holds below this field, a smooth increase of the magnetization is induced above this transition field indicating a spin-reorientation. A second transition emerges when the magnetization asymptotically reaches the linear susceptibility of the  $\mathbf{H} \perp c$  case, which remains constant for up to 14 T.

## 6.2.3 Magnetic Torque

The microscopic model of the magnetic moments is developed based on the magnetization curves (Fig. 6.5) and the measurements of the magnetic torque, measured for angles around the crystal's  $c$ -axis. A plane-parallel  $c$ -cut sample was used for this investigation.

Below the first transition  $\mu_0 H_{C1}$  the magnetization curves are characteristic for easy axis antiferromagnets, i.e. zero magnetization for fields along the easy axis and a constant susceptibility for fields perpendicular to the easy axis. As visualized in Fig. 6.5 a,b the moments are assumed to be antiparallel along the crystal's  $c$ -axis and cant for the applied field  $\mathbf{H} \perp c$ , which leads to a non-zero magnetization along this direction. The relatively low values of the critical fields along the  $c$  axis and the identical susceptibility for  $\mathbf{H} \parallel c$  and  $\mathbf{H} \perp c$  in fields above  $H_{C2}$  indicate a nearly isotropic spin-system.

The smooth increase of the magnetization between the two transition fields, results from competing anisotropies. The magnetization is not parallel to the external field, as illustrated in Fig. 6.5b and described by the enclosed angle  $\theta_M$  in Fig. 6.5c. This angle should lead to a non-zero magnetic torque (Eq. 2.3). However, the system is unstable for magnetic fields along the  $c$ -axis, since the magnetization component perpendicular to the field has no preferred orientation in the  $ab$ -plane. Therefore the measurements of  $\tau$  were performed not only for an angle between field direction and  $c$ -axis  $\vartheta$  of  $\approx 0^\circ$ , where the preferred canting direction is induced by a non-controlled misalignment, but also with a controlled offset of  $\vartheta \approx \pm 1^\circ$  towards the crystal's  $a$ -axis (Fig. 6.6). The model calculations provide a good explanation for those angles, as presented in Fig. 6.6b. The characteristic peak in the magnetic field dependence of the magnetic torque in the

$H_{C1} < H < H_{C2}$  field regions, corresponds to the maximum of  $\theta_M$  (Fig. 6.5c). The small hysteresis observed at these fields for some angles are most likely explained by mechanical instabilities of the experimental setup. The constant torque above  $H_{C2}$  is due to the compensation of the decreasing angle  $\theta_M$  and the increasing magnetization amplitude (Fig. 6.5b). Due to the good agreement of calculation and experiment in Fig. 6.5 and 6.6, we can conclude that the the magnetic properties are well described by this simple microscopic model, which is further developed by THz absorption spectroscopy. The measurements of the spin-wave frequencies enables the extraction of the magnetic exchange and  $g$ -factor parameters, as presented in [99].

## 6.3 Summary

We were able to reveal the magnetic phase transitions of two systems by torque magnetometry. The conventional measurement technique to determine the transition fields is by magnetization curves. The emergence of sharp features in the magnetic torque proved to be an excellent complimentary experimental approach to accurately obtain these transition fields. This is especially true for the cycloidal-skyrmion phase transition in  $\text{GaV}_4\text{S}_8$ . In  $\text{Mn}_2\text{Mo}_3\text{O}_8$  the canting of the magnetic moments could be resolved by combining magnetization curves with measurements of the magnetic torque as well.

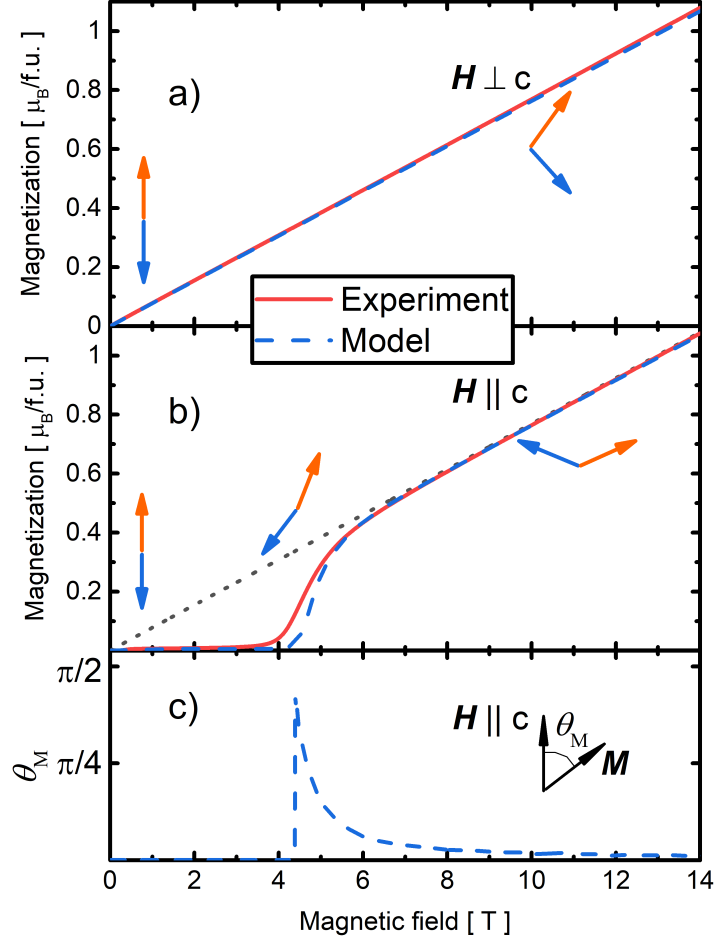


Figure 6.5: Magnetic field dependence of the magnetization of  $\text{Mn}_2\text{Mo}_3\text{O}_8$  at  $T = 2$  K. Magnetic field is perpendicular (a) and parallel (b,c) to the  $c$  axis. The red solid line corresponds to the experiment, while the blue dashed line corresponds to the model calculation. The orange and blue arrows illustrate the magnetic moments of the two sublattices in different magnetic fields pointing horizontally/vertically for (a) and (b), respectively. The experimental curve of the  $\mathbf{H} \perp c$  case is repeated in (b) as black dotted line for comparison. Panel (c) shows the calculated angle  $\theta_M$  enclosed by the magnetization and the magnetic field. The presented measurements (a,b) were performed by Anton Jesche at the Center for Electronic Correlations and Magnetism of the University of Augsburg and the model was calculated by David Szaller [99].

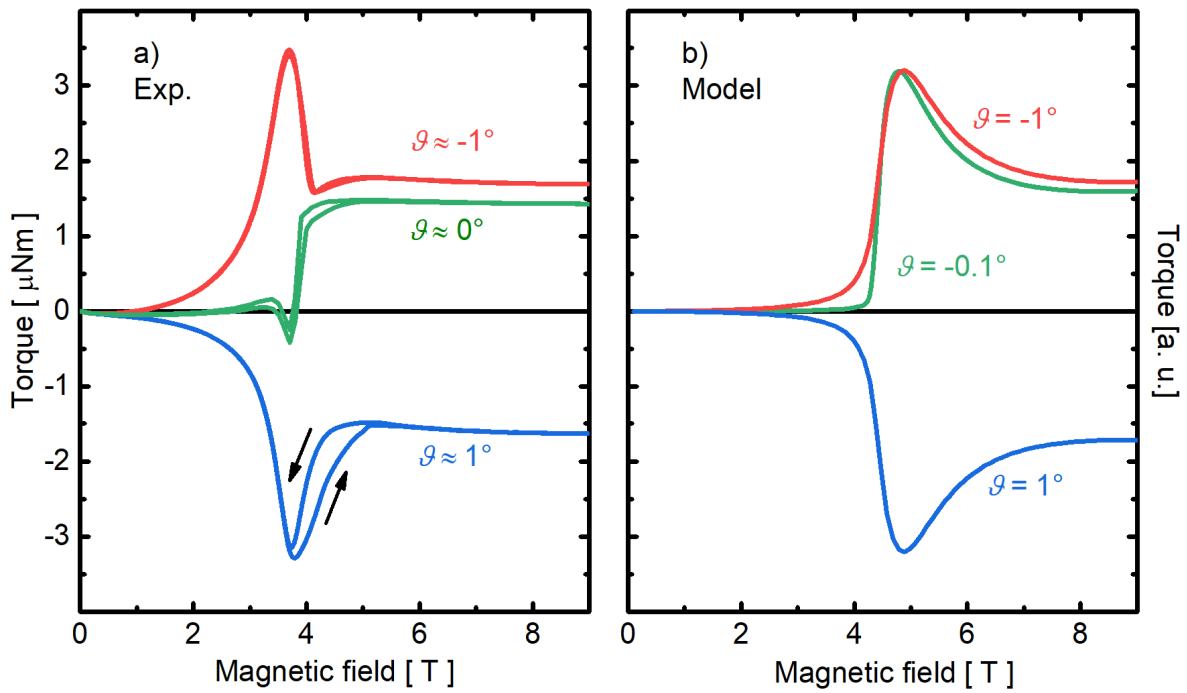


Figure 6.6: Magnetic field dependence of the magnetic torque in  $\text{Mn}_2\text{Mo}_3\text{O}_8$  at  $T = 2$  K. (a) experiment and (b) model calculation. The angle included between the  $c$  axis and the magnetic field is denoted by  $\vartheta$ , where the  $\pm$  signs represent the directions towards the  $\pm a$ -axes.



# 7 Radiative Damping in Yttrium-Iron-Garnet Films

In this chapter<sup>1</sup> we present the investigation of the magnetic equivalent of electric super-radiance in yttrium iron garnet (YIG) thin films. The ferrimagnetic resonance is analyzed for two samples of different thicknesses in a quasi-optical sub-THz transmission spectroscopy with an applied magnetic field in two different geometries (Chapter 2.3). The magnetic superradiance can be easily separated from the intrinsic damping, both of them leading to a broadening of the resonance signal, by a straightforward analysis, based on Maxwell's equations.

## 7.1 Introduction

Since the current CMOS-based electronics is soon to reach its limitations [102], the design of fundamentally new ways to forward, process, and store information is of vital importance. One possible direction is offered by magnonics, where information is manifested in the magnetic state of matter and forwarded as an oscillating magnetic wave (magnon) [103]. The lifetime of such an excited state, usually in the microwave frequency range, is a crucial factor when designing potential applications. Besides their use in information technology, the research of magnonic systems with long-lifetime excitations is also motivated by their role as model systems of fundamental physical effects, such as Bose-Einstein condensation and other macroscopic quantum transport phenomena [104; 105].

Lifetime measurement of various excited states is an essential tool for analyzing physical, chemical, and biological processes and making spectroscopic state assignments [106]. The most direct way is to observe the transient optical signal following the excitation pulse, typically in luminescence, and by fitting the exponential decay, the lifetime of the corresponding excited state can be determined [107]. Another approach involves the phase shift of the response as compared to the modulated excitation signal [108].

The third method utilizes Heisenberg's uncertainty principle, which connects the lifetime of a state to the uncertainty of its energy [109], resulting in the natural line broadening of the spectroscopic absorption or emission signal. However, starting from the earliest spectroscopic experiments, the intrinsic natural broadening is dominated by other phenomena, such as the collision between particles and the Doppler-effect due to thermal motion in the atomic spectral lines of gases [110]. In case of microwave magnetic resonance

---

<sup>1</sup>This chapter is based on a paper that is about to be published [101].

measurements, where the magnetic sample is coupled to the GHz-radiation typically by a coplanar waveguide, the two main contributions to the non-intrinsic linewidth result from eddy currents induced either in the conducting sample [111] or in the waveguide [112], which effects are termed eddy-current- and radiative damping, respectively [113].

In several cases when intrinsic damping is low and the density of oscillators is high, the damping due to coherent radiation starts to dominate, the effect known as superradiance [114]. Superradiance denotes coherent emission of uncoupled emitters when interacting with the same mode of electromagnetic wave, predicted in the Dicke-modell [115] and observed both in gases inside of an optical cavity [116; 117; 118], in metamaterials [119; 120], and in two-dimensional electron gases [121; 122; 123; 124].

The concept of superradiance was first discussed by Dicke for two-level molecules in a gas [115]. More general, superradiance is now considered as the coherent radiative emission by a system of uncoupled oscillators, which are connected only by their interaction with the same mode of an electromagnetic wave. In recent years new interest arose (e.g. [114]) from the investigation of superradiance at the cyclotron resonance, which couples to the electric field of the light, in two-dimensional electron gases [121]. In this case the superradiance can dominate the intrinsic damping, when an applied gate voltage leads to a high density of oscillators. However, to achieve the dominance of superradiance in magnetic oscillators is not as simple, since the material parameters limit the oscillator density and the magnetic coupling to the light wave is rather small. Therefore an approach of separating the intrinsic and radiative contributions to the linewidth of the resonance signal is developed and applied to a wide range of measurements, which is obtained by the variation of resonance frequency, experimental geometry (Faraday/Voigt) and sample thickness.

## 7.2 Experimental Method

For this investigation two thin films of  $\text{Y}_3\text{Fe}_5\text{O}_{12}$  (YIG) grown by liquid epitaxy on a paramagnetic  $\text{Gd}_3\text{Ga}_5\text{O}_{12}$  (GGG) substrate were chosen due to the strong and sharp ferrimagnetic resonance of YIG and the well known properties of both compounds. The first sample is a  $3\ \mu\text{m}$  thick YIG film on a  $537\ \mu\text{m}$  GGG, while the second sample consists of two  $6.1\ \mu\text{m}$  YIG-films on both sides of a  $471\ \mu\text{m}$  thick GGG substrate. Since the thickness of the thin films is crucial for the interpretation of the optical experiments, for quality control, static magnetization measurements were performed in a vibrating sample magnetometer (Chapter 2.2) and in the temperature range of 5-300 K, as shown in Fig. 7.1. The thickness of the YIG layer in the sample was accurately determined from the magnitude of the observed magnetization step at a small magnetic field, corresponding to the switching of the ferrimagnetic magnetization of the YIG film (Fig. 7.1).

The measurements were performed in Voigt geometry with a linearly polarized beam in the phase-sensitive Mach-Zehnder setup and in Faraday geometry at the exact same frequencies with a circularly polarized beam in the transmission-only mode (see Chap-

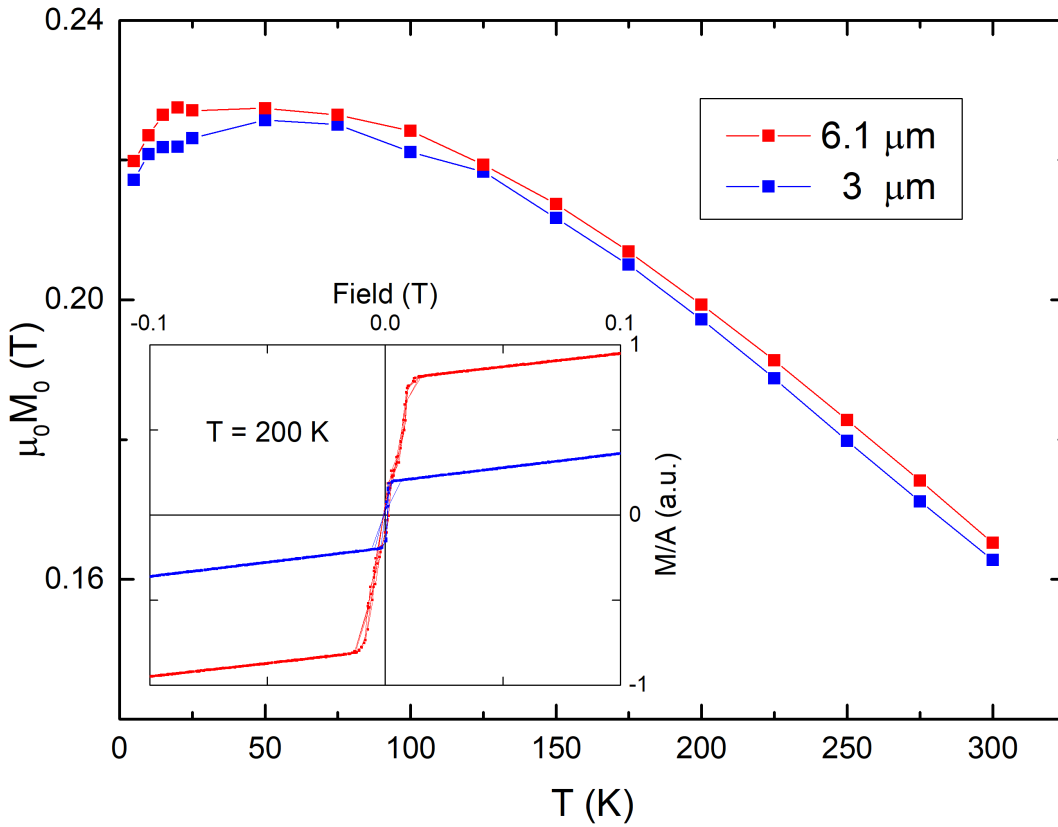


Figure 7.1: The temperature dependent ferrimagnetic magnetization of the YIG film is shown for the sample consisting of one 3  $\mu\text{m}$  thick YIG layer and the sample consisting of two 6.1  $\mu\text{m}$  thick YIG layers on top of the GGG substrate. In the inset the magnetization as a function of magnetic field is shown for both samples, normalized with the area of the thin film. Therefore the magnitude of the step in magnetization corresponds directly to the thickness of the films.

ter 2.3). During the measurements, the sample temperature was kept at 200 K.

### 7.3 Analyzing the Transmission Spectra and Separating Intrinsic and Radiative Damping

The transmission spectra have been analyzed using the Fresnel optical equations for a multilayer system [125], assuming a Lorentzian line-shape for the ferri/paramagnetic resonance in the magnetic permeability of the YIG film and the GGG substrate, respectively. As discussed below, to visualize the effects of magnetic superradiance, simplified expressions for the transmission coefficient are more appropriate. This procedure allows a direct estimate of the relevant material parameters from the spectra. The magnetic resonances of the system are shown in Fig. 7.2.

In the following we present the basic steps of the thin film approximation, which are necessary to analyze the magnetic radiative damping. Similarly to the case of cyclotron superradiance in semiconducting films [114; 126], the effect can only be observed in samples which are thin compared to the radiation wavelength. In the opposite case of the thick sample, the "superradiated" wave is re-absorbed, thus forming the propagation wave within the material.

The response of the magnetic moment  $\mathbf{M}$  of YIG to an external magnetic field  $\mathbf{H}$  is given by the Landau-Lifshitz-Gilbert equation of motion [127]

$$\frac{d\mathbf{M}}{dt} = -\gamma\mu_0 (\mathbf{M} \times \mathbf{H}) + \frac{\alpha}{M_0} \left( \mathbf{M} \times \frac{d\mathbf{M}}{dt} \right), \quad (7.1)$$

where  $\gamma$  denotes the gyromagnetic ratio,  $M_0$  the saturation magnetization,  $\alpha$  the dimensionless Gilbert damping parameter, and  $\mu_0$  the vacuum permeability. Here we assumed that the oscillation is coherent in the sample, due to the monochromatic incoming light of the same phase and the small thickness of the films.

In case of an incoming THz beam with frequency  $\omega$  and within Faraday geometry the magnetic field in the film is given by  $\mathbf{H} = (h_x e^{i\omega t}, h_y e^{i\omega t}, H_0^F)$ . Here  $h_{x,y} e^{i\omega t}$  is the oscillating (AC) field in the sample plane,  $H_0^F$  is the strength of the static (DC) magnetic field in the material given by  $H_0^F = |H_0 - M_0|$ , with the applied external field  $H_0$ . Linearizing Eq. (7.1), we finally get the standard result for the magnetic susceptibility for the circularly polarized light in the Faraday geometry:

$$\chi_{\pm}^F = \frac{m_{\pm}}{h_{\pm}} = \frac{\gamma M_0}{\omega_0^F \mp \omega + i\alpha\omega}, \quad (7.2)$$

where  $m_{\pm}, h_{\pm}$  are the circular AC magnetization and field, respectively, and  $\omega_0^F = \gamma|H_0 - M_0|$  is the ferromagnetic resonance frequency.

Similarly, in the Voigt geometry with linearly polarized light  $\mathbf{H} = (H_0, h_y e^{i\omega t}, 0)$  the

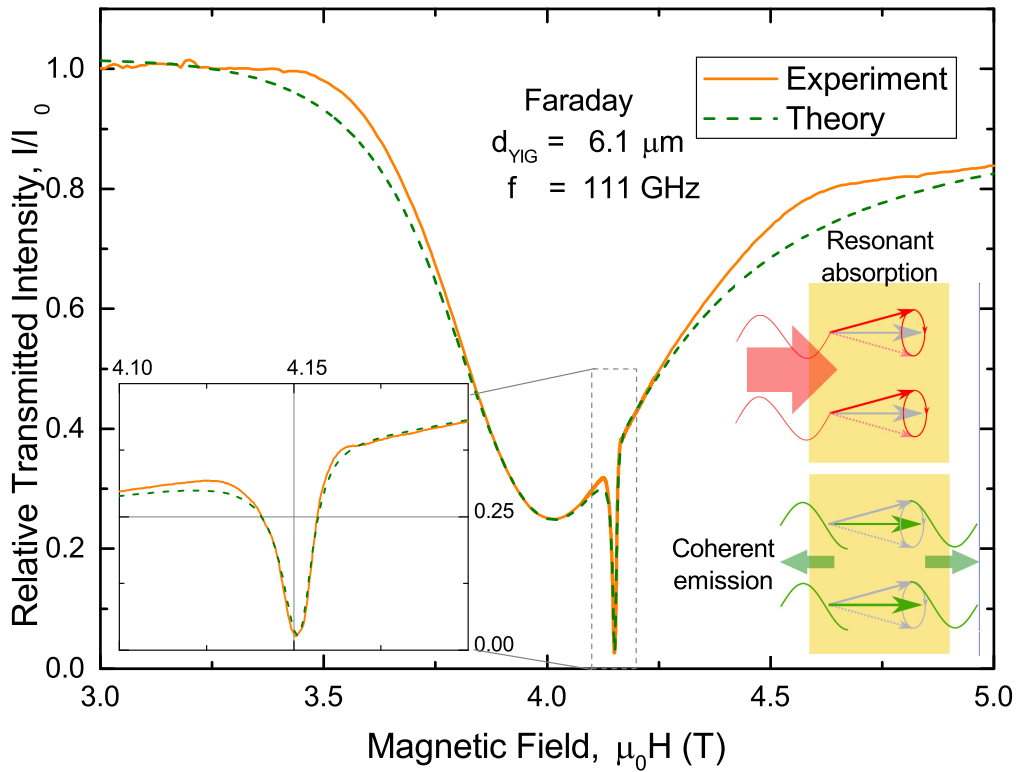


Figure 7.2: Magnetic field dependence of the transmission of a YIG/GGG system at  $\omega = 111 \text{ GHz}$ . The solid orange curve shows the experiment and the dashed green line the fit using the Fresnel equations [125]. The broad minimum around a magnetic field of 4.0 T corresponds to the paramagnetic resonance in GGG, while the sharp minimum at 4.15 T is due to the ferrimagnetic resonance in YIG. The inset shows the expanded view of this resonance in YIG. The underlying physical processes, namely magnetic absorption and coherent emission, are depicted in the schematic cartoons.

susceptibility is obtained as

$$\chi_y^V = \frac{(\omega_0^V)^2 M_0 / H_0}{(\omega_0^V)^2 + (\alpha - i)^2 \omega^2}, \quad (7.3)$$

with  $\omega_0^V = \gamma \sqrt{H_0(H_0 + M_0)}$  resonance frequency.

To obtain the radiative contribution to the damping, we consider the transmission through a magnetic sample in the thin film approximation [128; 129]. In this approximation, the boundary conditions are rewritten, taking the thin film as a part of the boundary. For the Faraday geometry with circularly polarized light, we use the Maxwell equations

$$\begin{aligned} \oint_{\partial A} \mathbf{E} \cdot d\mathbf{l} &= - \iint_A \frac{\partial \mathbf{B}}{\partial t} \cdot d\mathbf{A} \\ \oint_{\partial A} \mathbf{H} \cdot d\mathbf{l} &= \iint_A \frac{\partial \mathbf{D}}{\partial t} \cdot d\mathbf{A} \end{aligned} \quad (7.4)$$

to obtain the fields on both sides of the film:

$$\begin{aligned} e_{\pm}^0 - e_{\pm}^r - e_{\pm}^t &= -i\omega d\mu_0 (h_{\pm} + m_{\pm}) \\ h_{\pm}^0 + h_{\pm}^r - h_{\pm}^t &= i\omega d e_{\pm} \varepsilon \varepsilon_0. \end{aligned} \quad (7.5)$$

On the left-hand side of Eq. (7.5), ( $e$ ) and ( $h$ ) are the AC electric and magnetic fields of the incident (0), reflected (r) and transmitted (t) wave. On the right-hand side, within the thin-sample approximation, the linear dependence of the AC electric and magnetic fields along the surface normal of the sample is assumed. Thus,  $e_{\pm}$ ,  $h_{\pm}$  and  $m_{\pm}$  are the mean values of the corresponding fields and of the magnetization inside the film. Here  $d$  denotes the sample thickness, and  $\varepsilon$ ,  $\varepsilon_0$  stand for the electric permittivity of YIG and vacuum, respectively. To obtain Eq. (7.5), the integration path in the Maxwell equations must be taken across both sides of the sample.

The AC electric and magnetic fields are connected via  $\mathbf{e} = Z_0 \mathbf{h} / n_{1,2}$ , where  $Z_0 = \sqrt{\mu_0 / \varepsilon_0}$  is the impedance of free space, and  $n_{1,2}$  is the refractive index of the dielectric media on both sides of the film. To further simplify the final expressions, for frequencies close to the ferromagnetic resonance, we assume  $\chi_{\pm}^F \gg 1$  and neglect all smaller terms. After some simple algebra, the transmission coefficient is obtained as:

$$t_{\pm}^F = \frac{h_{\pm}^t}{h_{\pm}^0} = \left( \frac{1}{2} + \frac{1}{2n} + \frac{i\omega d\mu_0 \chi_{\pm}^F}{2Z_0} \right)^{-1}, \quad (7.6)$$

where  $n$  stands for the refractive index of the substrate (GGG in our case).

In order to obtain relative transmission due to the magnetic resonance in YIG, Eq. (7.6)

### 7.3 Analyzing the Transmission Spectra and Separating Intrinsic and Radiative Damping

should be normalized by the transmission<sup>2</sup> through the pure substrate,  $t|_{d=0}$ :

$$\frac{t_{\pm}^{\text{F}}}{t_{\pm}^{\text{F}}|_{d=0}} = 1 - \frac{i\Gamma_{\text{rad}}^{\text{F}}}{\omega_0 - \omega + i\alpha\omega + i\Gamma_{\text{rad}}^{\text{F}}}, \quad (7.7)$$

where we introduce the radiative damping parameter as

$$\Gamma_{\text{rad}}^{\text{F}} = \frac{n}{Z_0(n+1)}\omega d\mu_0\gamma M_0 = 2\pi\frac{n}{n+1}\frac{d}{\lambda}\gamma M_0. \quad (7.8)$$

Here  $\lambda$  is the radiation wavelength.

In the case of Voigt geometry, the normalized transmission for a linearly polarized wave with  $h_y$  results in the same expression as in Eq. (7.7), where the superradiant damping parameter is replaced by

$$\Gamma_{\text{rad}}^{\text{V}} = \frac{\Gamma_{\text{rad}}^{\text{F}}}{2}. \quad (7.9)$$

In the case of electric superradiance in thin films the corresponding equation reads [126]

$$\Gamma_{\text{rad}} = n_{2\text{D}}e^2Z_0/2m. \quad (7.10)$$

Here  $n_{2\text{D}}$  is the density,  $e$  the charge, and  $m$  the effective mass of two-dimensional electrons. In the electric case, to control the ratio between intrinsic and radiation damping, the electron density can be easily changed by variation of the gate voltage [126]. In the magnetic case the parameter responsible for the radiance intensity is the static magnetization  $M_0$  that can be modified by tuning the temperature. An alternative way to control the superradiance is by changing the sample thickness  $d$ , as seen in Eq. (7.8).

Eq. (7.7) provides an expression for a resonant minimum in transmission with an effective width given by the sum of intrinsic ( $\alpha$ ) and radiative ( $\Gamma_{\text{rad}}^{\text{F}}$ ) parts. Since both the amplitude and the linewidth of the peak in Eq. (7.7) contains  $\Gamma_{\text{rad}}^{\text{F}}$ , the power of the secondary re-emitted wave grows with the square of the number of magnetic moments due to  $\Gamma_{\text{rad}}^{\text{F}} \sim M_0d$ . This scaling is characteristic for coherent radiation, such as superradiance.

According to Eq. (7.7), compared to an intrinsic damping  $\Gamma_{\text{int}} = \alpha\omega$ , the resonance is additionally broadened by the radiative damping  $\Gamma_{\text{rad}}$ . As illustrated in Fig. 7.3, the analysis of the linewidth and amplitude of the resonance according to Eq. (7.7) provides a way to directly obtain both damping parameters independently.

Fig. 7.2 shows the typical magnetic field dependent transmission of YIG films on GGG substrate. The sharp minimum at 4.14 T that corresponds to the ferrimagnetic resonance of YIG is observed on top of the broad paramagnetic resonance of the GGG

<sup>2</sup>In case of two films on both sides of the substrate the transmission in the same approximation is given by  $t(2d) = |t(d)|^2$ .

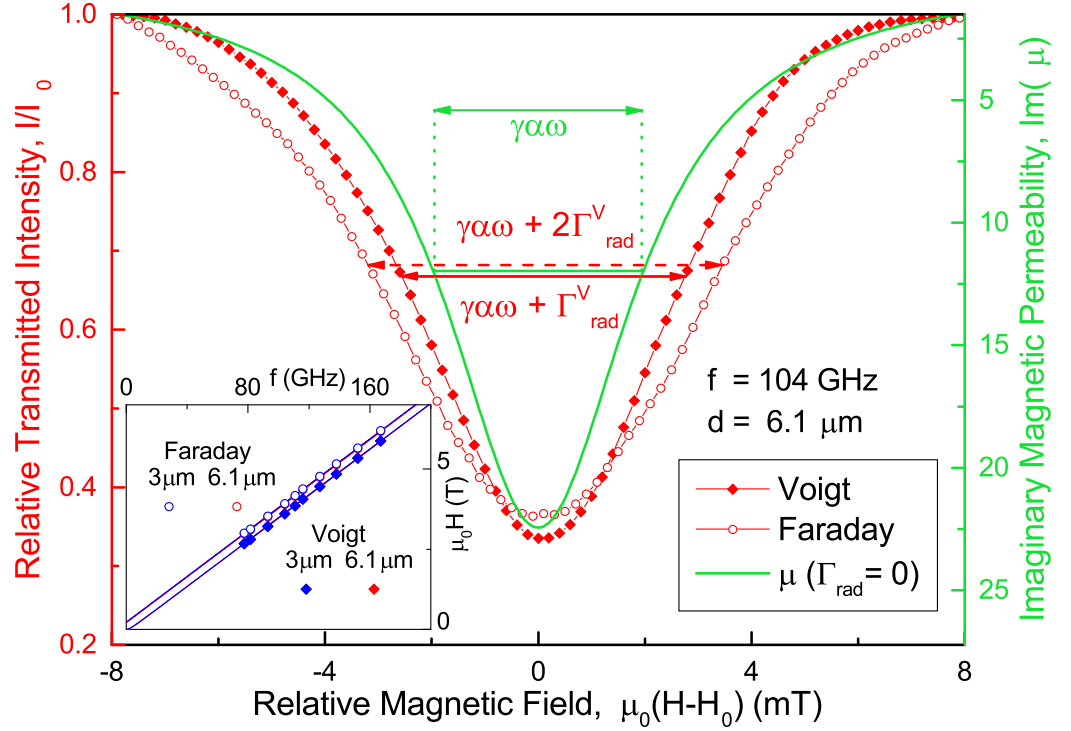


Figure 7.3: Ferrimagnetic resonance linewidth in YIG at  $f = 104$  GHz frequency. Resonance curves correspond to the intrinsic damping ( $\text{Im}(\mu)$ , green) and observed superradiance effects in the Faraday (red open circles) and Voigt (red filled diamonds) geometries. The horizontal axis shows the magnetic field  $H$  relative to the corresponding resonance field  $H_0$ . Red labels on the left vertical axis belong to the experimental curves and indicate the transmitted light intensity relative to the substrate's transmission baseline. The inverse scale on the green right axis corresponds to the imaginary part of the magnetic permeability. The frequency dependence of the ferrimagnetic resonance fields (open/filled symbols for Faraday/Voigt geometry experiments) in two YIG films of different thicknesses ( $d = 3 \mu\text{m}$  in blue and  $d = 6.1 \mu\text{m}$  in red) is presented in the inset, where lines show theoretical expectations of the resonance frequencies. The experimental points for both samples lie nearly exactly on top of each other.

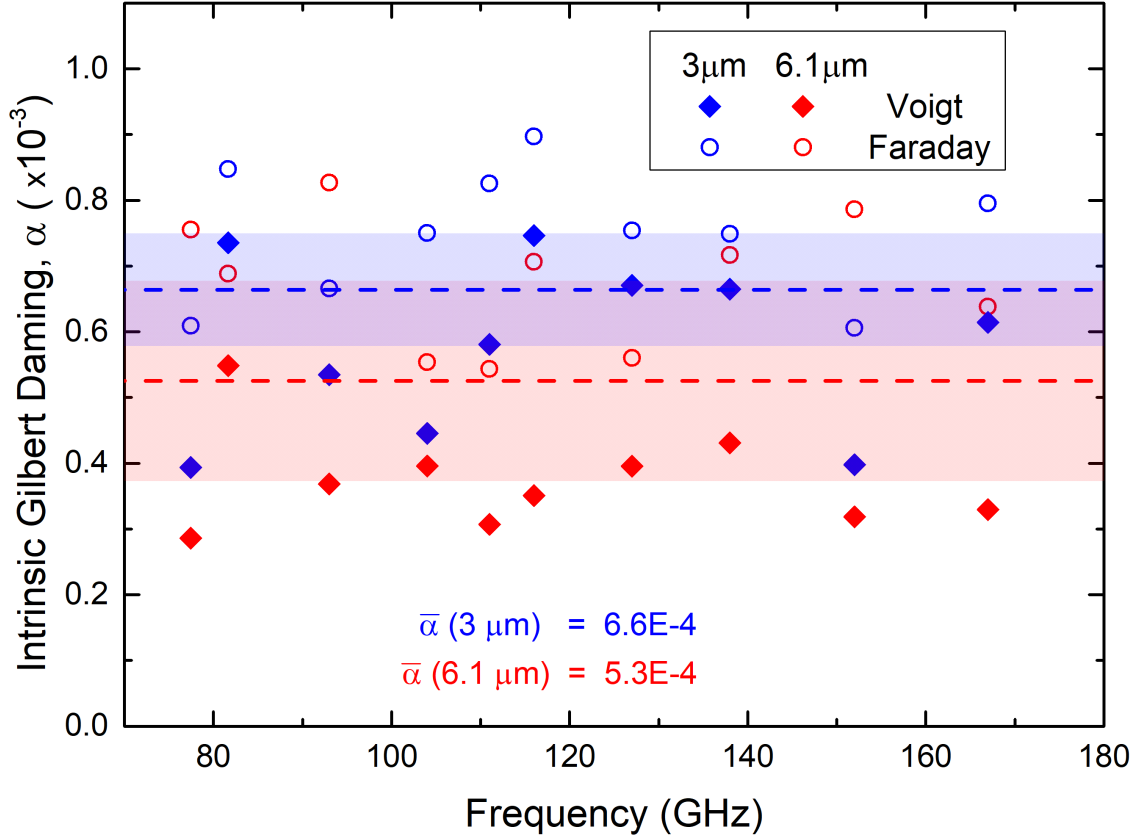


Figure 7.4: Frequency dependence of the intrinsic damping parameter,  $\alpha$ , which is extracted from fits of the resonance in transmission for samples with different thicknesses (6.1  $\mu\text{m}$  - red, 3  $\mu\text{m}$  - blue). The measurement error is indicated by bands of the corresponding colors.

substrate. The two resonances were fitted simultaneously using Fresnel equations for the transmission of the layered system. The free parameters in such a fit are the saturation magnetization of the YIG film  $M_0$ , intrinsic damping  $\alpha$ , and the resonance field  $H_{\text{res}}$ . The refractive index of the GGG substrate,  $n = 3.43$ , was obtained in a separate experiment [130]. The magnetic field dependence of the paramagnetic resonance frequency in GGG corresponds to a  $g$ -factor of  $g_{\text{GGG}} = 2.26$ .

The ferrimagnetic resonance field  $H_{\text{res}}$  of YIG shows an approximately linear dependence on the frequency  $f$  (see inset in Fig. 7.3), which is expected in high magnetic fields  $H_0 \gg M_0$ . From the fits to these data we estimate the values for the saturation magnetization  $\mu_0 M_0(T = 200\text{K}) = 0.22 \pm 0.05 \text{ T}$ , in reasonable agreement with the literature values [131] and with the static data,  $\mu_0 M_0^{\text{VSM}} = 0.198 \text{ T}$ , measured on the same sample using vibrating sample magnetometry (Fig. 7.1).

Fig. 7.3 demonstrates that the ferrimagnetic resonance linewidth of YIG in the transmission is indeed substantially higher than the actual resonance linewidth in the mag-

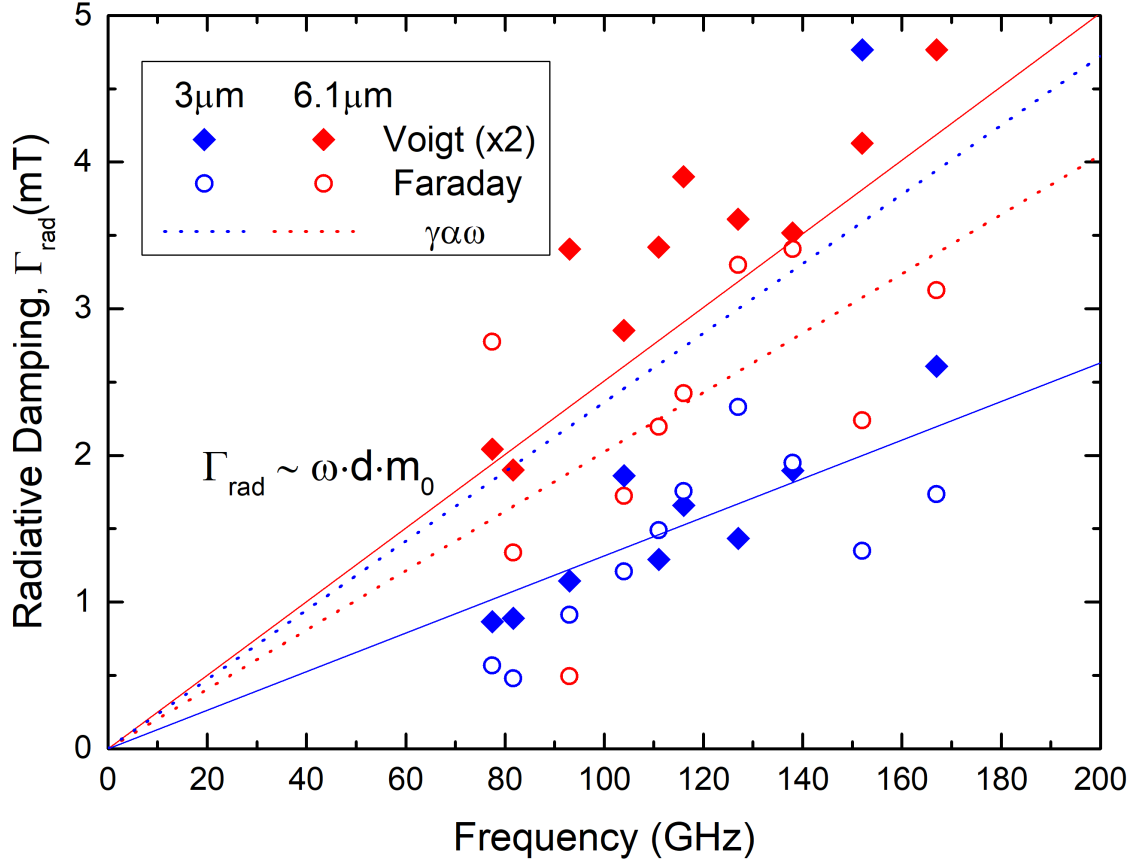


Figure 7.5: Frequency dependence of the radiative damping. Points correspond to experiments on the ferrimagnetic resonance in thin films, solid lines show calculations according to Eqs. (7.8) and (7.9), while dotted lines give the value of the intrinsic damping,  $\alpha\omega$ , for comparison. Radiative damping from the Voigt experiments is scaled by a factor of 2, according to Eq. (7.9).

netic permeability,  $\mu(H)$ . Moreover, the radiative correction in Faraday geometry is twice as large as in Voigt configuration, in agreement with Eq. (7.9). The transmission spectra allow us to extract the relevant electrodynamic parameters using different approaches. In a first approach it can be done using the *exact* Fresnel expressions [125] including the magnetic permeability given by Eqs. (7.2,7.3). Here the radiative damping is not a free parameter [126] but is obtained via Eq. (7.8). The second way to compare intrinsic and radiative damping is to use the simplified Eq. (7.7). In this case, the width of the resonance curve directly gives the total damping parameter  $\Gamma_{\text{int}} + \Gamma_{\text{rad}}$ , and the radiative damping is extracted from the amplitude of the resonance curves.

The values of intrinsic damping obtained from the present experiments are shown in Fig. 7.4. As expected, the Gilbert damping parameter  $\alpha$  in our samples is approximately frequency-independent and agrees reasonably well with other reports (e.g. [132; 133; 134]).

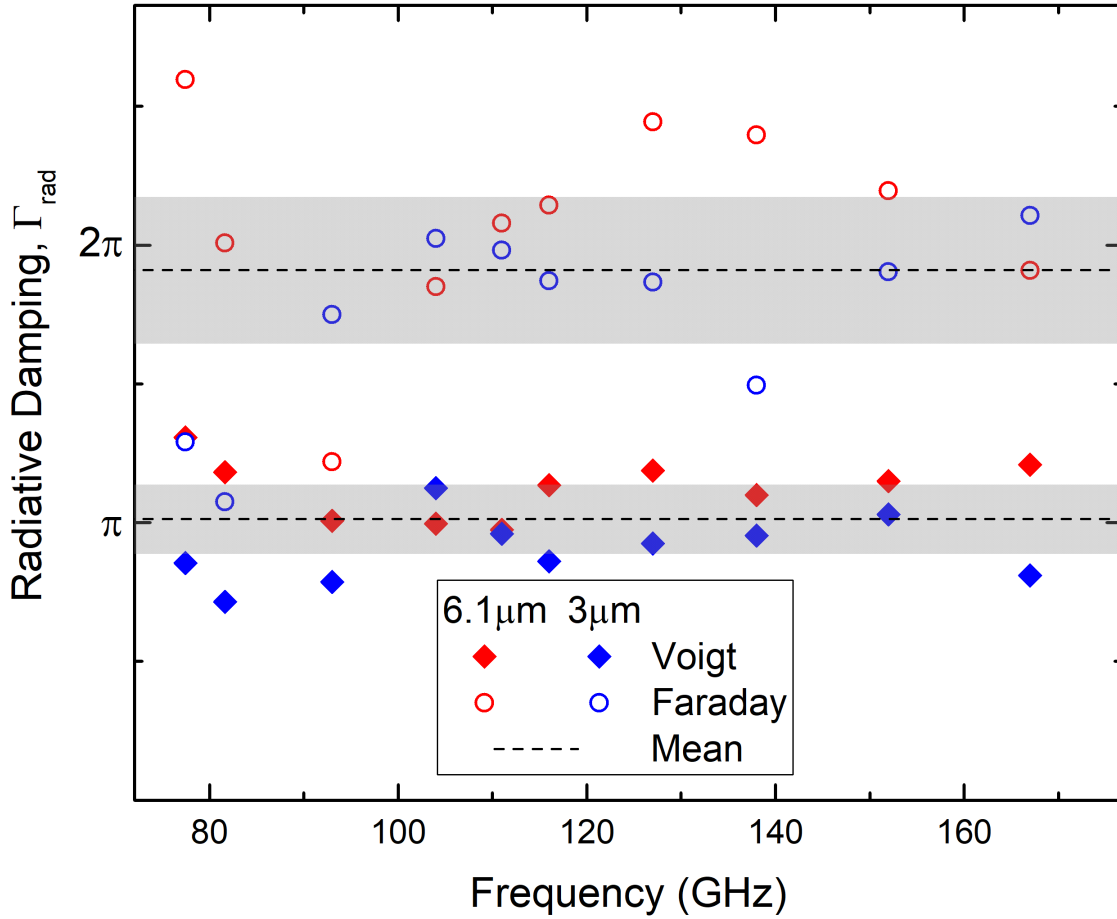


Figure 7.6: Experimental confirmation of Eq. (7.8): The radiative damping  $\Gamma_{\text{rad}}$  is shown in the units of  $\frac{n}{n+1} \frac{d}{\lambda} \gamma M_0$ , which should lead to a value of  $2\pi$  for Faraday geometry (empty symbols) and of  $\pi$  for Voigt geometry (full symbols). The mean of the  $6.1 \mu\text{m}$  (red) and  $3 \mu\text{m}$  (blue) samples of both geometries is indicated by the dashed lines and the corresponding error given by the gray area.

Fig. 7.5 shows the frequency dependence of the radiative damping at the magnetic resonance.  $\Gamma_{\text{rad}}$  is proportional to the frequency and to the sample thickness as expected from Eq. (7.8). Comparing the values of the intrinsic (dotted lines) and radiative damping, we see that in the thin film with  $d = 3 \mu\text{m}$ , the intrinsic damping dominates. On the contrary in the thicker film both contributions are of comparable values:  $\omega\alpha \sim \Gamma_{\text{rad}}(6.1 \mu\text{m})$ .

Finally, by plotting the radiative damping in the units of  $\frac{n}{n+1} \frac{d}{\lambda} \gamma M_0$  the Eq. (7.8) could be confirmed, since the remainder gives  $\pi$  and  $2\pi$  for Voigt (see Eq. (7.9)) and Faraday geometry, respectively, which can be well reproduced, as demonstrated in Fig. 7.6. An oscillation around those values is especially visible for the Faraday measurements, which can be traced back to Fabry-Pérot interferences in the substrate.

## 7.4 Summary

We have presented a method to separate the intrinsic and radiative contributions to magnetic thin films' resonance linewidth in optical absorption experiments, including an accurate determination of the intrinsic Gilbert damping parameter  $\alpha$ . The coherent nature of the radiative line broadening mechanism allows its identification as the magnetic equivalent of superradiance, opening a fundamentally new way to study this collective phenomenon in the dynamics of magnetic systems.

## 8 Conclusions

In this work a diverse set of phenomena in magnetoelectric materials, obtained by a wide range of experimental techniques, was presented and discussed. The selection of static and dynamic setups enabled us for not only detecting the magnetoelectric effect directly by measuring the magnetically induced electric polarization, but also to investigate further effects, like quantum phase transitions, an electron-phonon coupling and the magnetic equivalence of superradiance.

For two rare-earth magnetoelectrics the effect was measured and modelled. In samarium ferroborate we applied an already developed model to the high-field effect, which allowed for correcting the Sm-Fe molecular field and, by complementing already published measurements, to determine the  $g$ -factor of the samarium ions in this system. Moreover, we reported the discovery of a small magnetoelectric effect of the sixth order, which was not observed up to now.

In  $\text{Ho}_x\text{La}_{3-x}\text{Ga}_5\text{SiO}_{14}$  a profound study was conducted, revealing a puzzling magnetoelectric effect, which cannot be classified in the classic categories of linear versus higher-order effects. The sixfold oscillation of the magnetically induced polarization, when the magnetic field is swept around the threefold symmetry axis, indicates a magnetoelectric effect of the sixth order, similar to samarium ferroborate. However, the electric polarization becomes linearly dependent on the magnetic field strengths above a low field threshold. In two steps we presented a simple phenomenological model, first solely based on one easy axis for each of the three Ho-sites, which was then extended to also fit the experimentally obtained magnetic anisotropy, by a two-easy axes approach. Both models give a reasonable agreement of the magnetoelectric effect, whilst only the second model gives a sufficient explanation of the magnetic torque and the angular dependent magnetization. Nevertheless, we formulated some open questions, which have to be answered for a complete understanding of the magnetic and magnetoelectric properties of the system. The lowest lying crystal field level was obtained by measurements of the paramagnetic resonance and the electric polarization induced by strong magnetic fields. Even though it could indicate the energies of higher crystal field levels, a complete investigation of the exact energies would be desired. Furthermore a strong magnetic field dependent low-frequency excitation was discovered, which we identified as a phonon that seems to be coupled to the crystal field levels of the holmiums  $4f$ -electrons and, therefore, narrows in magnetic fields along the threefold symmetry axis.

The torque magnetometry was further used to identify transitions between different spin configurations in transition metal multiferroics.  $\text{GaV}_4\text{S}_8$  was reported to have a rather fine magnetic phase diagram at low temperatures and small fields. We were able

to show that measurements of the magnetic torque provide an excellent experimental confirmation of the proposed phase transitions between cycloidal spin structures and Néel-skyrmions. Moreover, torque magnetometry was used to complement the magnetization curves of  $\text{Mn}_2\text{Mo}_3\text{O}_8$  to reveal the uneven canting of the magnetic moments on two different sublattices. These studies prove the value of the experimental setup to identify quantum phase transitions.

For the well known yttrium-iron-garnet thin films, the ferrimagnetic resonance at different frequencies was thoroughly investigated. The exceptional resolution of the backward wave oscillators provided the opportunity to obtain small changes in the linewidth of the sharp absorption lines. The high frequency of this optical approach provided a precise way to determine the intrinsic Gilbert damping parameter. Based on the Maxwell equations and the boundary conditions, we were able to derive that besides the internal damping, a radiative damping term shortens the lifetime of the excitation, which could be verified by the experiments with different configurations of sample thickness and magnetic field direction.

This work demonstrates that magnetoelectric materials provide an intriguing research topic, even apart from the linear magnetoelectric effect, which the research is often focused on. Not only higher-order effects in highly symmetric paramagnetic compounds, but also dynamic phenomena, like magnetic superradiance or electron-phonon coupling are calling for further research.

# Acknowledgments

In the past years I got much support from many people without whom I could never have completed this work. First, I want to thank the following people for making my PhD possible:

- Andrei Pimenov for the supervision of this work and my measurements in the past years. Andrei and Anna Pimenov for the coordination of our group.
- André Vogel for coordinating the Solids4Fun program. More importantly, thank you for helping with the whole organization around my PhD, from filling out travel requests to getting all the credit points I needed. I always knew that I could come to your office and you would fix each and every problem I had.
- Our friendly secretaries for the administrative work.

I want to thank the following people for their scientific input:

- Andrei Pimenov for the guidance throughout my PhD. Thank you for always having an open door for me. I am very glad that I had the opportunity to explore many different experimental setups and materials.
- Alexey Shuvaev for guiding me through the various challenges that came up in the experimental work. When I had problems during the data analysis, you helped me just enough, so that I could find the solutions by myself. Thank you for your patience, you are a perfect teacher. Thank you for proofreading the thesis.
- David Szaller for the supervision of many of the herein described experiments. I am especially glad for the numerous ideas you had for new measurements. Thank you for helping me understand the different theoretical concepts in long discussions. You encouraged me to ask the simplest questions by pretending that you could still learn something from it. Thank you for proofreading the thesis.
- Evan Constable for the supervision of measurements, which unfortunately did not make it into this thesis. I learned a lot from our discussions, which we preferred to have during lunch time or certain long evenings. Thank you for proofreading the thesis.
- Thomas Kain for introducing me to the PPMS and helping me especially in my first year of the PhD with many different experimental issues.

## *Acknowledgments*

---

- Artem Kuzmenko for introducing me to the sub-THz setup, the langasites and the ferroborates. Thank you for helping me regularly by answering many questions via e-mail.
- Uladzislau Dziom for helping me to tame the U4 setup and for the discussions about science, while you filled the office with music.
- Alexander Mukhin for patiently discussing various experiments with me and explaining the theoretical concepts behind it. Thank you especially for encouraging me to share my thoughts on the measurements. Even during my first months of the PhD you took my suggestions seriously and discussed the ideas with me.
- Anna Pimenov for coordinating the group and the feedback on my contributions in the group discussions. Thank you for showing me what happens when science meets art.
- Jan Gospodarič, Lorenz Bergen and Janek Wettstein, my fellow PhD students, for the discussions in our office and in the group meetings. Thank you, Jan, for sharing your experience with the sub-THz setup and giving feedback on my presentation skills. Thank you, Lorenz, for the discussions about our shared passion, the langasites, for explaining how the TU works and for accompanying me to the measurements in Grenoble. Thank you, Janek, for the discussions about samarium ferroborate.
- Ernst Bauer for teaching me how to measure with the pressure cell and the positive and encouraging atmosphere in the lab.
- Milan Orlita and Jan Wyzula at the LNCMI in Grenoble for the collaboration and for being wonderful hosts.
- Sumanta Chattopadhyay at the High Field Lab of the Helmholtz Zentrum Dresden-Rossendorf for measuring the magnetoelectric effect in pulsed fields with me.
- Michaela Kramer for helping me with the fitting of the YIG data.

Finally, I have to thank all my friends and family for the constant support. Especially, I want to mention the following people:

- All the new friends that I made in Vienna for being the main reason that the past years are among the best of my life.
- I am so grateful that my colleagues turned quickly into good friends. Thanks to you, my time in the office was characterized by a positive working atmosphere. I will never forget the countless great evenings in Vienna and on the various conferences.

- 
- The Akademische Bläserphilharmonie Wien, for giving me and my tuba a new musical home. It was a gift to find so many good friends in this orchestra. In this short time, I made countless unforgettable experiences. From beautiful concerts and intensive rehearsals to hiking trips and memorable wine tastings. I will always remember the long nights with even longer discussions about music, science and life. Not only the work in the 'Weingarten', but also the 'Gemüsegarten' kept me sane during the past months. Special thanks to Berni Neustifter for supporting me even through the lockdown with his infamous 'Neustifter-Selection'.
  - My colleagues and friends from 5mcc, for inviting me into this awesome science communication project. I love to think ABAP with you!
  - My companions from HDL for the good time in and around the Superstore.
  - The Kramers for giving me a second home in Austria.
  - My dear friends in Germany with whom I managed to stay in close contact. Thank you for visiting me and for the open doors and beers, when I visited home.
  - My parents for the love and support. My brothers for the fact that besides all the quarrel and fun I can always rely on you.
  - Klara. For everything. I love you.



# Bibliography

- [1] J. C. Maxwell. *VIII. A dynamical theory of the electromagnetic field*. Philosophical transactions of the Royal Society of London , 155, pp. 459–512 (1865)
- [2] W. C. Röntgen. *Ueber die durch Bewegung eines im homogenen elektrischen Felde befindlichen Dielectricums hervorgerufene electrodynamische Kraft*. Annalen der Physik und Chemie **271**, 10, pp. 264–270 (1888)
- [3] P. Curie. *Sur la symétrie dans les phénomènes physiques, symétrie d'un champ électrique et d'un champ magnétique*. Journal de Physique Théorique et Appliquée **3**, 1, pp. 393–415 (1894)
- [4] L. D. Landau, E. M. Lifshitz. *Electrodynamics of continuous media*. Course of theoretical physics, Pergamon, Oxford. Trans. from the Russian (1960)
- [5] D. Astrov. *The magnetoelectric effect in antiferromagnetics*. Sov. Phys. JETP **11**, 3, pp. 708–709 (1960)
- [6] A. I. Popov, D. I. Plokhov, A. K. Zvezdin. *Quantum theory of magnetoelectricity in rare-earth multiferroics: Nd, Sm, and Eu ferrobates*. Physical Review B **87**, 2 (2013)
- [7] A. M. Kadomtseva, Y. F. Popov, S. S. Krotov, G. P. Vorob'ev, E. A. Popova, A. K. Zvezdin, L. N. Bezmaternykh. *Investigation of the anomalies of the magnetoelectric and magnetoelastic properties of single crystals of the ferrobate  $GdFe_3(BO_3)_4$  at phase transitions*. Low Temperature Physics **31**, 8, pp. 807–813 (2005)
- [8] G. Kozlov, A. Volkov. *Coherent source submillimeter wave spectroscopy*. In *Topics in Applied Physics*, pp. 51–109. Springer Berlin Heidelberg (1998)
- [9] M. Fiebig. *Revival of the magnetoelectric effect*. Journal of Physics D: Applied Physics **38**, 8, pp. R123–R152 (2005)
- [10] J.-P. Rivera. *A short review of the magnetoelectric effect and related experimental techniques on single phase (multi-) ferroics*. The European Physical Journal B **71**, 3, pp. 299–313 (2009)
- [11] M. Fiebig, T. Lottermoser, D. Meier, M. Trassin. *The evolution of multiferroics*. Nature Reviews Materials **1**, 8, p. 16046 (2016)

## BIBLIOGRAPHY

---

- [12] N. A. Spaldin, R. Ramesh. *Advances in magnetoelectric multiferroics*. Nature materials **18**, 3, p. 203 (2019)
- [13] G. T. Rado, V. J. Folen. *Observation of the Magnetically Induced Magnetoelectric Effect and Evidence for Antiferromagnetic Domains*. Physical Review Letters **7**, 8, pp. 310–311 (1961)
- [14] T. H. O’Dell. *An induced magneto-electric effect in yttrium iron garnet*. Philosophical Magazine **16**, 141, pp. 487–494 (1967)
- [15] B. Krichevstov, V. Pavlov, R. Pisarev. *Giant linear magnetoelectric effect in garnet ferrite films*. Jetp Lett **49**, 8, p. 535 (1989)
- [16] E. Ascher. *Higher-order magneto-electric effects*. The Philosophical Magazine: A Journal of Theoretical Experimental and Applied Physics **17**, 145, pp. 149–157 (1968)
- [17] T. Kurumaji, S. Ishiwata, Y. Tokura. *Doping-Tunable Ferrimagnetic Phase with Large Linear Magnetoelectric Effect in a Polar Magnet  $Fe_2Mo_3O_8$* . Physical Review X **5**, 3 (2015)
- [18] A. Shuvaev, V. Dziom, A. Pimenov, M. Schiebl, A. A. Mukhin, A. C. Komarek, T. Finger, M. Braden, A. Pimenov. *Electric Field Control of Terahertz Polarization in a Multiferroic Manganite with Electromagnons*. Physical Review Letters **111**, 22 (2013)
- [19] S. Bluck, H. G. Kahle. *Measurement and interpretation of the magneto-electric effect in  $TbPO_4$* . Journal of Physics C: Solid State Physics **21**, 29, pp. 5193–5208 (1988)
- [20] T. H. O’Dell. *The field invariants in a magneto-electric medium*. Philosophical Magazine **8**, 87, pp. 411–418 (1963)
- [21] W. F. Brown, R. M. Hornreich, S. Shtrikman. *Upper Bound on the Magnetoelectric Susceptibility*. Physical Review **168**, 2, pp. 574–577 (1968)
- [22] H. Schmid. *Magnetoelectric effects in insulating magnetic materials*. In A. Lakhtakia, W. S. Weiglhofer, R. F. Messier (Editors), *Complex Mediums*. SPIE (2000)
- [23] S. L. Hou, N. Bloembergen. *Paramagnetoelectric Effects in  $NiSO_4 \cdot 6H_2O$* . Physical Review **138**, 4A, pp. A1218–A1226 (1965)
- [24] C. Tabares-Munoz, J. P. Rivera, A. Bezings, A. Monnier, H. Schmid. *Measurement of the Quadratic Magnetoelectric Effect on Single Crystalline  $BiFeO_3$* . Japanese Journal of Applied Physics **24**, S2, p. 1051 (1985)

- 
- [25] B. Howes, M. Pelizzone, P. Fischer, C. Tabares-munoz, J. pierre Rivera, H. Schmid. *Characterisation of some magnetic and magnetoelectric properties of ferroelectric  $Pb(Fe_{1/2}Nb_{1/2})O_3$* . *Ferroelectrics* **54**, 1, pp. 317–320 (1984)
- [26] H. Schmid. *On a magnetoelectric classification of materials*. *International Journal of Magnetism* **4**, 4, pp. 337–361 (1973)
- [27] M. J. Cardwell. *Measurements of the magnetic field dependent electric susceptibility of yttrium iron garnet*. *Philosophical Magazine* **20**, 167, pp. 1087–1089 (1969)
- [28] A. Shubnikov. *Symmetry and Antisymmetry of Finite Figures*. (1951)
- [29] J. Curie, P. Curie. *Piezoelectric and allied phenomena in Rochelle salt*. *Comptes rendus de l'Académie des sciences* **91**, pp. 294–297 (1880)
- [30] W. Voigt, et al. *Lehrbuch der Kristallphysik*, volume 962. Teubner Leipzig (1928)
- [31] G. T. Rado. *Statistical Theory of Magnetoelectric Effects in Antiferromagnetics*. *Physical Review* **128**, 6, pp. 2546–2556 (1962)
- [32] H. Grimmer. *The piezomagnetolectric effect*. *Acta Crystallographica Section A Foundations of Crystallography* **48**, 3, pp. 266–271 (1992)
- [33] V. V. Shvartsman, S. Bedanta, P. Borisov, W. Kleemann, A. Tkach, P. M. Vilarinho. *(Sr,Mn)TiO<sub>3</sub>: A Magnetoelectric Multiglass*. *Physical Review Letters* **101**, 16 (2008)
- [34] K.-C. Liang, R. P. Chaudhury, B. Lorenz, Y. Y. Sun, L. N. Bezmaternykh, V. L. Temerov, C. W. Chu. *Giant magnetoelectric effect in  $HoAl_3(BO_3)_4$* . *Physical Review B* **83**, 18 (2011)
- [35] G. A. Gehring. *On the microscopic theory of the magnetoelectric effect*. *Ferroelectrics* **161**, 1, pp. 275–285 (1994)
- [36] I. Dzyaloshinsky. *A thermodynamic theory of “weak” ferromagnetism of antiferromagnetics*. *Journal of Physics and Chemistry of Solids* **4**, 4, pp. 241–255 (1958)
- [37] T. Moriya. *New Mechanism of Anisotropic Superexchange Interaction*. *Physical Review Letters* **4**, 5, pp. 228–230 (1960)
- [38] H. Schmid. *Multi-ferroic magnetoelectrics*. *Ferroelectrics* **162**, 1, pp. 317–338 (1994)
- [39] J. F. Scott. *Applications of magnetoelectrics*. *Journal of Materials Chemistry* **22**, 11, p. 4567 (2012)

- [40] M. Bibes, A. Barthélémy. *Towards a magnetoelectric memory*. Nature Materials **7**, 6, pp. 425–426 (2008)
- [41] A. Pimenov, A. A. Mukhin, V. Y. Ivanov, V. D. Travkin, A. M. Balbashov, A. Loidl. *Possible evidence for electromagnons in multiferroic manganites*. Nature Physics **2**, 2, pp. 97–100 (2006)
- [42] J. Seidel, L. W. Martin, Q. He, Q. Zhan, Y.-H. Chu, A. Rother, M. E. Hawkrigde, P. Maksymovych, P. Yu, M. Gajek, N. Balke, S. V. Kalinin, S. Gemming, F. Wang, G. Catalan, J. F. Scott, N. A. Spaldin, J. Orenstein, R. Ramesh. *Conduction at domain walls in oxide multiferroics*. Nature Materials **8**, 3, pp. 229–234 (2009)
- [43] J. H. Jung, M. Matsubara, T. Arima, J. P. He, Y. Kaneko, Y. Tokura. *Optical Magnetoelectric Effect in the Polar  $GaFeO_3$  Ferrimagnet*. Physical Review Letters **93**, 3 (2004)
- [44] J. Wang. *Epitaxial  $BiFeO_3$  Multiferroic Thin Film Heterostructures*. Science **299**, 5613, pp. 1719–1722 (2003)
- [45] K. Z. Rushchanskii, S. Kamba, V. Goian, P. Vaněk, M. Savinov, J. Prokleška, D. Nuzhnyy, K. Knížek, F. Laufek, S. Eckel, S. K. Lamoreaux, A. O. Sushkov, M. Ležaić, N. A. Spaldin. *A multiferroic material to search for the permanent electric dipole moment of the electron*. Nature Materials **9**, 8, pp. 649–654 (2010)
- [46] H. Zheng. *Multiferroic  $BaTiO_3$ - $CoFe_2O_4$  Nanostructures*. Science **303**, 5658, pp. 661–663 (2004)
- [47] J. A. Mundy, C. M. Brooks, M. E. Holtz, J. A. Moyer, H. Das, A. F. Rébola, J. T. Heron, J. D. Clarkson, S. M. Disseler, Z. Liu, A. Farhan, R. Held, R. Hovden, E. Padgett, Q. Mao, H. Paik, R. Misra, L. F. Kourkoutis, E. Arenholz, A. Scholl, J. A. Borchers, W. D. Ratcliff, R. Ramesh, C. J. Fennie, P. Schiffer, D. A. Muller, D. G. Schlom. *Atomically engineered ferroic layers yield a room-temperature magnetoelectric multiferroic*. Nature **537**, 7621, pp. 523–527 (2016)
- [48] J. Ma, J. Hu, Z. Li, C.-W. Nan. *Recent Progress in Multiferroic Magnetoelectric Composites: from Bulk to Thin Films*. Advanced Materials **23**, 9, pp. 1062–1087 (2011)
- [49] P. K. Amiri, J. G. Alzate, X. Q. Cai, F. Ebrahimi, Q. Hu, K. Wong, C. Grezes, H. Lee, G. Yu, X. Li, M. Akyol, Q. Shao, J. A. Katine, J. Langer, B. Ocker, K. L. Wang. *Electric-Field-Controlled Magnetoelectric RAM: Progress, Challenges, and Scaling*. IEEE Transactions on Magnetics **51**, 11, pp. 1–7 (2015)

- [50] Y. Wang, D. Gray, J. Gao, D. Berry, M. Li, J. Li, D. Viehland, H. Luo. *Improvement of magnetoelectric properties in Metglas/Pb(Mg<sub>1/3</sub>Nb<sub>2/3</sub>)O<sub>3</sub>-PbTiO<sub>3</sub> laminates by poling optimization*. Journal of Alloys and Compounds **519**, pp. 1–3 (2012)
- [51] A. A. Bush, K. E. Kamentsev, V. F. Meshcheryakov, Y. K. Fetisov, D. V. Chashin, L. Y. Fetisov. *Low-frequency magnetoelectric effect in a Galfenol-PZT planar composite structure*. Technical Physics **54**, 9, pp. 1314–1320 (2009)
- [52] D. A. Keszler. *Borates for optical frequency conversion*. Current Opinion in Solid State and Materials Science **1**, 2, pp. 204–211 (1996)
- [53] J. A. Campá, C. Cascales, E. Gutiérrez-Puebla, M. A. Monge, I. Rasines, C. Ruíz-Valero. *Crystal Structure, Magnetic Order, and Vibrational Behavior in Iron Rare-Earth Borates*. Chemistry of Materials **9**, 1, pp. 237–240 (1997)
- [54] A. M. Kadomtseva, Y. F. Popov, G. P. Vorob'ev, A. P. Pyatakov, S. S. Krotov, K. I. Kamilov, V. Y. Ivanov, A. A. Mukhin, A. K. Zvezdin, A. M. Kuz'menko, L. N. Bezmaternykh, I. A. Gudim, V. L. Temerov. *Magnetoelectric and magnetoelastic properties of rare-earth ferrobates*. Low Temperature Physics **36**, 6, pp. 511–521 (2010)
- [55] A. K. Zvezdin, G. P. Vorob'ev, A. M. Kadomtseva, Y. F. Popov, A. P. Pyatakov, L. N. Bezmaternykh, A. V. Kuvardin, E. A. Popova. *Magnetoelectric and magnetoelastic interactions in NdFe<sub>3</sub>(BO<sub>3</sub>)<sub>4</sub> multiferroics*. JETP Letters **83**, 11, pp. 509–514 (2006)
- [56] M. N. Popova, E. P. Chukalina, B. Z. Malkin, D. A. Erofeev, L. N. Bezmaternykh, I. A. Gudim. *Crystal field and exchange interactions in the SmFe<sub>3</sub>(BO<sub>3</sub>)<sub>4</sub> multiferroic*. Journal of Experimental and Theoretical Physics **118**, 1, pp. 111–123 (2014)
- [57] E. Chukalina, M. Popova, L. Bezmaternykh, I. Gudim. *Spectroscopic study of the magnetic ordering in SmFe<sub>3</sub>(BO<sub>3</sub>)<sub>4</sub>*. Physics Letters A **374**, 15-16, pp. 1790–1792 (2010)
- [58] A. I. Pankrats, G. A. Petrakovskii, L. N. Bezmaternykh, O. A. Bayukov. *Antiferromagnetic resonance and phase diagrams of gadolinium ferrobate GdFe<sub>3</sub>(BO<sub>3</sub>)<sub>4</sub>*. Journal of Experimental and Theoretical Physics **99**, 4, pp. 766–775 (2004)
- [59] E. Eremin, N. Volkov, V. Temerov, I. Gudim, A. Bovina. *Specific features of magnetic properties of rare-earth ferrobates Sm<sub>1-x</sub>La<sub>x</sub>Fe<sub>3</sub>(BO<sub>3</sub>)<sub>4</sub>*. Physics of the Solid State **57**, 3, pp. 569–575 (2015)

- [60] Z. Frait. *The g-factor in pure polycrystalline iron*. Czechoslovak Journal of Physics **27**, 2, pp. 185–189 (1977)
- [61] L. Weymann, L. Bergen, T. Kain, A. Pimenov, A. Shuvaev, E. Constable, D. Szaller, B. V. Mill, A. M. Kuzmenko, V. Y. Ivanov, N. V. Kostyuchenko, A. I. Popov, A. K. Zvezdin, A. Pimenov, A. A. Mukhin, M. Mostovoy. *Unusual magnetoelectric effect in paramagnetic rare-earth langasite*. npj Quantum Materials **5**, 1 (2020)
- [62] A. Kaminskii, B. Mill, I. Silvestrova, G. Khodzhabagian. *The nonlinearly active material  $(La_{1-x}Nd_x)_3Ga_5SiO_{14}$* . IzSSR **47**, pp. 1903–1909 (1983)
- [63] I. Andreev, M. Dubovik. *New piezoelectric langasite  $La_3Ga_5SiO_{14}$ -material with zero temperature-coefficient of elastic oscillation particles*. Pisma V Zhurnal Tekhnicheskoi Fiziki **10**, 8, pp. 487–491 (1984)
- [64] B. Mill, Y. Pisarevsky. *Langasite-type materials: from discovery to present state*. In *Proceedings of the 2000 IEEE/EIA International Frequency Control Symposium and Exhibition (Cat. No.00CH37052)*. IEEE (2000)
- [65] H. Fritze, H. L. Tuller. *Langasite for high-temperature bulk acoustic wave applications*. Applied Physics Letters **78**, 7, pp. 976–977 (2001)
- [66] M. Hamidon, V. Skarda, N. White, F. Krispel, P. Krempf, M. Binhack, W. Buff. *Fabrication of high temperature surface acoustic wave devices for sensor applications*. Sensors and Actuators A: Physical **123-124**, pp. 403–407 (2005)
- [67] J. Stade, L. Bohatý, M. Hengst, R. Heimann. *Electro-optic, Piezoelectric and Dielectric Properties of Langasite  $(La_3Ga_5SiO_{14})$ , Langanite  $(La_3Ga_{5.5}Nb_{0.5}O_{14})$  and Langataite  $(La_3Ga_{5.5}Ta_{0.5}O_{14})$* . Crystal Research and Technology: Journal of Experimental and Industrial Crystallography **37**, 10, pp. 1113–1120 (2002)
- [68] H. Kong, J. Wang, H. Zhang, X. Yin, S. Zhang, Y. Liu, X. Cheng, L. Gao, X. Hu, M. Jiang. *Growth, properties and application as an electrooptic Q-switch of langasite crystal*. Journal of Crystal Growth **254**, 3-4, pp. 360–367 (2003)
- [69] B. A. Maksimov, V. N. Molchanov, B. V. Mill, E. L. Belokoneva, M. K. Rabadanov, A. A. Pugacheva, Y. V. Pisarevskii, V. I. Simonov. *Absolute structure of  $La_3Ga_5SiO_{14}$  langasite crystals*. Crystallography Reports **50**, 5, pp. 751–758 (2005)
- [70] P. Bordet, I. Gelard, K. Marty, A. Ibanez, J. Robert, V. Simonet, B. Canals, R. Ballou, P. Lejay. *Magnetic frustration on a Kagomé lattice in  $R_3Ga_5SiO_{14}$  langasites with  $R = Nd, Pr$* . Journal of Physics: Condensed Matter **18**, 22, pp. 5147–5153 (2006)

- [71] K. Marty, P. Bordet, V. Simonet, M. Loire, R. Ballou, C. Darie, J. Kljun, P. Bonville, O. Isnard, P. Lejay, B. Zawilski, C. Simon. *Magnetic and dielectric properties in the langasite-type compounds:  $A_3BFe_3D_2O_{14}$  ( $A=Ba, Sr, Ca$ ;  $B=Ta, Nb, Sb$ ;  $D=Ge, Si$ )*. Physical Review B **81**, 5 (2010)
- [72] M. Loire, V. Simonet, S. Petit, K. Marty, P. Bordet, P. Lejay, J. Ollivier, M. Enderle, P. Steffens, E. Ressouche, A. Zorko, R. Ballou. *Parity-Broken Chiral Spin Dynamics in  $Ba_3NbFe_3Si_2O_{14}$* . Physical Review Letters **106**, 20 (2011)
- [73] M. Ramakrishnan, E. Constable, A. Cano, M. Mostovoy, J. S. White, N. Gurung, E. Schierle, S. de Brion, C. V. Colin, F. Gay, P. Lejay, E. Ressouche, E. Weschke, V. Scagnoli, R. Ballou, V. Simonet, U. Staub. *Field-induced double spin spiral in a frustrated chiral magnet*. npj Quantum Materials **4**, 1 (2019)
- [74] J. Robert, V. Simonet, B. Canals, R. Ballou, P. Bordet, P. Lejay, A. Stunault. *Spin-Liquid Correlations in the Nd-Langasite Anisotropic Kagomé Antiferromagnet*. Physical Review Letters **96**, 19 (2006)
- [75] J. Robert, V. Simonet, B. Canals, R. Ballou, P. Bordet, P. Lejay, A. Stunault. *Erratum: Spin-Liquid Correlations in the Nd-Langasite Anisotropic Kagomé Antiferromagnet*. Physical Review Letters **97**, 25 (2006)
- [76] A. Konstantinova, T. Golovina, A. Dudka. *Anisotropy of Optical Activity in Langasite Family Crystals*. Crystallography Reports **63**, 2, pp. 200–206 (2018)
- [77] A. K. Zvezdin, S. S. Krotov, A. M. Kadomtseva, G. P. Vorob'ev, Y. F. Popov, A. P. Pyatakov, L. N. Bezmaternykh, E. Popova. *Magnetoelectric effects in gadolinium iron borate  $GdFe_3(BO_3)_4$* . Journal of Experimental and Theoretical Physics Letters **81**, 6, pp. 272–276 (2005)
- [78] V. Y. Ivanov, A. Kuzmenko, A. A. Mukhin. *Magnetoelectric effect in ytterbium aluminum borate  $YbAl_3(BO_3)_4$* . JETP Letters **105**, 7, pp. 435–441 (2017)
- [79] A. Zvezdin, R. Levitin, A. Popov, V. Silant'ev. *Magnetic field strength dependence of the magnetostriction of rare-earth iron garnets*. Zhurnal Eksperimental'noj i Teoreticheskoy Fiziki **80**, 4, pp. 1504–1513 (1981)
- [80] G. Babushkin, A. Zvezdin, R. Levitin, V. Orlov, A. Popov. *Theoretical and experimental investigations of the magnetostriction of paramagnetic rare-earth garnets  $Tb_3Ga_5O_{12}$  and  $Dy_3Al_5O_{12}$* . Zhurnal Eksperimental'noi i Teoreticheskoi Fiziki **85**, 4, pp. 1366–1376 (1983)
- [81] N. Vedernikov, A. Zvezdin, R. Levitin, A. Popov. *Magnetic linear birefringence in rare earth garnets*. Zhurnal Eksperimental'noj i Teoreticheskoy Fiziki **93**, 12, pp. 2161–2178 (1987)

- [82] N. Vedernikov, A. Zvezdin, R. Levitin, A. Popov. *Magnetostriction of paramagnetic rare-earth garnets*. Zh. Eksp. Teor. Fiz **94**, p. 370 (1988)
- [83] J. H. Van Vleck. *The theory of electric and magnetic susceptibilities*. Clarendon Press (1932)
- [84] C. Kittel. *Einführung in die Festkörperphysik, 15. Aufl* (2013)
- [85] L. Bergen, L. Weymann, A. Kuzmenko, A. A. Mukhin, E. Constable, A. Pimenov. *Low Frequency Phonons in Langasites*. to be published (2020)
- [86] R. Pocha, D. Johrendt, R. Pöttgen. *Electronic and structural instabilities in  $GaV_4S_8$  and  $GaMo_4S_8$* . Chemistry of materials **12**, 10, pp. 2882–2887 (2000)
- [87] E. Ruff, S. Widmann, P. Lunkenheimer, V. Tsurkan, S. Bordács, I. Kézsmárki, A. Loidl. *Multiferroicity and skyrmions carrying electric polarization in  $GaV_4S_8$* . Science Advances **1**, 10, p. e1500916 (2015)
- [88] S. McAlister, P. Strobel. *Magnetic order in  $M_2Mo_3O_8$  single crystals ( $M = Mn, Fe, Co, Ni$ )*. Journal of Magnetism and Magnetic Materials **30**, 3, pp. 340–348 (1983)
- [89] T. Kurumaji, S. Ishiwata, Y. Tokura. *Diagonal magnetoelectric susceptibility and effect of Fe doping in the polar ferrimagnet  $Mn_2Mo_3O_8$* . Physical Review B **95**, 4 (2017)
- [90] I. Kézsmárki, S. Bordács, P. Milde, E. Neuber, L. M. Eng, J. S. White, H. M. Rønnow, C. D. Dewhurst, M. Mochizuki, K. Yanai, H. Nakamura, D. Ehlers, V. Tsurkan, A. Loidl. *Néel-type skyrmion lattice with confined orientation in the polar magnetic semiconductor  $GaV_4S_8$* . Nature Materials **14**, 11, pp. 1116–1122 (2015)
- [91] S. Mühlbauer, B. Binz, F. Jonietz, C. Pfleiderer, A. Rosch, A. Neubauer, R. Georgii, P. Boni. *Skyrmion Lattice in a Chiral Magnet*. Science **323**, 5916, pp. 915–919 (2009)
- [92] A. N. Bogdanov, D. Yablonskii. *Thermodynamically stable “vortices” in magnetically ordered crystals. The mixed state of magnets*. Zh. Eksp. Teor. Fiz **95**, 1, p. 178 (1989)
- [93] W. Kang, Y. Huang, X. Zhang, Y. Zhou, W. Zhao. *Skyrmion-Electronics: An Overview and Outlook*. Proceedings of the IEEE **104**, 10, pp. 2040–2061 (2016)
- [94] A. K. Nayak, V. Kumar, T. Ma, P. Werner, E. Pippel, R. Sahoo, F. Damay, U. K. Röfler, C. Felser, S. S. P. Parkin. *Magnetic antiskyrmions above room temperature in tetragonal Heusler materials*. Nature **548**, 7669, pp. 561–566 (2017)

- [95] M. M. Abd-Elmeguid, B. Ni, D. I. Khomskii, R. Pocha, D. Johrendt, X. Wang, K. Syassen. *Transition from Mott Insulator to Superconductor in  $\text{GaNb}_4\text{Se}_8$  and  $\text{GaTa}_4\text{Se}_8$  under High Pressure*. Physical Review Letters **93**, 12 (2004)
- [96] E. Dorolti, L. Cario, B. Corraze, E. Janod, C. Vaju, H.-J. Koo, E. Kan, M.-H. Whangbo. *Half-Metallic Ferromagnetism and Large Negative Magnetoresistance in the New Lacunar Spinel  $\text{GaTi}_3\text{VS}_8$* . Journal of the American Chemical Society **132**, 16, pp. 5704–5710 (2010)
- [97] K. Singh, C. Simon, E. Cannuccia, M.-B. Lepetit, B. Corraze, E. Janod, L. Cario. *Orbital-Ordering-Driven Multiferroicity and Magnetoelectric Coupling in  $\text{GeV}_4\text{S}_8$* . Physical Review Letters **113**, 13 (2014)
- [98] C. Yadav, A. Nigam, A. Rastogi. *Thermodynamic properties of ferromagnetic Mott-insulator  $\text{GaV}_4\text{S}_8$* . Physica B: Condensed Matter **403**, 5-9, pp. 1474–1475 (2008)
- [99] D. Szaller, K. Szász, S. Bordács, J. Viirok, T. Rõõm, U. Nagel, A. Shuvaev, L. Weymann, A. Pimenov, A. A. Tsirlin, A. Jesche, L. Prodan, V. Tsurkan, I. Kézsmárki. *Magnetic anisotropy and exchange paths for octa- and tetrahedrally coordinated  $\text{Mn}^{2+}$  ions in the honeycomb multiferroic  $\text{Mn}_2\text{Mo}_3\text{O}_8$* . accepted for publication (2020)
- [100] Y. Wang, G. L. Pascut, B. Gao, T. A. Tyson, K. Haule, V. Kiryukhin, S.-W. Cheong. *Unveiling hidden ferrimagnetism and giant magnetoelectricity in polar magnet  $\text{Fe}_2\text{Mo}_3\text{O}_8$* . Scientific Reports **5**, 1 (2015)
- [101] L. Weymann, A. Shuvaev, A. Pimenov, A. A. Mukhin, D. Szaller. *The magnetic equivalent of electric superradiance: radiative damping in yttrium-iron-garnet films*. to be published (2020)
- [102] J. A. del Alamo. *Nanometre-scale electronics with III–V compound semiconductors*. Nature **479**, 7373, pp. 317–323 (2011)
- [103] A. V. Chumak, V. I. Vasyuchka, A. A. Serga, B. Hillebrands. *Magnon spintronics*. Nature Physics **11**, 6, pp. 453–461 (2015)
- [104] S. O. Demokritov, V. E. Demidov, O. Dzyapko, G. A. Melkov, A. A. Serga, B. Hillebrands, A. N. Slavin. *Bose–Einstein condensation of quasi-equilibrium magnons at room temperature under pumping*. Nature **443**, 7110, pp. 430–433 (2006)
- [105] D. A. Bozhko, A. A. Serga, P. Clausen, V. I. Vasyuchka, F. Heussner, G. A. Melkov, A. Pomyalov, V. S. L’vov, B. Hillebrands. *Supercurrent in a room-temperature Bose–Einstein magnon condensate*. Nature Physics **12**, 11, pp. 1057–1062 (2016)

## BIBLIOGRAPHY

---

- [106] J. Demas. *Excited state lifetime measurements*. Elsevier (2012)
- [107] J. Demas. *Luminescence decay times and bimolecular quenching. An ultrafast kinetics experiment*. Journal of Chemical Education **53**, 10, p. 657 (1976)
- [108] R. D. Spencer, G. Weber. *Influence of Brownian Rotations and Energy Transfer upon the Measurements of Fluorescence Lifetime*. The Journal of Chemical Physics **52**, 4, pp. 1654–1663 (1970)
- [109] E. A. Gislason, N. H. Sabelli, J. W. Wood. *New form of the time-energy uncertainty relation*. Physical Review A **31**, 4, pp. 2078–2081 (1985)
- [110] W. Voigt. *Das Gesetz der Intensitätsverteilung innerhalb der Linien eines Gasspektrums*. Verlagd. KB Akad. d. Wiss. (1912)
- [111] P. Pincus. *Excitation of Spin Waves in Ferromagnets: Eddy Current and Boundary Condition Effects*. Physical Review **118**, 3, pp. 658–664 (1960)
- [112] G. Wende. *Radiation damping in FMR measurements in a nonresonant rectangular waveguide*. Physica Status Solidi (a) **36**, 2, pp. 557–567 (1976)
- [113] M. A. W. Schoen, J. M. Shaw, H. T. Nembach, M. Weiler, T. J. Silva. *Radiative damping in waveguide-based ferromagnetic resonance measured via analysis of perpendicular standing spin waves in sputtered permalloy films*. Physical Review B **92**, 18 (2015)
- [114] K. Cong, Q. Zhang, Y. Wang, G. T. Noe, A. Belyanin, J. Kono. *Dicke superradiance in solids*. Journal of the Optical Society of America B **33**, 7, p. C80 (2016)
- [115] R. H. Dicke. *Coherence in Spontaneous Radiation Processes*. Physical Review **93**, 1, pp. 99–110 (1954)
- [116] N. Skribanowitz, I. P. Herman, J. C. MacGillivray, M. S. Feld. *Observation of Dicke Superradiance in Optically Pumped HF Gas*. Physical Review Letters **30**, 8, pp. 309–312 (1973)
- [117] M. Gross, P. Goy, C. Fabre, S. Haroche, J. M. Raimond. *Maser Oscillation and Microwave Superradiance in Small Systems of Rydberg Atoms*. Physical Review Letters **43**, 5, pp. 343–346 (1979)
- [118] Y. Kaluzny, P. Goy, M. Gross, J. M. Raimond, S. Haroche. *Observation of Self-Induced Rabi Oscillations in Two-Level Atoms Excited Inside a Resonant Cavity: The Ringing Regime of Superradiance*. Physical Review Letters **51**, 13, pp. 1175–1178 (1983)

- [119] Y. Sonnefraud, N. Verellen, H. Sobhani, G. A. Vandenbosch, V. V. Moshchalkov, P. V. Dorpe, P. Nordlander, S. A. Maier. *Experimental Realization of Subradiant, Superradiant, and Fano Resonances in Ring/Disk Plasmonic Nanocavities*. ACS Nano **4**, 3, pp. 1664–1670 (2010)
- [120] M. Wenclawiak, K. Unterrainer, J. Darmo. *Cooperative effects in an ensemble of planar meta-atoms*. Applied Physics Letters **110**, 26, p. 261101 (2017)
- [121] Q. Zhang, T. Arikawa, E. Kato, J. L. Reno, W. Pan, J. D. Watson, M. J. Manfra, M. A. Zudov, M. Tokman, M. Erukhimova, A. Belyanin, J. Kono. *Superradiant Decay of Cyclotron Resonance of Two-Dimensional Electron Gases*. Physical Review Letters **113**, 4 (2014)
- [122] T. Laurent, Y. Todorov, A. Vasanelli, A. Delteil, C. Sirtori, I. Sagnes, G. Beaudoin. *Superradiant Emission from a Collective Excitation in a Semiconductor*. Physical Review Letters **115**, 18 (2015)
- [123] Q. Zhang, M. Lou, X. Li, J. L. Reno, W. Pan, J. D. Watson, M. J. Manfra, J. Kono. *Collective non-perturbative coupling of 2D electrons with high-quality-factor terahertz cavity photons*. Nature Physics **12**, 11, pp. 1005–1011 (2016)
- [124] T. Maag, A. Bayer, S. Baiertl, M. Hohenleutner, T. Korn, C. Schüller, D. Schuh, D. Bougeard, C. Lange, R. Huber, M. Mootz, J. E. Sipe, S. W. Koch, M. Kira. *Coherent cyclotron motion beyond Kohn's theorem*. Nature Physics **12**, 2, pp. 119–123 (2015)
- [125] A. M. Shuvaev, G. V. Astakhov, C. Brüne, H. Buhmann, L. W. Molenkamp, A. Pimenov. *Terahertz magneto-optical spectroscopy in HgTe thin films*. Semiconductor Science and Technology **27**, 12, p. 124004 (2012)
- [126] J. Gospodarič, V. Dziom, A. Shuvaev, A. A. Dobretsova, N. N. Mikhailov, Z. D. Kvon, A. Pimenov. *Superradiant and transport lifetimes of the cyclotron resonance in the topological insulator HgTe*. Physical Review B **99**, 11 (2019)
- [127] A. G. Gurevich, G. A. Melkov. *Magnetization Oscillations and Waves*. Taylor & Francis Inc. ISBN 0849394600 (1996)
- [128] M. Oksanen, S. Tretyakov, I. Lindell. *Vector Circuit Theory for Isotropic and Chiral Slabs*. Journal of Electromagnetic Waves and Applications **4**, 7, pp. 613–643 (1990)
- [129] D. Szaller, A. Shuvaev, A. Mukhin, A. Kuzmenko, A. Pimenov. *Controlling of light with electromagnons*. arXiv preprint arXiv:1910.05071 (2019)

## BIBLIOGRAPHY

---

- [130] A. Schneider, A. Shuvaev, S. Engelbrecht, S. O. Demokritov, A. Pimenov. *Electrically Excited Inverse Electron Spin Resonance in a Split-Ring Metamaterial Resonator*. Physical Review Letters **103**, 10 (2009)
- [131] E. E. Anderson. *Molecular Field Model and the Magnetization of YIG*. Physical Review **134**, 6A, pp. A1581–A1585 (1964)
- [132] M. Chen, C. Patton, G. Srinivasan, Y. Zhang. *Ferromagnetic resonance foldover and spin-wave instability in single-crystal YIG films*. IEEE Transactions on Magnetics **25**, 5, pp. 3485–3487 (1989)
- [133] O. d’Allivy Kelly, A. Anane, R. Bernard, J. B. Youssef, C. Hahn, A. H. Molpeceres, C. Carrétéro, E. Jacquet, C. Deranlot, P. Bortolotti, R. Lebourgeois, J.-C. Mage, G. de Loubens, O. Klein, V. Cros, A. Fert. *Inverse spin Hall effect in nanometer-thick yttrium iron garnet/Pt system*. Applied Physics Letters **103**, 8, p. 082408 (2013)
- [134] S. Kosen, A. F. van Loo, D. A. Bozhko, L. Mihalceanu, A. D. Karenowska. *Microwave magnon damping in YIG films at millikelvin temperatures*. APL Materials **7**, 10, p. 101120 (2019)

# Lukas Weymann

## Curriculum Vitae

Kölblgasse 32/38  
1030, Vienna, Austria  
☎ (+43) 678 1252369  
✉ lukas.weymann@gmx.net



### Education

- 2016-present **Ph.D.**, *Technische Universität Wien*, Vienna, Austria.  
Solid State Spectroscopy - Institute of Solid State Physics
- 2014–2016 **Master of Science**, *Leibniz University Hannover*, Hannover, Germany.  
Physics - Albert Einstein Institute of Hannover
- 2011–2014 **Bachelor of Science**, *Leibniz University Hannover*, Hannover, Germany.  
Physics - Institute for Theoretical Physics
- 2011 **Abitur**, *Ratsgymnasium Osnabrück*, Osnabrück, Germany.

### Masters Thesis

- Title *Long-Term Gamma-Ray Timing of an Extreme Black Widow Binary Pulsar*
- Supervisors Dr. Holger Pletsch & Prof. Domenico Giulini

### Bachelors Thesis

- Title *Point Particles in a Five-Dimensional Reissner-Nordström-de-Sitter Space-time*
- Supervisor Prof. Olaf Lechtenfeld

### Communication Skills

#### Presentations within the Scientific Community

- 09/2019 Contributed Talk at "EASTMAG - 2019"
- 03/2019 Contributed Talk at "DPG Spring Meeting of the Condensed Matter Section"
- 03/2018 Contributed Talk at "DPG Spring Meeting of the Condensed Matter Section and EPS-CMD27"
- 02/2018 Contributed Talk at "33. Workshop on Novel Materials and Superconductors"

## Science Communication

- 2020–present **Producer/Host**, "5MinutenClimateChance - Der Klimapodcast", Vienna, Austria.
- 2018 **Local Co-Coordinator**, "Wissensdurst-Festival", Vienna, Austria.
- 2017 **Teammember Physics**, "Wissensdurst-Festival", Vienna, Austria.

---

## Publications

- 2020 D. Szaller et al. *Magnetic anisotropy and exchange paths for octa- and tetrahedrally coordinated  $Mn^{2+}$  ions in the honeycomb multiferroic  $Mn_2Mo_3O_8$* . accepted for publication
- 2020 L. Weymann et al. *The magnetic equivalent of electric superradiance: radiative damping in yttrium-iron-garnet films*. submitted
- 2020 L. Weymann et al. *Unusual magnetoelectric effect in paramagnetic rare-earth langasite*. npj Quantum Materials, **5**, 61 (2020)
- 2018 A. M. Kuzmenko et al. *Switching of Magnons by Electric and Magnetic Fields in Multiferroic Borates*. Phys. Rev. Lett. **120**, 027203 (2018)

---

## Languages

- German **Mothertongue**
- English **Advanced**

### Programming Languages

- Python **Experienced**
- C/Java **Basic**